Sheffield Hallam University

A Sheffield Hallam University thesis

Morphology and Structure of Syndiotactic Polystyrene

Stéphane Moyses

A thesis submitted in partial fulfilment of the requirements of
Sheffield Hallam University
for the degree of Doctor of Philosophy

November 1997
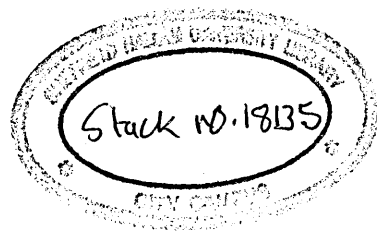
Abstract

The δ-phase of the syndiotactic polystyrene/ethylbenzene system, as formed by crystallisation from dilute solution, is shown to result in a lamellar morphology, with a monoclinic crystal lattice similar to that already reported for the complex with toluene. The temperature/concentration phase diagram for sPS/ethylbenzene gels was obtained using DSC. This shows the presence of three polymer/solvent compounds, one of which contains 0.25 solvent molecules per monomer unit. For this latter compound, the stoichiometry corresponds to that proposed by Chatani et al. for the δ-phase of sPS in toluene. Combined SAXS, FTIR, DSC and TGA measurements show that an increase in the X-ray long period between 80 and 120°C is related to solvent loss and decomplexation. There is also some temporary loss in helical order. SANS measurements on the δ-phase reveal negligible isotopic fractionation. The small increase in the in-plane radius of gyration with increasing molecular weight is interpreted as evidence of a sheetlike molecular conformation, with superfolding at higher molecular weights leading to a multiple sheet structure. On transformation to the solvent-free γ-phase, an increase in radius of gyration results from a displacement of crystal stems out of the δ-phase sheets.

Further support to these conclusions is brought by intermediate and wide angle neutron scattering. Data for δ-phase are shown to be consistent with sheetlike arrangements of crystal stems along the $\underline{a}$ direction. Adjacent stems therefore show an alternation in helicity. Simulations based on a statistical model have been used to calculate statistical parameters, such as the probability of adjacency (P_A), for which optimum agreement is found for a value of 0.8. Radii of gyration obtained from simulations are in good agreement with experimental values. The molecular weight range studied appears to cover the change from a single sheet structure to a superfolded double sheet. The same stem statistics (with $P_A = 0.8$) apply, irrespective of molecular weight. Scattering data from the γ-phase of sPS are well reproduced by a model involving some movement of stems out of the planes of sheets.

SANS measurements have been made using tilted samples in order to separate in-plane and out-of-plane radii of gyration. Comparison between the out-of-plane radius and the long spacing determined from small angle X-ray measurements shows close agreement for the lower molecular weight in both δ- and γ-phases, while R_z is a factor of 2 larger for the higher molecular weight. This indicates that each molecule occupies a single lamella at the lower molecular weight and, on average, two lamellae at the higher one, in both δ- and γ-phases. The implication is that the δ- to γ-phase transition only involves a reorganisation of chain segments within those lamellae which originally contained the molecule.

CONTENTS

length

Acknowledgements

Introduction

When a very dilute solution of polymer is left at a given temperature for a period of time ranging from a few hours to several days, a characteristic lamellar structure may appear. When a polymer melt is cooled down, other charateristic structures are encountered, notably shish kebabs and spherulites. For both of these, lamellar structures are obtained, for the former, in the form of the lamellar overgrowths, while the latter can be described as twisted lamellae going outwards from the central nucleus.

The question of the macromolecular structure involved in these lamellae, and also of the mechanisms leading to their formation, arises naturally. The first works were specifically carried out on polyethylene, from which the tools used for crystalline polymer research were elaborated and the basic models were built. Among these tools, infrared and Raman spectroscopy and neutron scattering have a particular significance. The former may allow the examination of a particular chain configuration and the latter the accurate determination of the individual chain conformation. For neutron scattering, use is made of mixtures of deuterated polymer in a protonated matrix [1]. This technique, called 'isotopic labelling', enables one to 'highlight' one molecule within its surroundings.

1

Since macromolecules crystallized from dilute solution were shown to fold within the lamellae [2], with folding occuring along one or several crystallographic planes, their conformation was compared to sheets built up from basic units called stems. Crystalline stems (the individual molecular traverses of the crystal) were used as basic components and experimental results were compared with models based on particular arrangements of stems [3]. It quickly appeared from both infrared and neutron scattering that these basic components were sufficient for the modelling of the chain conformation in solution crystallized polymers, in the form of rows of stems called sheet-like structures. By contrast, melt crystallized polymers have been shown to form a more random arrangement of stems [4]. For solution grown crystals, although calculations for sheet-like structures seemed to fit experimental results well, departures from idealized rows of adjacent stems and single sheets were necessary in order to explain the chain dimensions, and this led to the introduction of two features : dilution [5] and superfolding [6]. Dilution means that each stem of one particular molecule is not adjacent in a sheet, but that stems from one or several other molecules are also present in the region of the sheet occupied by the first molecule. Superfolding involves a complete departure of the macromolecule from a sheet, followed by incorporation in a separate adjacent sheet. Later, these features were successfully used for the determination of the molecular structure of isotactic polystyrene [7]. In this case, an additional problem was the existence of chains of different helicity in the crystalline structure. It was demonstrated, using neutron scattering, that the macromolecules change their helicity along their path [8].

For certain polymers, it is possible to form compounds involving intercalation of solvent molecules in the crystalline structure. They can be obtained for example, by swelling the amorphous material. These type of materials are called clathrates or polymer/solvent complexes. Research concerning polymer/solvent complexes has rapidly grown the past years. Syndiotactic polystyrene is a newly synthesized polymer [9] presenting some characteristics making it of interest. Rapid crystallisation to high levels of crystallinity and a high crystal melting temperature have contributed to its commercial interest, while the complex polymorphism [10] has led to extensive research. Syndiotactic polystyrene/solvent complexes can be obtained with a range of solvents [11] and involve a helical polymer structure. The solvated structure is termed the δ-phase, which transforms on heating and removal of solvent to the helical γ-phase. Further heating leads to the α- or β-forms, depending on heating conditions, with planar zigzag chains in both cases [10]. Additional possible structures include superlattices to the α- and β-forms [eg. 12], a mesomorphic form obtained, for example, by stretching amorphous samples [13] and an "emptied δ-form", where solvent has been removed [14]. This particular form has already found industrial applications [15].

In this study, ethylbenzene was chosen as solvent because of the clearly defined lamellar structure in the δ-phase (as will be shown here) and because of related earlier work [16]. Our aim was to understand the chain conformation of the δ- and the γ- phases and to clarify the mechanisms involved during the transition between these two phases. We were primarily interested in determining the chain conformation in sPS/ethylbenzene crystals and in comparing with those of well known polymers such as polyethylene and isotactic

3

polystyrene, in the absence of complex formation. How will the presence of intercalated solvent molecules affect the chain conformation in the δ-phase ? Once the macromolecular conformation of the δ-phase is understood, it is likely that the chain conformation of an annealed sample, brought into the γ-phase, will depend on the initial conformation. Thus, the conformation in the γ-phase can be seen as a possible modification of that in the δ-phase. The mechanisms involved during the transition from the δ- to the γ-phases are also interesting. Techniques used in this study were X-ray scattering, differential scanning calorimetry, infrared spectroscopy , and small and intermediate angle neutron scattering. Use of a statistical model, already shown to be informative for polyethylene [17] was made in order to help interpreting intermediate angle neutron scattering data. Also, a method of analysis of anisotropic small angle neutron scattering data from tilted samples derived by Sadler in 1983 [18] was used to determine any multiple occupancy of lamellae.

In the first chapter, we make a review of the structure and morphology of crystalline polymers. This initially concerns PE and iPS. The last section is a state of the knowledge on sPS. The different crystalline forms are reviewed, and morphological features are described. In chapter 2, we give a short introduction to the techniques : X-ray scattering, infrared spectrocopy, and differential scanning calorimetry, followed in chapter 3 by the description of the neutron scattering techniques used here. Chapter 4 and 5 concern our experimental results. In chapter 4, we present results from the techniques described in chapter 2, while neutron scattering results are presented in chapter 5. The latter is divided into three sections. The first section concerns small angle neutron scattering, the second intermediate angle neutron scattering and the last section anisotropic small angle neutron

scattering from tilted samples. We will finally bring together all these results in a final chapter where we will try to produce an overall picture of the structures of the δ- and the γ-phases and of the nature of the transition, and suggest future lines of investigation.

Chapter 1

Molecular Conformations in Crystalline Polymers

Background

There are two ways of growing a polymer crystal : melt crystallization and solution crystallization. For the former process, the type of structure usually obtained is called a spherulite. A spherulite is a spherical structure, with chain folded lamellar ribbons growing from the centre and twisting regularly. When crystallization occurs under stress (high pressure, elongational flow) shish-kebabs can be obtained. A shish-kebab consists of a central fibrous backbone (shish) with lamellar overgrowth (kebabs). In both the backbone and its overgrowths, the polymer molecules are primarily parallel to the shish-kebab axis. In the backbone polymer molecules are extended while in the overgrowth they are folded. Crystallization from dilute solution leads to single lamellar structures where folded chains pack together side by side to form the core of the crystal. Alternatively if stress is applied

(e.g. by stirring), shish-kebabs can be obtained. More concentrated solutions lead to the formation of a gel. A physical gel is a three dimensional network constituted of polymer molecules connected through van der Waals interactions and swollen by a solvent [19]. These gels are also called thermoreversible gels because the energy involved in the van der Waals interaction is of the order of kT so that these gels are thermoreversible.

Another type of complex formed between a polymer and a solvent can exist : clathrates. A clathrate is a form in which polymer molecules interact with solvent in the crystalline state and form inclusion compounds [20]. Inclusion can occur on both a stoichiometric and a non-stoichiometric basis. As examples of the former type, we can mention syndiotactic polymethylmethacrylate (sPMMA) which forms a clathrate with a variety of solvents [21], or poly(vinyl alcohol) (PVOH) with water [22]. Non-stoichiometic clathrates include, Poly(ethylene oxide) (PEO) which can form various crystalline complexes with inorganic and organic compounds [23], and syndiotactic poly(p-methylstyrene) (sPPMS) for which two kinds of clathrates have been distinguished, depending on the solvent [24].

A few polymers have been subjected to intensive research in order to determine the molecular conformation in the crystalline state, with the aim of understanding the crystallization mechanisms. The most widely studied is without any doubt polyethylene (PE). A whole section below is dedicated to this polymer for which the fundamental models of polymer crystals were built and refined.

For polymers with asymmetric backbone carbon atoms, one of the parameters which determines the ability of a polymer to crystallize is their tacticity. For polymers prepared from monomers of the general structure CH_2-CXY, where X and Y are two different

substituent groups, there are two distinct configurational arrangements of the monomer. The two stereoisomers (syndiotactic and isotactic) of the polymer cannot be converted by bond rotation. Tacticity is related to the distribution of the two isomeric forms of the repeat unit. Atactic polymers have a random placement of the two configurations. In isotactic polymers, all the repeat units have the same configuration, whereas in syndiotactic polymers the configuration alternates from one repeat unit to the next.

Following the work on PE, isotactic polystyrene became the subject of intensive research. Features derived from PE seemed to be adequate to describe the molecular conformation of this compound. Isotactic polystyrene also merits a whole section below.

The final section concerns the state of the knowledge about syndiotactic polystyrene. The structure of the different phases is described, including a clathrate. We are interested in establishing the links existing between the structural characteristics of sPS gels and sPS crystals. For this reason, we will also examine in detail syndiotactic polystyrene gels. Among the variety of techniques used to examine the structure and the morphology of sPS crystals, infrared spectroscopy distinguishes itself by its ability to characterise a particular configuration and to enable its evolution to be followed during any altering treatment. This subject will also be treated in a detailed review of the assigments of the infrared spectrum of sPS crystals.

1.1. Polyethylene

Polyethylene $\left[\left(CH_2\right)_n\right]$ has been widely studied. The most stable molecular configuration is the crystal with all trans bonds, i.e. the planar zigzag. The molecules pack into an orthorhombic unit cell (figure 1.1) and lie parallel to the c axis. A monoclinic modification which differs only in terms of molecular packing can be formed by mechanical deformation of orthorhombic polyethylene.
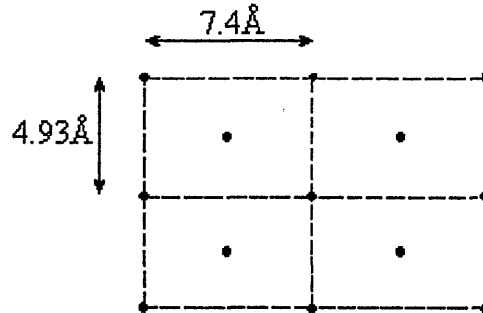
Figure 1.1.

PE unit cell.

In the lamellae, the polymer chains pack together side by side to form the crystal core. Because the chain length was usually much longer than the lamellar thickness, it was suggested by Keller [2] that the macromolecules fold many times upon themselves (figure 1.2.). The segment of polymer which traverses the lamella is usually called a stem. Stems of the same macromolecule are connected through folds.
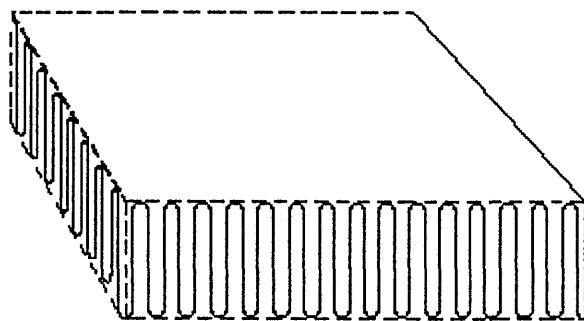
Figure 1.2.

An idealized polymer crystal (from ref. [1]).

Growth faces of solution-grown PE crystals were identified as [110] crystallographic planes by electron microscopy [25], indicating that folding occurs in this plane. This result was confirmed by infrared spectroscopy of blends of protonated and deuterated polyethylene [26] suggesting that in single crystals, nearest neighbour chains along the [110] directions are of the same isotopic composition. This indicates adjacent re-entrant folding. Painter et al. [27], in a FTIR study of the methylene wagging mode of PE found evidence for the existence of regular and tight structures characteristic of such folds.

A more detailed picture of the nature of the folds in solution crystallized PE was given by Patel and Keller [28]. It is possible to remove selectively the fold surface of the lamella by attacking it with a strong oxidizing agent, and to study the remaining material by gel permeation chromatography (GPC). By this way, the exact distribution of the fold length could be obtained. It appeared that some folds were present well beneath the surface ("buried folds") while other longer and looser folds stay well above it (figure 1.3.). Highest supercoolings seemed to favour the latter type of folding.
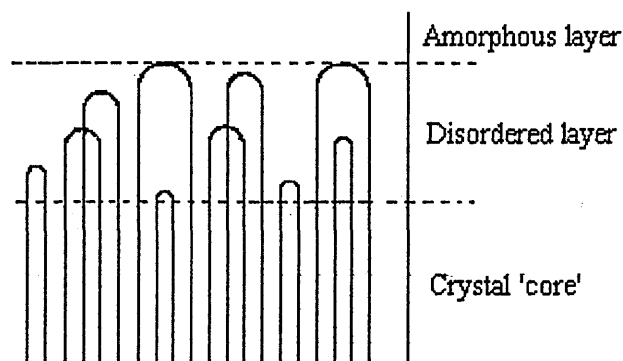
Figure 1.3.

The fold surface of the lamella showing the distribution of fold length and the presence of "buried folds" situated well bellow the average surface (from ref. [29]).

Polyethylene is the polymer most extensively studied by neutron scattering although it suffers from isotopic fractionation, believed to be due to the difference of about 4°C in the melting temperature between the deuterated and hydrogenated species. Schelten et al. [30] were the first to study melt crystallized PE by small angle neutron scattering. They concluded that molecules of the same species form clusters containing 15 to 30 of them, which disappear in the molten state. They pointed out the consequence of this "clustering" on the interpretation of infrared and neutron scattering results of isotopically mixed PE. They proposed a method to eliminate fractionation involving fast cooling from the melt [31]. They showed that, despite fractionation, deuterated molecules are uniformly distributed in both the amorphous and the crystalline regions of the semicrystalline material [31].

Sadler and Keller [3] studied solution grown polyethylene crystals. They used the analytical expressions for the intensity scattered by an isolated stem and a thin lamella in order to

interpret experimental curves. In this way, they extracted the thickness and the number of scattering centres per unit area of sheet. They showed that polyethylene stems are packed in sheets whose thickness agrees with that expected for neighbouring stems of one molecule being restricted to the same [110] plane. In these planes, the folding is largely adjacent re-entrant.

The conformations obtained for solution and melt crystallized polyethylene were compared by Sadler and Keller [4]. They confirmed that in solution grown crystals, the chains form sheets consistent with adjacent reentry folds. In this study, they also examined the effect of isotopic fractionation on the scattered intensity, answering the remarks of Schelten et al. [31]. Their results are consistent with the existence of large structures which scatter at low angles, where the scattering contrast is provided by H and D species. This is a particular case where the two components of a mixture differ only in their melting temperature, the other case being different molecular weights. The component with lowest melting temperature is ejected by the growing crystal and crystallizes at a later stage, forming a peripheral layer on the relevant crystal unit which thus becomes enriched in this component as shown in Figure 1.4. Instead of using the term "clusters" of Schelten [30], they described regions of enriched concentration.

Now that the basic scattering units are known to be stems in various arrangement, Sadler and Keller described a method which allows the calculation of the intensity scattered by any two dimensional arrangement of these stems [4]. Making use of this method, Spells and Sadler [5] built a statistical model for the arrangement of stems in sheets. In this model was incorporated the possibility of dilution of one molecule by others within a sheet, and also of
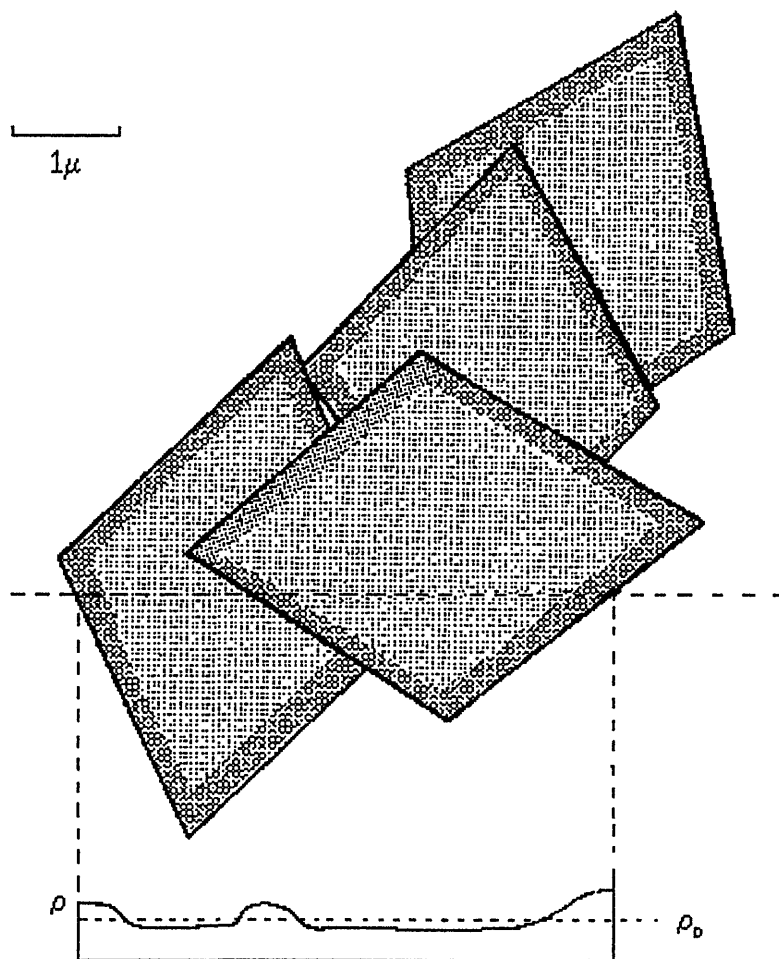
Figure 1.4.

Schematic representation of the large-scale structure for solution grown crystals of DPE and HPE blends. Below is drawn the variation of scattering density ρ about its average value ρ_0 (from ref. [4]).

superfolding. This feature appeared to be necessary after small angle neutron scattering measurements showed that radii of gyration were relatively insensitive to molecular weights ($R_g \propto M_w^{0.1}$). Sadler and Keller explained these results by the superfolding model where the chain folds back on itself [6]. In other words, superfolding means that on some

occasions a non adjacent fold involves a complete departure from a sheet, followed by
incorporation in a separate sheet (figure 1.5).
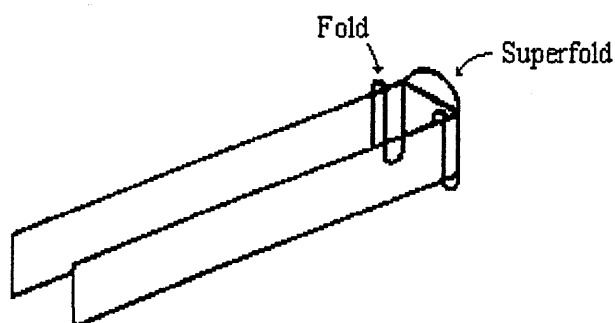
Figure 1.5.
The superfolding model.

In the model of Spells and Sadler, stems of a given molecule are placed in sheets
corresponding to a [110] crystallographic plane. The parameters describing the model are
the dilution ϕ (in other words, the proportion of lattice sites in the plane bounded by a
labelled molecule which are occupied by that molecule) and the probability of adjacent
reentry P_A. Another parameter was the number of sheets, in each of which the number of
stems was allowed to vary randomly. A dilution of 50% was chosen because it satisfies the
requirement for dilution by integers and is within the range previously determined from
SANS [4] (the number of scattering centers per unit area of sheet was lower by a factor of 2
than the value expected from adjacent reentry) and infrared data [32]. Results demonstrated
a strong statistical preference for adjacent reentry, with 75% of stems occupying adjacent
sites. The average length of a sheet of stems along the fold plane does not change much as
the molecular weight increases. Hence, the probability of a molecule folding back on itself
is relatively insensitive to molecular weight.

The labelling technique is also applicable to infrared spectroscopy in the case of polyethylene. A method enabling the calculation of splittings in the CD_2 bending vibrations, for irregular groups of labelled stems arising from the model [5] was developed by Spells [33]. Results obtained in this way confirmed previous findings in terms of probability of adjacency (75%) and dilution (50%). As stressed by Spells and Sadler [5], these effects certainly arise from the competition that takes place between different chains while depositing onto the crystallization growth plane.

Recently, Sonntag et al [17], built a statistical model that corrected one shortcoming of the previous one from Spells and Sadler (namely, the dilution was independent of the probability of adjacency), by adding another parameter which is the probability of having a labelled stem after an unlabelled one. Results from this model were in good agreement with neutron scattering from solution-grown polymer crystals and also with results from the previous model. They compared two situations: one with superfolding occuring after a specified number of labelled stems, which shows good agreement with experimental data for polyethylene. On the contrary, a model with superfolding occuring at random along the molecular length showed poor agreement. Sadler and Keller tried to consider a correlation between stems from adjacent sites [3], and demonstrated that this is less significant on neutron scattering intensities than the correlations of stem positions within a sheet.

Neutron scattering has demonstrated a marked difference in conformation between melt-grown and solution-grown polyethylene crystals [4]. The scattering curves are completely different and the intensities can differ by an order of magnitude. For melt-crystallized samples the chain stems scatter as almost individual entities. The more random

arrangement of stems implies something close to random fold reentry [4]. Melt quenched PE crystals have been shown to give IANS curves consistent with a "subunit" model of short groups of stems connected by longer folds [33, 34].

The behaviour of solution-grown polyethylene crystals upon annealing has also been studied by Sadler and Spells [35], and shows that at sufficiently low temperatures there is no melting during annealing. Small angle x-ray scattering on annealed solution-grown crystals of polyethylene showed that when the lamellar thickness increased by a factor of about 2, the radius of gyration from neutron scattering measurement remained constant. The stems lengths increased and their number decreased upon annealing, in a process which involves random removal of some of them, in order to keep their conformation within the sheets as well as the centres of gravity of the molecule unchanged. For the type of annealing studied (at $T_a \leq 123°C$ for 1h) the rearrangement is a solid state one, involving no melting even on a local scale. These results were confirmed by X-ray diffraction [36]. For a heating rate of $10°Cmin^{-1}$ and $T_a \leq 123°C$, the results were consistent with a localized solid state reorganization. Using a heating rate of $500°Cmin^{-1}$ for any T_a or using a heating rate of $10°Cmin^{-1}$ for $T_a > 123°C$, the results are consistent with larger scale melting. Sadler has developed a new technique of analysing anisotropic scattering signals [18], and applied it to small angle neutron scattering of isotopic mixtures of polyethylene crystallized from solution [18, 37]. It was deduced that between 123°C and 125°C there is a demarcation between sizes of mobile region: above, the regions are larger than molecules, below, they are smaller [37].

1.2 Isotactic polystyrene

Isotactic polystyrene (iPS) was synthesized first by Natta in 1955. Crystallinities of about 45% were obtained, and a high melting point ($\cong240°C$) characterizes this material. The crystalline structure of iPS has been described by Natta et al. [38]. The unit cell is rhombohedral and the chains take an helical configuration. In the unit cell, stems of different helicity are present (see figure 1.6.). Planes parallel to the {110} contain stems of the same helicity only, this helicity alternating from one plane to the next adjacent one. As for PE, there is a difference in the melting points between protonated iPS and deuterated iPS. A difference of 5.5°C has been found for samples crystallized at 180°C [38]. Despite this difference, isotopic fractionation is virtually absent. The chain conformation in iPS has been shown in many respects to be similar to that of PE.

Radii of gyration measurements carried out in the Guinier range by Guenet on samples crystallized in dibutylphthalate at 130°C gave $\alpha=0.91$ for the exponent of the relation $R_g \propto M^\alpha$ [40]. This indicated that the molecules are incorporated into sheet-like structures. Using an analytical expression for the radius of gyration, it was shown that the distance between two consecutive stems belonging to the same macromolecule was 12.6Å. This value does not correspond to the distance between first neighbours, but between second (see figure 1.6.). Under these conditions, reentrance occurs along the [110] plane which contains stems of the same helicity. This model gives linear rows of stems and was finally denoted [330]. The [330] model fitted the radii of gyration values well provided that the

sheet was continuous and uninterrupted. A simple test for the validity of this model was to check the presence of the predicted peak at the corresponding momentum transfer $q = 0.5\text{Å}^{-1}$. This test failed [8], and another model called the zigzag model was proposed. The zigzag model corresponds more closely to adjacent reentry because the folds occur alternately along the [010] and [100] directions so that the overall direction of the sheet is along the [110] plane. It must be emphasized that in this model the macromolecule alternates in helicity along its path. The observed dependance of R_g on molecular weight was not fitted by this model, suggesting that molecules are diluted in the sheet as in PE.

Other features derived from PE were found again in iPS crystals. These include superfolding, and incorporation of the macromolecule in more than one lamella [7]. The last feature was christened the "hinge-like model" by the authors. Guenet et al. tested the analytical expressions of the scattered intensity for these types of conformation for wide ranges of both molecular weights and crystallization temperatures. For low supercoolings, a single sheet conformation with dilution was adequate, independently of the molecular weight. With increasing supercooling, deviation from regular folding occurs. In a first stage superfolding appears, and for the highest supercooling and the highest molecular weights there is incorporation in more than one lamellae. To our knowledge, there are no published results for the value of the dilution and the probability of adjacency in iPS crystals.

a=21.9Å   b=21.9Å
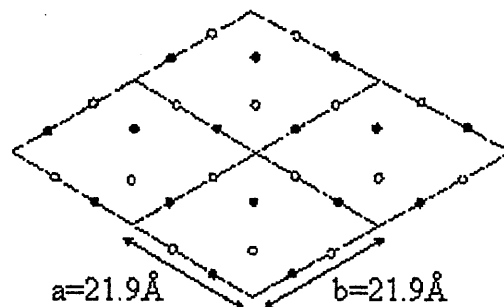
Figure 1.6.

iPS unit cell. Black points represent right-hand helix for instance and open circles left-hand helix.

1.3 Syndiotactic polystyrene

Ishira et al. [9] obtained for the first time in 1986 highly crystalline syndiotactic polystyrene (sPS) samples by using a specific catalytic system. This polymer presents a high melting temperature ($\approx 270°C$) and, unlike the isotactic polymer, crystallizes rapidly on cooling from the melt. These properties make this polymer of potential industrial interest. sPS is also of interest for its polymorphism. Structural studies on sPS have revealed that there are two types of chain configuration in the crystalline phases (cf. figure 1.7): a planar zigzag (TTTT) [9], and a twofold helix of type (TTGG)$_2$ [41]. Later, two crystalline forms containing molecular chains in a zigzag planar configuration and two crystalline forms containing molecular chains in helical configuration have been distinguished [42, 43]. Chatani et al. [10] confirmed that there are principally four distinct crystalline phases which they named in order of increasing stability: the molecular

19

compound, the helical form, the planar form I and the planar form II, which correspond respectively to the δ-, γ-, β- and α-phases in Guerra's notation [44]. It is this notation that we have finally adopted.

The sketch of the sample preparation methods and the connections between the different phases is relatively complex (figure 1.8.). The attained conformations and their relative contribution to the crystalline structure depend on the initial concentration, the solvent quality, the heating and cooling rates and, in some cases of the thermal history of the sample. Quenched extruded samples were obtained which were then annealed at 160°C, and their crystallinity was measured after different annealing times [45]. The maximum crystallinity reached for these samples was about 50%. Good agreement with this value was found using different techniques (Raman, WAXS, DSC and FTIR). Gianotti et al. [46] determined the fusion enthalpy of sPS and used this value to measure the crystallinity of samples crystallized without solvent under different thermal treatments. They give a value of about 40%, similar to what is normally found for iPS. These values are rather small in comparison to the 74% crystallinity given by Reynolds et al. [47] for a sample obtained by cooling slowly from the melt.

Recently, the existence of an empty δ-phase has been reported [10, 48]. This new phase, denoted δ_e, corresponds to a pure helical form of sPS, free from solvent. It can be obtained by extracting solvent molecules from the usual δ-phase with boiling acetone. Note that this phase is different from the γ-phase ; in particular it is not possible to reswell a sample in the γ-phase while it is for a sample in the δ_e-phase [49]. A patent has been granted

concerning separation of solvent mixtures and purification of vapour and liquid streams [15].
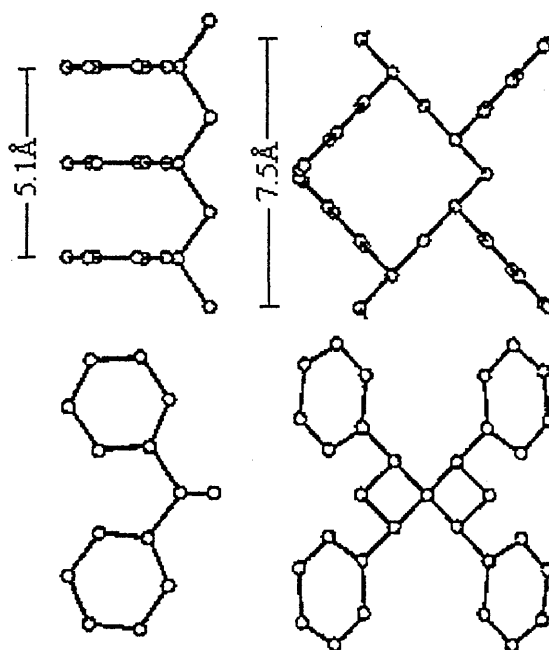
Figure 1.7.

Views perpendicular to (upper) and along (lower) the backbone of sPS in the TT (left) and TTGG (right) conformations (from ref. [50]).

1.3.1 The different forms of sPS crystals

The δ form is obtained either by solution crystallization or by swelling the amorphous polymer. Chatani et al. [10] have shown that the X-ray patterns were dependent on the solvent used for samples cast from solution, indicating that the solvent participates in the crystalline structure with sPS. They studied in more detail the crystal structure of the sPS crystallized from toluene [11] and iodine solutions [51]. They indexed their X-ray patterns
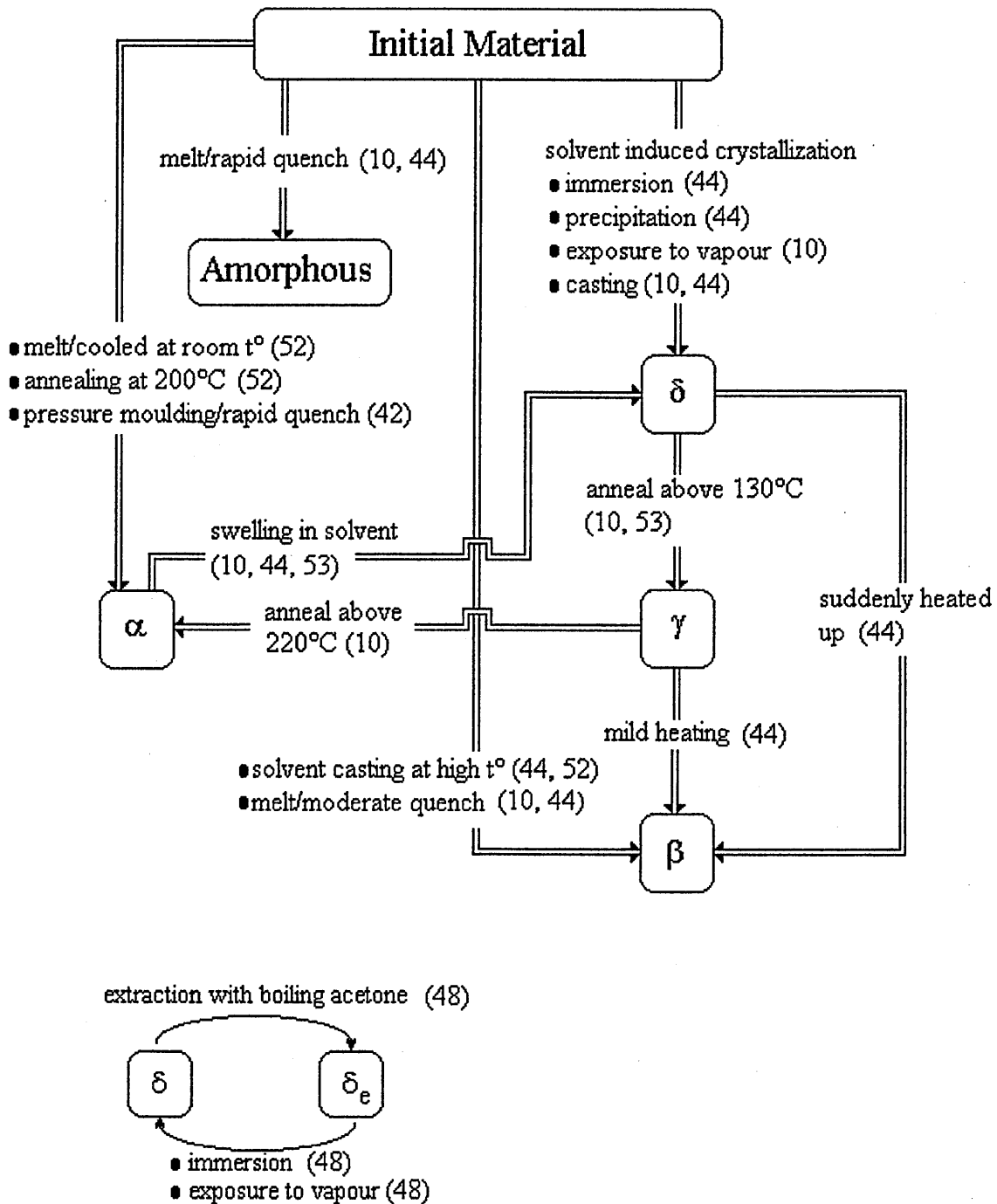
Figure 1.8.

Scheme of the sample preparation and polymorphism of sPS.

in terms of a monoclinic cell. The weight loss on heating and the density measurements yielded a molar ratio monomer/solvent of 4/1 for toluene and 2/1 for iodine. Their calculations of the crystal structure yield a model where the packing of the polymer chains enables solvent molecules to occupy an isolated hole between the phenyl groups of adjacent polymer chains (figure 1.9). On heating between 120 and 150°C, the δ-phase is transformed to another crystalline phase, the γ-phase. After this heat treatment, the X-ray fibre patterns were identical irrespective of the starting system. The chain repeat is retained and the unit cell is again monoclinic: thus the δ-form is transformed to a form consisting of the $(TTGG)_2$ helical chains free from solvent. However, the b-dimension of the γ-form is shortened by about 2Å, while the a-dimension is retained.

Further annealing brings the sample either to the α- or to the β-phase, depending on the heating rate [44]. The α- and β-phases belong respectively to the the hexagonal [12] and orthorhombic [54] systems. They can also be obtained by melt-crystallization [10, 44, 52]. The attained form depends on the cooling rate [44]. Guerra et al. [44] showed that the α- and β-phases can exist in different modifications characterized by differing degrees of structural order, so that two limiting disordered modifications (the α' and β') and two limiting ordered modifications (α" and β") have been described.

The phase behaviour of various sPS/solvent systems has been studied by Berghmans and co-workers [55], using DSC data. Necessarily, only a qualitative representation of the phase diagram is possible because of the non-equilibrium character of the systems. In general, a β-phase was reported to be the stable phase in poor solvents, with the δ-phase stabilised by good solvents. Intermediate solvent quality was found to give characteristics of an

δ with toluene [11]	γ [11]	δ_e [48]
Monoclinic	Monoclinic	Monoclinic
a = 17.58Å	a "is retained"	a = 17.4 Å
b = 13.26Å	b "is shortened by about 2Å"	b = 11.85 Å
c = 7.71Å	c "remains almost the same"	c = 7.70 Å
γ = 121.2°		γ=117°

Table 1.1.

Crystal structure of the different helical phases of sPS.

α [12]	β [54]
Hexagonal	Orthorhombic
a = 26.25Å	a = 8.81Å
c = 5.045Å	b = 28.82Å
	c = 5.06Å

Table 1.2.

Crystal structure of the different planar zigzag phases of sPS.

incongruent melting polymer/solvent compound. The structural relevance of the crystallization temperature was demonstrated from X-ray diffraction measurements on the sPS/ *trans* decalin system [56]: isothermal crystallisation at 60^0C and 90^0C resulted in diffraction patterns consistent with zigzag and helical chain configurations, respectively. In a wide study of the gelation of sPS, Guenet and co-workers have investigated the phase behaviour of sPS/benzene [57], sPS/toluene and sPS/chloroform [58] systems, using DSC with hermetically sealed pans. The experimental procedure involved inserting a piece of

the gel into a DSC pan and melting the sample in the pan before starting the measurements. Phase diagrams obtained in this way indicated the existence of two polymer/solvent complexes in the cases of benzene and toluene and at least one for the sPS/chloroform system. One of the complexes formed with toluene presented a stoichiometry identical to that given by Chatani et al. for the compound obtained by exposure to toluene vapour [11]. Neutron diffraction patterns were qualitatively consistent with the crystalline lattice proposed by Chatani et al. [11], although in the case of benzene one of the crystalline parameters appeared to be larger, probably linked to the high degree of solvation of the complex. The stoichiometry of the complexes identified was found to vary with solvent. A molecular model was proposed for the sPS/benzene [57] and sPS/toluene systems [58], with solvent molecules intercalated within the polymer helices.

A two step mechanism for the formation of the δ-phase was proposed [54]. In a first step, the random coils transforms into helices, which agglomerate in a second step to form the δ-phase. The solvent plays an important role in stabilizing the helix, and in impeding chain folding [57, 58].

Morphological studies which involved DSC, X-ray and thermogravimetric (TGA) measurements have been carried out in order to understand the δ- to γ-phase transition behavior in sPS. Wang et al. [16] report a ribbon-like morphology for sPS mats grown from dilute ethylbenzene solution at 50°C. This ribbon like morphology is destroyed during the transition from δ to γ which involves decomplexation. De Candia et al. [53, 59] observed the δ to γ transition for samples obtained by immersion of amorphous films in methylene chloride or dichloromethane. They report that the transition occurs through an intermediate

form which they suggest to be a mesophase, characterized by good configurational order and poor crystalline order. For a short review on mesomorphic forms of polymers, see for example the paper of Corradini and Guerra [58]. Another type of mesomorphic form was reported on sPS, involving this time the planar conformation [60, 61]. This mesomorphic form can be obtained by annealing an amorphous sample [62], by melt crystallization [63] and by stretching an amorphous film [61].

Infrared results [14, 64] showed that there is a partial loss of helical order upon the transition from the δ- to the γ-phase, which is recovered after the transition. NMR allows us to distinguish between the different phases of sPS [52, 65]. For samples in the δ-phase obtained by immersion of an amorphous film in dichloromethane, the mobility of the chains in the helical configuration is large in comparison to that of the chains in the zigzag configuration [52]. It was concluded that the presence of solvent molecules has the effect of loosening the crystalline packing. Also, chains in the bulk of the semicrystalline material were shown to have a mobility comparable to those in the amorphous component.

There is little in the literature about the fold direction in sPS crystals. Chatani et al [11] suggested that the lamellar crystals cast from the solution are extremely large in the a-direction, which could be the fold direction. This is based upon the abnormal orientation they observed in their drawn as-cast sample: this sample did not exhibit the [002] reflection corresponding to the chain periodicity, and what was the [$\bar{2}$10] reflection before drawing appeared on the meridian after drawing.

Stölken et al. [66] carried out the first SANS study of amorphous mixtures of protonated and deuterated sPS in order to study the influence of tacticity on the chain conformation
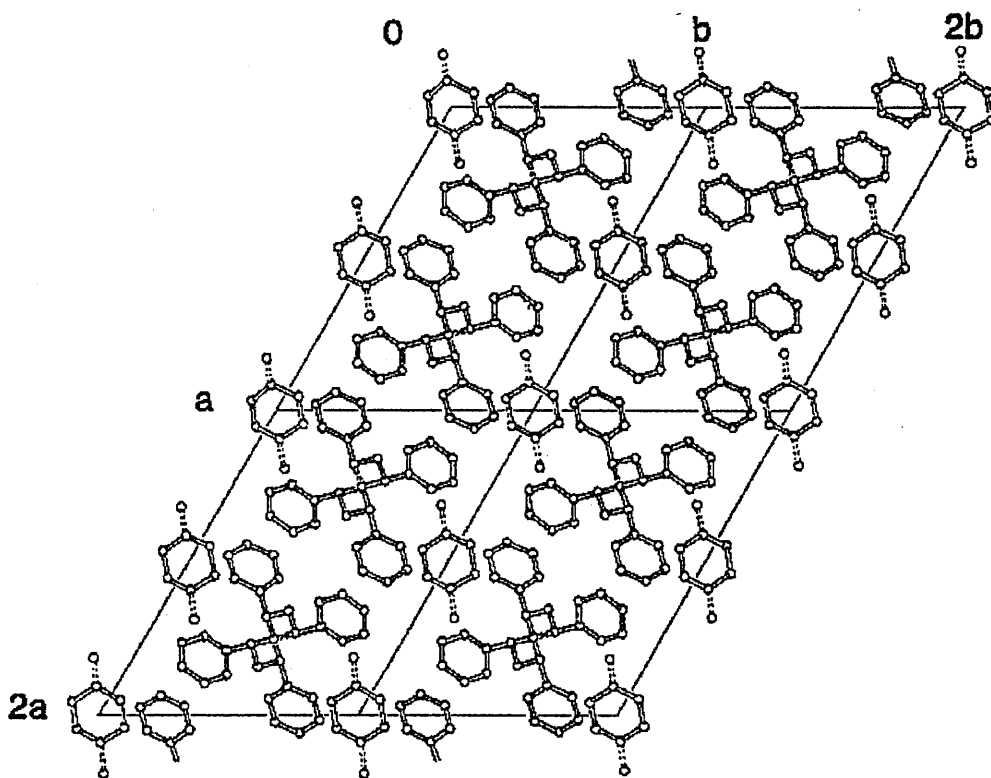
Figure 1.9.

Crystal structure of the δ-phase of sPS-with toluene viewed along the polymer chain axis (from ref. [11]).
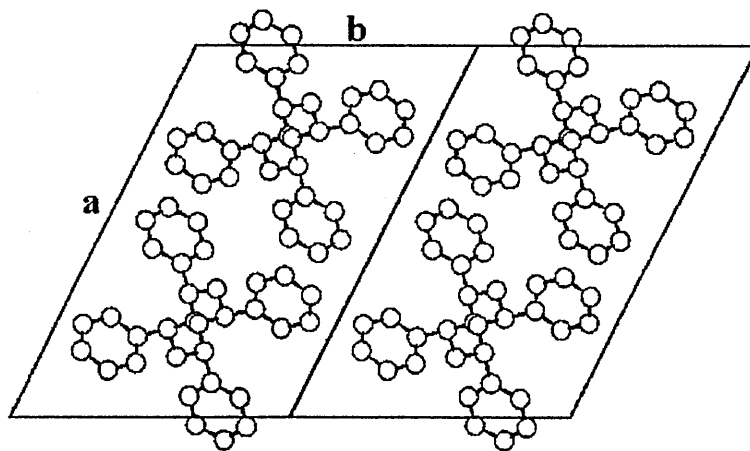
Figure 1.10.

Crystal structure of the empty δ-phase viewed along the polymer chain axis (from ref. [48])

a=26.25Å
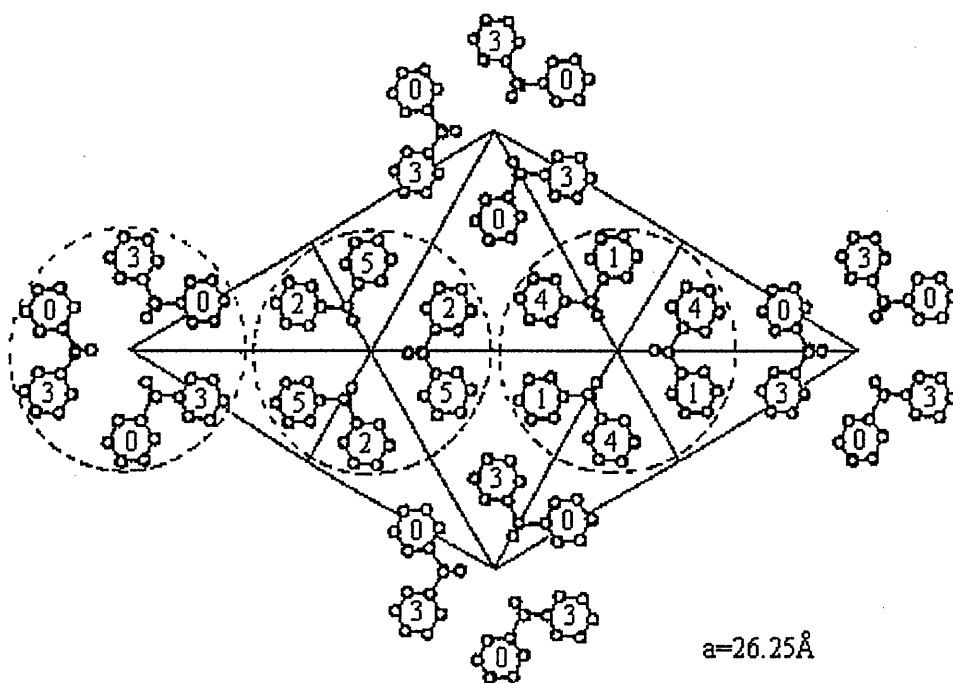
Figure 1.11.

Crystal structure for α" phase (limiting ordered) of sPS viewed along the polymer chain axis (from ref. [20]). The relative heights of the centers of the phenyl rings are indicated in c/6 units.

b=28.82Å

a=8.81Å
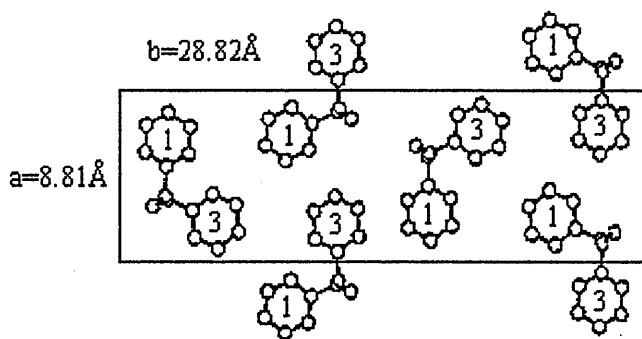
Figure 1.12.

Crystal structure for β" phase (limiting ordered) of sPS viewed along the polymer chain axis (from ref. [20]). The relative heights of the centers of the phenyl rings are indicated in c/4 units.

28

and to compare with predictions from the rotational isomeric state (RIS) model. Short-range steric interactions give rise to restrictions upon bond rotation. The RIS model assumes that each backbone bond configuration is restricted to one of three discrete rotational isomeric states corresponding to potential energy minima. If we go back to the Stölken measurements, the measured characteristic ratio $C_\infty = \langle R_0^2 \rangle / (nl^2)$ which is related to the stiffness of the polymer chain ($\langle R_0^2 \rangle$ mean square end to end distance, n number of monomers, l^2 mean square monomer length) did not agree with the prediction from the RIS model. In addition, the Kratky plots showed well-pronounced plateaux characteristic of chains with Gaussian statistics instead of the expected steady increase predicted by the RIS model.

1.3.2. Infra-red analysis

In the following section, we summarize the state of the knowledge concerning the assignment of the IR spectrum of the different forms of sPS crystals. We distinguish between the non-configurationally sensitive and the configurationally sensitive bands. The former are mostly phenyl ring modes and will be helpful for the normalization of the spectra and for the determination of the concentration in isotopic species in deuterated samples. The latter are mostly backbone modes and are used as the key bands for the identification of crystal modifications.

1.3.2.1 Non-configurationally sensitive bands

The phenyl ring modes are independent of chain configuration [67, 68]. This applies to ring C-H stretching, some ring C-H out-of-plane wagging and ring C-C torsion modes. Reynolds et al. [47] used the integrated intensities of the bands at 1601 cm^{-1} and 1585 cm^{-1} to normalize their spectra. These two bands are assigned to the benzene ring stretching vibrations [67, 69]. They are expected at the same frequencies for the planar and zigzag forms [68]. Two bands at 2922 and 2946 cm^{-1} assigned to backbone CH$_2$ stretching [67, 69] are also non-configurationally sensitive [68]. They will be helpful for the determination of the concentration in blends with deuterated polymer (vide infra).

1.3.2.2 Configurationally sensitive bands

The first clues available in the process of assigning a spectrum are the appearance/disappearance of certain bands when changing configuration. These changes of configuration can be obtained by heat treatment. Helpful information can also be obtained by comparison with the spectra of a similar compound such as iPS. Finally, the exact origin of a band can be obtained on the basis of normal mode calculations. Among the published work on infrared analysis of sPS, we can mention the studies of Kobayashi et al. [50], Reynolds et al. [47, 70], Vittoria [71], Rastogi and Gupta [67, 68] and Nyquist et al. [69].

In the infrared analysis of samples obtained by immersion in dichloromethane [71], seven bands were listed which are present neither in planar nor in amorphous samples. Thus, they

must arise from the helical configuration of the chains. These bands are reported at 1440, 1278, 1170, 935, 767, 576 and 499 cm^{-1}. Similarly, two bands at 943 and 934 cm^{-1} have been assigned to the helical configuration [47, 70]. This is based on the comparison between spectra from the helical and planar configurations which show that this doublet disappears "almost completely" in the latter form [61]. Reynolds et al. [70] also concluded that the bands observed at 769, 571 and 548 cm^{-1} have to be associated with the helical configuration. This conclusion is based on the increase of the intensity of these bands upon annealing (up to 185°C), which they interpret as due to an increase in crystallinity of the helical phase. After annealing at 200°C, which brings these samples into the all-trans configuration, only a single band remains in this region.

The band at 539cm^{-1} appearing in the planar zigzag samples shows an increasing intensity upon annealing or drawing confirming that it is due to a long sequence of trans isomers [70]. Thus this band is usually assigned to the planar zigzag structure. Melt crystallized samples have shown a strong infra-red band at 1220 cm^{-1}, which disappears after heating the sample to the amorphous state [9, 71] which contains an essentially random distribution of trans and gauche configurations. Vittoria [71] showed that this band also disappears in the helical form. Thus this band is usually assigned to the planar zigzag structure.

The band observed at 1220 cm^{-1} is assigned to the planar zigzag structure, and more precisely to a complex skeletal mode including methyne CH deformation δ(CH) [50, 67]. The comparable mode for TTGG sPS is assigned by Kobayashi et al. at 1277 cm^{-1} [50].

The study of Jasse et al. [72] of polystyrene model compounds showed that a band at 540 cm^{-1} is observed when at least three backbone bonds are in trans configurations, whereas a

band at 554 cm^{-1} is assigned to a second configuration containing a gauche isomer. This has been confirmed by Rastogi et al [67] who calculated the frequencies of these two modes at 547 cm^{-1} and 552cm^{-1} respectively. Thus the 540 cm^{-1} band is consistent with an all-trans structure [70]. The corresponding band for the TTGG configuration is assigned at 576 cm^{-1} by Rastogi et al. [68], or at 548 cm^{-1} by Reynolds et al. [70] and Kobayashi et al. [50]. The 572 cm^{-1} band for the TTGG form was assigned to an in-plane ring and ring C-H in-plane-deformation, with no corresponding band in the TT configuration, whereas the 537 cm^{-1} band in the all-trans form and the 536 cm^{-1} bands in the TTGG form were assigned to skeletal and in plane ring modes.

Nyquist et al. [69] observed a band for their helical sPS samples at 538.9 cm^{-1} (544.2 cm^{-1} in the all-trans form) and assigned it as an out of plane ring deformation. They assigned a peak at 572.1 cm^{-1} (540 cm^{-1} in the all-trans form) to an in-plane ring deformation.

The 769 cm^{-1} band is expected from Rastogi's calculation to arise from ring bending and deformation in agreement with Kobayashi et al. [50] who assign it to a mode involving skeletal and in-plane ring deformation. Nyquist et al. [69] observed a peak at 768 cm^{-1} (764 cm^{-1} in the all-trans spectrum) which they suggested to be associated with CH_2 rocking. Nyquist [69] et al. assigned the band they observed in their helical sample only at 932.3 cm^{-1} and the one at 945.3 cm^{-1} in the TTGG form (at 940 cm^{-1} in the TT form) to combinations of out-of-plane ring deformation. Rastogi et al. [68] calculated a backbone mode frequency at 929 cm^{-1} corresponding to the bands observed at 935 cm^{-1}. Another backbone band calculated at 944 cm^{-1} could correspond to the band observed at 945cm^{-1}. Both these bands were assigned to backbone $C-C-H$ bending and backbone $C-C$

stretching. Configurationally insensitive and sensitive band observations and assignments are summarized in tables 1.3 and 1.4.

sPS TT reported [69]	sPS TTGG reported [69]	sPS Calculated [67, 68]]	Assignment [67, 68, 69]
1601.9	1601.1	1608	ring C-C stretch and
1583.5	1583.2	1576	ring H-C-C bend
2923.11	2924.0	2930	backbone CH_2 stretch
2847.0	2846.0	2889	

Table 1.3.

Some useful non-configurationally sensitive bands and their assignments. Values given in column 3 are valid for both the planar and helical forms.

TT	TTGG	Assignment
1454 [68]	1440 [71] 1442 [68]	H-C-C bend, backbone C-C-H bend [68]
1224 [50] 1221.85 [69]	1277 [50, 71] 1275.3 [69]	skeletal mode, CH deformation [50, 69]
940 [69]	945.3 [69, 70, 71] 932.3 [69, 70, 71]	out-of-plane ring deformation[69] backbone C-C-H bend, backbone C-C stretch [68] out-of-plane deformation [69] backbone C-C-H bend, backbone C-C stretch, ring C-C stretch [68]
764 [69] Not obtained [67]	768 [69, 71] 769 [50] 767 [67]	CH_2 rocking [69] skeletal, in-plane ring [50] ring bend and deformation [67]
540 [67] 569.0 [69] 539 [70]	576 [67, 71] 572 [50] 572.1 [69] 548 [70]	ring C-C-C bend, ring H-C-C bend [67] in plane ring [50] and ring CH in-plane deformation [50, 69] ring C-C-C bend, ring H-C-C bend [70]
537 [50]	536 [50]	skeletal, out-of-plane ring mode, ring CH out-of-plane deformation [50]
544.2 [69]	538.9 [69]	out of plane ring deformation [69]
	499 [71]	ring C-C-C bend, backbone C-C-ring C bend, backbone C-C-H bend

Table 1.4.

Observed configurationally sensitive bands of sPS and their assignment.

Chapter 2

Techniques

Introduction

The purpose of this chapter is to give a quick introduction to the techniques we used for the characterization of polymer crystals, namely WAXS, SAXS, FTIR and DSC. WAXS allows the determination of the molecular structure of the crystal. SAXS gives access to the most characteristic dimension of the lamella : its thickness. Infrared spectroscopy gives information about the molecular configuration. The thermal behaviour can be studied by DSC which provides information about the transition occuring upon heating of a sample. For more detailed studies of these techniques see references [73, 74, 75] about X-ray diffraction, [19] and [76] about DSC, and [77] about FTIR.

2.1. X-Ray scattering

2.1.1. Wide Angle X-Ray Scattering

When a monochromatic X-ray beam is incident on a crystal, the scattered X-rays from the regularly placed atoms interfere with each other, giving strong diffraction signals in particular directions. The directions of the diffracted beams are related to the shape and dimensions of the unit cell of the crystalline lattice, and the diffraction intensity depends on the disposition of the atoms within the unit cell.

2.1.1.1. Bragg's law

A crystal consists of a three-dimensional array of unit cells. If the primitive translations of the space lattice are represented by the vectors **a**, **b** and **c**, then the reciprocal lattice is defined by vectors **a***, **b*** anc **c*** in reciprocal space where

$$\mathbf{a^*} = \frac{\mathbf{b} \times \mathbf{c}}{V} \qquad \mathbf{b^*} = \frac{\mathbf{c} \times \mathbf{a}}{V} \qquad \mathbf{c^*} = \frac{\mathbf{a} \times \mathbf{b}}{V} \qquad (2.1)$$

Where V is the volume of the unit cell. A general property of the reciprocal lattice is that the vector s(hkl) from the origin to any lattice point (hkl) is perpendicular to a set of parallel planes in the real lattice which intersect **a**, **b** and **c** axes at intervals of a/h, b/k and c/l respectively. The spacing between subsequent planes is d = 1/s. These planes are called

Miller planes and (hkl) are the Miller indices. The angle of diffraction 2θ of the incident

beam diffracted by a particular set of Miller planes is given by Bragg's law

$$2d \sin\theta = n\lambda \qquad (2.2)$$

where d represents the interplanar spacing, λ is the wavelength of the radiation and n

indicates the order of diffraction.

2.1.1.2. Scattering amplitude

The amplitude F of diffraction in a certain direction (specified by **s**) is the Fourier

transform of the electron density distribution within the object.

$$F(\mathbf{s}) = \sum_{j=1}^{N} f_j \exp(2\pi i \mathbf{s} \cdot \mathbf{r}_j) \qquad (2.3)$$

Here f_j is the atomic scattering factor for the jth atom. If the object is continuous, the set of

discrete points at positions r_j can be replaced by an electron density distribution $\rho(\mathbf{r})$ and

equation (2.3) can be rewritten as

$$F(\mathbf{s}) = \int \rho(\mathbf{r}) \exp(2\pi i \mathbf{s} \cdot \mathbf{r}) dv \qquad (2.4)$$

The functions $\rho(\mathbf{r})$ and $F(\mathbf{s})$ are Fourier transforms of each other,

$$\rho(\mathbf{r}) = \int F(\mathbf{s}) \exp(-2\pi i \mathbf{r} \cdot \mathbf{s}) ds \qquad (2.5)$$

The integral presented in equation 2.5 has to be taken over all elements of reciprocal space.

If x_j, y_j and z_j are the fractional coordinates of the N atoms in the unit cell then

$$\mathbf{r}_j = x_j \mathbf{a} + y_j \mathbf{b} + z_j \mathbf{c} \qquad (2.6)$$

The corresponding vector **s** in reciprocal space may then be written

$$s = ha* + kb* + lc*$$ (2.7)

The unit cell structure factor, pertaining to the reflection (hkl), is then

$$F(hkl) = \sum_{j=1}^{N} f_j \exp\left[2\pi i(hx_j + ky_j + lz_j)\right]$$ (2.8)

2.1.1.3. Systematic absences

If the unit cell contains a number of identical groups related by certain symmetry operations, certain hkl reflections will be absent, for which there will be a systematic relationship in the h, k or l indices. These absences or space group extinctions are helpful in attempting to assign a space group symmetry to the structure.

2.1.1.4. The Ewald construction sphere

In figure 2.1, let the scattering object be placed at O, where O is also considered to be the origin of the reciprocal space connected with the object. The primary beam of wavelength λ is directed along PO, on which line, at a distance of $1/\lambda$ from O, the midpoint M of a sphere of radius $1/\lambda$ is positioned. Accordingly, this sphere, which is generally called the Ewald sphere, will pass through O. Each point X on the surface of this sphere will then represent a point in the reciprocal space around O from which a diffracted beam of wavelength λ can be obtained. The direction of the beam will be MX, whereas the actual

38

path of the beam will be OX', where OX' is parallel to MX. From figure 2.1 it follows that the length of the scattering vector is OX which is equal to $2\sin\theta/\lambda$.
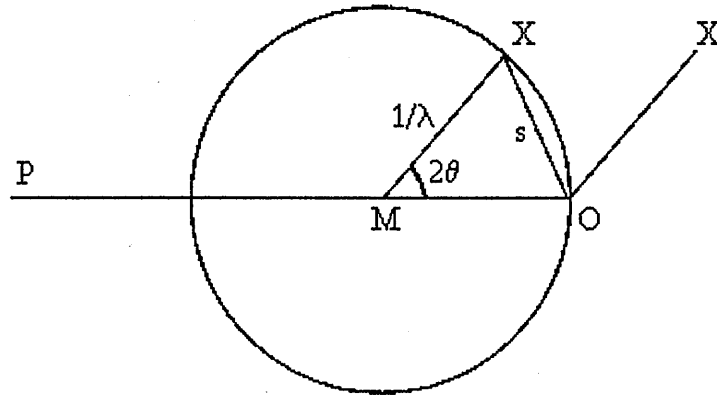
Figure 2.1.

The Ewald sphere construction.

When the crystallites are uniformly distributed at all orientations about a common axis (such as in fibres or sedimented mats), the arrangement is analogous to a single crystal rotated about the c axis (figure 2.2.a). Bragg's law will be satisfied where the circles intersect the Ewald sphere (figure 2.2.b). The layer lines allow periodicities along the fibre axis c to be separated from periodicities along a and b. The basic problem in indexing the X-ray patterns is to disentangle sets of hk reflections for successive values of l.

This construction is extremely helpful in surveying the effects of changing the experimental conditions. Thus, rotation of the object involves rotation of the connected reciprocal space, which will bring new points in this space on the surface of the Ewald sphere, and thereby into a diffracting position.
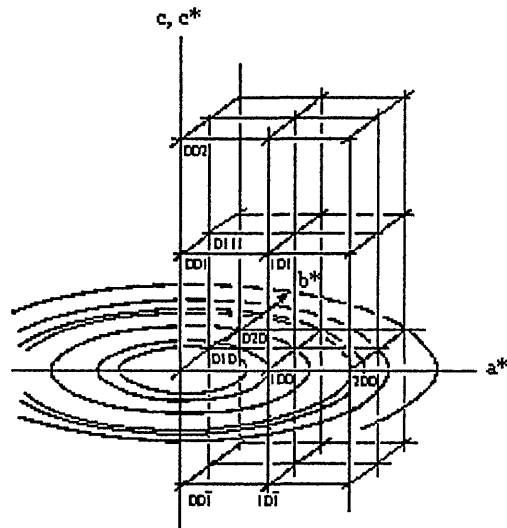
Figure 2.2.a.

Reciprocal lattice of a crystallite with concentric circular distribution of reciprocal lattice points in the equatorial (a*b*) plane (from ref. [75]).
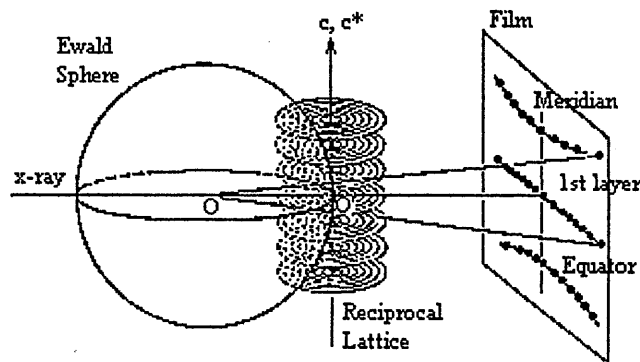
Figure 2.2.b.

Geometric relationship between the distribution of reciprocal lattice points and the fibre diffraction pattern (from ref. [75]).

40

2.1.1.5. Indexing the X-Ray pattern

In this study, we used a flat film camera and the sample was positioned so as to have the mat normal perpendicular to the beam. This geometry is called "edge on". When the sample is placed with this axis parallel to the beam, the geometry is called "flat on".
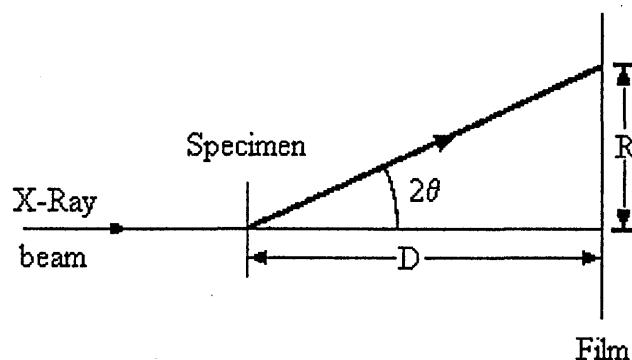
Figure 2.3.

Geometry of flat film recording.

Figure 2.3 illustrates the geometry of the flat film camera. The pattern obtained will consist of 4 symmetric quadrants, in each of which the diffraction arcs are part of circles The diameter 2R of each circle is measured and the Bragg angle is calculated using

$$\tan 2\theta = \frac{R}{D} \qquad (2.9)$$

where D is the specimen to film distance.

Finally the d-spacing of a reflection is given by

$$d = \dfrac{\lambda}{2\sin\left[\dfrac{1}{2}\tan^{-1}\dfrac{R}{D}\right]}$$

(2.10)

The c value is directly found from the layer line spacing. The reflections on the equator have index l = 0, on the first layer l = 1, and so on. The measured d-spacings are compared with those calculated for various sets of hkl planes of unit cells with different structure and dimensions. For example, for a monoclinic structure (a ≠ b ≠ c, $\alpha = \gamma = 90°$, $\beta \neq 90°$), the interplanar spacing is

$$d_{hkl} = \left(\dfrac{\dfrac{h^2}{a^2}+\dfrac{l^2}{c^2}-\dfrac{2hl\cos\beta}{ac}}{\sin^2\beta}+\dfrac{k^2}{b^2}\right)^{-\frac{1}{2}}$$

(2.11)

When good agreement is found, hkl values are assigned to the reflections, and the unit cell parameters are refined using least squares procedures. Once the assignment of the reflections has been done, the atomic positions of the atoms in the lattice cell have to be determined. For a known postulated structure, F(hkl) can be calculated using equation 2.8 and the product FF* can be compared with the measured intensities.

2.1.2. Small Angle X-Ray Scattering

Semicrystalline polymers are ideal objects to be studied by small angle X-ray scattering. First, they show electron density variations for which the correlation length is usually well within the range covered by this technique. Secondly, their structure may in many cases be

42

adequately described by assuming the electron density variations to occur in one direction only. When lamellar single crystals are allowed to settle out from solution they form a solid mat of crystals with a preferred parallel orientation. In the case of isothermal crystallization, crystals have approximately a constant thickness. The periodicity of the stack in the mat is related to both the crystal thickness and the degree of crystallinity. The densities of crystal and amorphous material, and hence their electron densities, are different. The regular alternation of crystalline regions from the stacks of lamellar crystals gives rise to a periodic variation in electron density. The stack scatters X-rays in a similar way to the atoms in a crystal lattice and Bragg's law is obeyed. The diffraction peaks can be associated with the various orders of the Bragg reflection from the lamellae, and the average value of the period l_x, which is the sum of the average thickness of the crystalline and amorphous layers, can be obtained using Bragg's law. For small angle scattering, this can be approximated by

$$l_x \cdot 2\theta = n\lambda \qquad (2.12)$$

where λ is the wavelength of the X-rays, 2θ is the scattering angle of the peak, n its order. The possibility to observe high orders will depend on the regularity of crystal stacking.

2.2. Infrared spectroscopy

2.2.1 Infrared spectroscopy of polymers

Infrared spectroscopy is an important tool which can be used for the identification of

molecules and analysis of molecular structure. These molecular vibrations occur in the infrared region of the electromagnetic radiation spectrum from $\approx 1 \times 10^{12}$ Hz to $\approx 300 \times 10^{12}$ Hz (≈ 3 cm^{-1} to 10^4 cm^{-1}).

Infrared spectroscopy is a technique used to examine the vibrational modes of polyatomic molecules, the incident infrared energy being absorbed at the frequency of the vibration. The number of vibrational modes produced by a molecule is 3N-6 or 3N-5 for linear molecules, where N is the number of atoms in the molecule, and so for example CO_2 has 4 vibration modes. For a vibrational mode to be infrared active, there has to be a change in the dipole moment $\Delta\mu$ of the molecule during the vibration, i.e.

$$\Delta\mu = qr \neq 0 \qquad\qquad (2.13)$$

where r is the displacement of the centre of charge and q is the charge. This can be affected by the symmetry of the molecule; the higher the symmetry the molecule possesses, the less probable it becomes that there will be a change in dipole moment. Also because of the symmetry elements present in a molecule, many vibrations could be degenerate. Figure 2.4 shows the vibrational modes present in carbon dioxide, namely 2 stretching and 2 bending vibrations. In fact, of the stretching vibrations only the asymmetrical vibration gives rise to a change in dipole moment $\Delta\mu$ and so only this vibration is visible in the infrared spectrum. The bending vibrations both give rise to a change in dipole moment and therefore are both infrared active, but the symmetry of the CO_2 molecule makes these vibrations identical, and therefore degenerate, so only one bending vibration is seen in the infrared spectrum. So from the four vibrations only two are seen in the infrared spectrum. Along with the low

intensity of some vibrational modes, this reduces the number of vibrations observed in the infrared spectrum of any polyatomic molecule.

Let the masses of the atoms in a diatomic molecule to be m_1 and m_2 and let their separation be r. In the harmonic approximation, the potential energy V(r) of the molecule is given by

$$V(r) = V_0 + \frac{1}{2}k(r - r_0)^2 \qquad (2.14)$$

where V_0 and k are constants and r_0 is the equilibrium separation of the atoms, it is easy to show that when the molecule is disturbed from equilibrium it will vibrate with simple harmonic motion of frequency v, where

$$v = \frac{1}{2\pi}\sqrt{\frac{k(m_1 + m_2)}{m_1 m_2}} \qquad (2.15)$$

The quantity k is called a force constant.
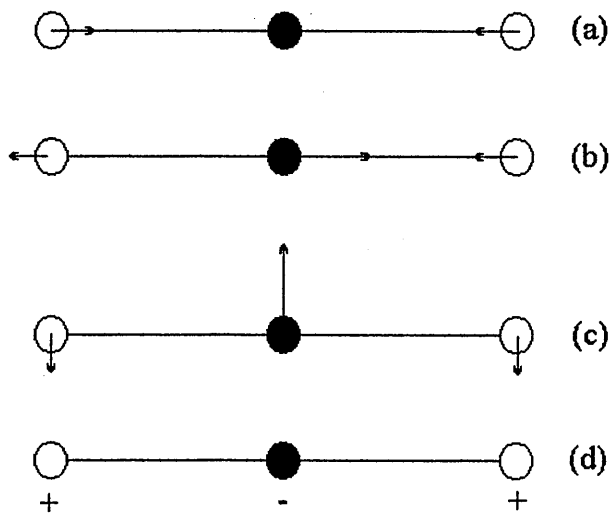
Figure 2.4

Normal modes of vibration of CO_2. (a) symmetric stretch ; (b) antisymmetric stretch ; (c) and (d) bend.

2.2.2 Configurational sensitivity

Many of the functional groups present in molecules, such as $C-H_2$, vibrate at approximately the same frequency irrespective of the molecules to which the group is attached. For polymeric molecules, there are some configurationally sensitive bands which originate from the intramolecular vibrational coupling between the monomeric units regularly arranged along the polymer chain. For example in iPS, it was shown that a particular sequential length of the TG, TT or TTGG configuration was responsible for the appearance of certain configurationally sensitive bands [78]. The critical sequential length necessary for the band to arise depends on the vibrational mode from which the band originates.

2.2.3 Fourier transform infrared spectrocopy

2.2.3.1 Principle

Originally, IR spectra of polymers were recorded using a dispersive instrument equipped with an optical element of a prism or grating to disperse the infrared radiation. Using a scanning mechanism, the dispersed radiation is passed through a slit system which isolates the frequency range falling on the detector. In this manner, the spectrum i.e. the energy transmitted through a sample as a function of frequency, is obtained. This dispersive IR method is severely limited in sensitivity because most of the available energy is thrown

away because it does not fall on the slit aperture and hence does not reach the detector. To improve the sensitivity of an infrared instrument, a multiplex optical device was sought which allows the continuous detection of all the transmitted energy simultaneously. The Michelson interferometer (which is described in detail in the next section) is such an optical device and the IR instrumentation which resulted is termed a Fourier Transform Infrared (FTIR) Spectrometer. An important advance was made with the discovery of the Fast Fourier Transform (FFT) algorithm by Cooley and Tukey [79] and also with the introduction of cheaper and more powerful microcomputers.

2.2.3.2 The Michelson interferometer

At the heart of a Fourier transform spectrometer is a Michelson interferometer. A Michelson interferometer is an optical device which can divide a beam of radiation into two paths and then recombine them so that the intensity variations at the exit can be measured by a detector as a function of path difference. The simplest form of the interferometer is shown in figure 2.5. It consists of two mutually perpendicular plane mirrors, one of which can move along its normal. The movable mirror is either moved at a constant velocity or is held at equidistant points for short, fixed periods of time and rapidly stepped between these points. Between the fixed mirror and the movable mirror is a beamsplitter, where a beam of radiation from an external source can be partially reflected to the fixed mirror (at point F) and partially transmitted to the movable mirror (at point M).

After each beam has been reflected back to the beamsplitter, they are again partially transmitted.

To understand the process occuring in a Michelson interferometer, let us first consider an idealised situation where a source of monochromatic radiation produces an infinitely narrow, perfectly collimated beam. If the fixed and movable mirrors are equidistant from the beamsplitter, no path difference exists between the two beams. They interfere constructively for path differences equal to any integral multiple of the wavelength λ . In the case of path differences equal to $(n + 1/2)\lambda$, the two beams interfere destructively and for a monochromatic source of intensity $I(\overline{v})$, the intensity of the transmitted beam through the interferometer as a function of optical path difference, or retardation, x(cm) is given by

$$I(x) = 0.5I(\overline{v})(1 + \cos 2\pi \overline{v} x) \qquad (2.16)$$

Fixed mirror

Movable Mirror

M

Source

Direction of motion

Beamsplitter

Detector
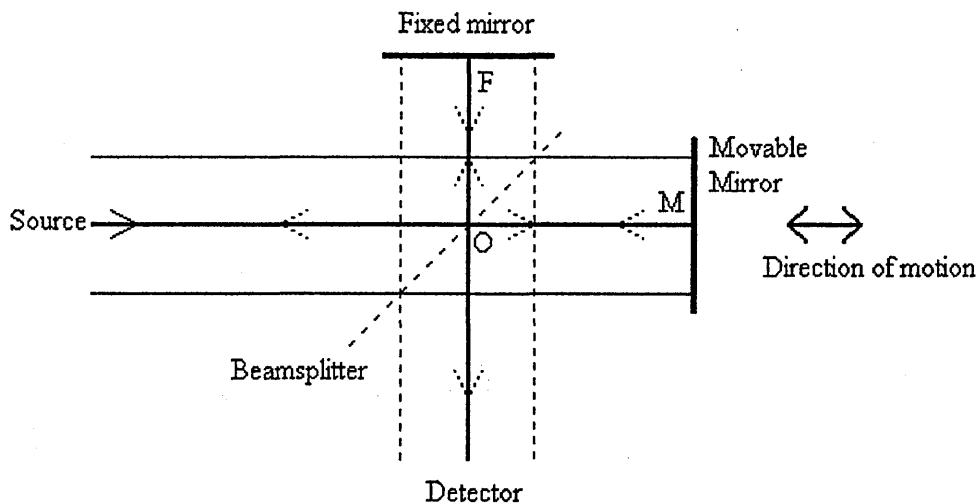
Figure 2.5

Schematic diagram of a Michelson interferometer.

In a scanning Michelson interferometer, the optical path difference x is varied by moving one mirror at a constant velocity v. It can be seen that I(x) is composed of a constant (dc) component equal to $0.5I(\bar{v})$ and a modulated (ac) component equal to $0.5I(\bar{v})\cos\pi\bar{v}x$. Only the ac component is important in spectrometric measurements, and it is this modulated component that is generally refered to as the interferogram, I(x). In the case of a polychromatic source, the interferogram is the sum of the individual interferograms due to each wavenumber, i.e.

$$I(x) = 0.5\sum_{i=1}^{n}I(\bar{v_i})\cos 2\pi\bar{v_i}x \qquad (2.17)$$

And if we consider a continuous source, the interferogram is the integral of the contributions from all wavenumbers in the spectrum.

$$I(x) = 0.5\int_{-\infty}^{+\infty}I(\bar{v})\cos 2\pi\bar{v}xd\bar{v} \qquad (2.18)$$

In practise, the amplitude of the interferogram as observed after detection and amplification is proportional not only to the intensity of the source, but also to instrument characteristics (detector response, beamsplitter efficiency, etc.). These factors remain constant for a given configuration and equation 2.18 can be expressed as

$$I(x) = \int_{-\infty}^{+\infty}B(\bar{v})\cos 2\pi\bar{v}xd\bar{v} \qquad (2.19)$$

where $B(\bar{v})$ represents the intensity of the source at a frequency $\bar{v}$ cm^{-1} taking into account the instrumental characteristics. It can be seen from equation 2.19 that I(x) is the cosine Fourier transform of the spectrum $B(\bar{v})$ which can be recovered by taking the Fourier transform of I(x)

$$B(\overline{v}) = \int_{-\infty}^{+\infty} I(x) \cos 2\pi \overline{v} x dx \qquad (2.20)$$

In practise, data acquisition involves signal-averaging of interferograms and requires that the signals are added coherently. For this purpose, the interferogram of a monochromatic source (He-Ne laser) is measured along with the main interferogram. The different interferograms can be digitised at exactly the same position during each scan by sampling at each zero value of the sinusoidal reference interferogram arising from the He-Ne laser. It is however necessary for the first data point to be sampled at an identical retardation for every scan. This is achieved using a third interferogram arising from a white light source. The very sharp interferogram produced by this source gives a reproductible marker at the same retardation, and whenever this interferogram exceeds a certain threshold voltage, data collection begins at the next zero crossing of the laser reference interferogram.

2.2.4 Fourier self deconvolution

Fourier self-deconvolution involves the deconvolution of an intrinsic lineshape function from the experimental spectrum. Convolution is essentially the smearing of one line shape by another. It is assumed that the spectral resolution obtained is limited by the natural lineshape rather than by instrumental factors. A spectrum $E(v)$ is derived from an interferogram $I(x)$ as $\Im\{I(x)\}$; where $\Im$ symbolizes a Fourier transformation. The self-deconvoluted interferogram, $I'(x)$ is then expressed as

50

$$I'(x) = \frac{D_g(x)}{\mathfrak{I}^{-1}\{E_0(\nu)\}} I(x) \qquad (2.21)$$

where $E_0(\nu)$ is the intrinsic lineshape function and $D_g(x)$ is an apodization function. $\mathfrak{I}^{-1}$ denotes an inverse Fourier transformation. The denominator represents the deconvolution, with $D_g(x)$ determining the final lineshape. Fourier transformation then simply yields a spectrum $E'(\nu)$. In practise, a Lorentizian is used for the intrinsic lineshape $E_0(\nu)$, and a Bessel function for apodization ($D_g(x)$).

2.2.5 Isotopic substitution

The frequency of a vibrational mode depends on the masses of the atoms as well as on the geometry of the molecule and the force constants. If the mass of one type of atom can be changed by substituting a different isotope from the normally predominant one and the other factors which determine the frequencies of the modes remain constant, then certain simple predictions can be made about the changes in frequency which will be observed. Clearly, if the type of atom for which the substitution is made does not move in a particular mode, the frequency of that mode will be unchanged, whereas if the mode involves predominantly the movement of this type of atom the change of frequency may be quite large. Isotope substitution may thus be a useful aid in making vibrational assignments. Consider, for instance, the totally symmetric 'breathing mode' of the methane molecule, in which all four hydrogen atoms move radially in and out in phase with each other. In the

simplest model the frequency of this mode can be calculated using equation (2.15), and is given by

$$v = \frac{1}{2\pi} \sqrt{\frac{k}{m_H}} \qquad (2.22)$$

where m_H is the mass of the hydrogen atom and k is the force constant for C-H stretching, since in this mode the carbon atom does not move and the vibration has the same frequency as that of a diatomic molecule consisting of a hydrogen atom bonded to an atom of infinite mass by a bond with force constant k. Since the frequency of this mode is independent of the mass of the carbon atom, it would not change if the mass of the carbon atom were changed from the usual 12 to 13 amu (atomic mass unit) by isotopic substitution, whereas if the masses of all the hydrogen atoms were changed from 1 to 2 amu by the substitution of deuterium the frequency would, in the harmonic approximation, be reduced by a factor $\sqrt{2}=1.414$.

The effect of isotope substitution on the frequency of any particular normal mode could only be predicted accurately if the precise molecular geometry and force constants were known, and only approximate shifts can be calculated. There is a simple approximate rule derived by Krimm [80] which seems to apply quite well to the case of hydrogen-deuterium substitution. If v is the frequency of a vibration of the molecule before isotopic substitution, and v' is the frequency of the same vibration after isotopic substitution, the ratio of these two frequencies is

$$\frac{v'}{v} = \sqrt{1 - \frac{\Delta T}{\rho T}} \qquad (2.23)$$

where T is the total kinetic energy associated with the vibration and ΔT is the change in kinetic energy which results from isotopic substitution. ρ is the ratio of the isotopic to the normal mass (ρ=2 in the present case).

For an example of the possibility given by isotopic substitution in the study of polymer crystals, see page 166 of reference [81].

2.3. Thermal analysis

2.3.1 Theoretical

Introduction

When a polymeric solution is cooled down, a liquid-solid transition can be observed corresponding to the formation of organized phases. The knowledge of the temperature/concentration phase diagram brings significant information on the types of phase involved (polymer/solvent compound, congruent melting, etc.) and on the mechanisms involved during the formation of these phases.

For the systems to be in equilibrium, there are a few rules which allow the phase diagram to be built. However, these rules also apply when the systems are formed out of equilibrium and to thermoreversible gels as long as the cooling rate and the quench temperature are identical for all the concentrations.

2.3.1.1 Variance

Phase diagrams obey the Gibbs phase rule. This rule gives the degree of freedom of the system, its variance υ_G, and particulary the maximum number of coexisting phases for a given number of components. The variance υ_G of a system may be regarded as the dimension in the T, x_1, x_2, ..., x_i diagram of the locus where a given transformation takes place. If Φ is the number of possible phases and c the number of components of the system, then the variance reads at constant pressure :

$$\upsilon_G = c - \Phi + 1 \qquad (2.24)$$

For a two-component system (c=2), if υ_G=2, then Φ=1 (one phase in equilibrium with itself) and this equilibrium occurs within an area of the T, x diagram. Now, if υ_G=1, one phase is in equilibrium with another one and the locus of the transition is a line (T=f(x)). Finally, for υ_G=0 three phases coexist, an event that can only appear on a zero-dimension locus, i.e. a point. Correspondingly, three phases cannot exist at different temperatures or concentrations even for non-equilibrium conditions without violating Gibbs phase rule.

2.3.1.2 Temperature-invariant transitions

For a two-component system, when three phases coexist there is a temperature invariant transition which produces a thermal event. It is possible to determine the composition of each of these three phases : x_T, the composition at which the three phases coexist, x_α, the polymer-poor phase composition and x_β, the polymer-rich phase composition. At x_T, only

one endotherm will be observed corresponding to the transition of two phases into one. If ΔH_T is the heat associated with this transition, the following relations are derived from the lever rule :

$$\text{for } x \leq x_T \qquad \Delta H_T(x) = \frac{|x - x_\alpha|}{|x_T - x_\alpha|} \times \Delta H_T \qquad (2.25)$$

$$\text{for } x \geq x_T \qquad \Delta H_T(x) = \frac{|x - x_\beta|}{|x_T - x_\beta|} \times \Delta H_T \qquad (2.26)$$

As a result, for $x \leq x_T$, $\Delta H_T(x)$ increases linearly with x up to x_T, then decreases for $x \geq x_T$. $\Delta H_T(x)=0$ for $x=x_\alpha$ and $x=x_\beta$. Such a diagram is known as Tamman's diagram. In the case of a polymer/solvent compound, the Tamman's diagram will allow the determination of the stoichiometry of the compound.

2.3.1.3 Polymer-solvent compound

The polymer-solvent compound is characterized by the following reactions at the stoichiometric composition, C_γ

Compound $\Rightarrow$ liquid   for a congruently melting compound where the compound and the liquid have the same composition (figure 2.6 a).

Compound $\Rightarrow$ liquid + solid   for an incongruently melting compound where the liquid and the solid both have compositions which differ from that of the compound (figure 2.6 b).

The intermediate case can also be found and is designated as a compound possessing a singular point (figure 2.6 c).
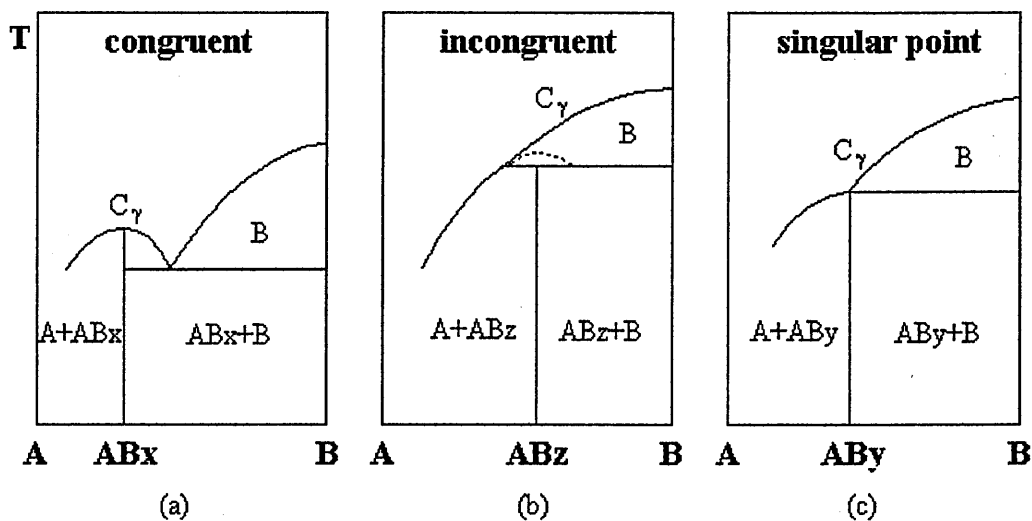
Figure 2.6.

Examples of phase diagrams involving polymer + solvent compounds. C_γ stoichiometric composition. The dotted line in 'incongruent' represents the metastable extension (from reference [19]).

2.3.2 Differential scanning calorimetry

Introduction

When a material undergoes a change of state, such as melting, heat is either absorbed or given. Many such processes can be initiated by raising the temperature of the material.

Differential Scanning Calorimetry (DSC) provides a means of measuring the enthalpies ΔH of these processes. This latter value is obtained by integrating the intensity of the DSC peaks corresponding to the different thermal events.

For a semi-crystalline polymer, a typical DSC trace will present a low temperature endotherm corresponding to the glass transition of the amorphous phase. At higher temperature, a large melting endotherm is expected corresponding to the melting of the crystalline phase. The transition between different crystalline phases, if existing, will also appear as an endotherm. Recrystallization is also possible and will lead to the presence of an exotherm.

2.3.2.1. Technique

Two pans, one containing the sample, the other empty used as a reference are placed on two positions equipped with sensors (figure 2.7).

A temperature scanning consists of heating or cooling the sample at a given rate (°C/min). The temperature difference between the sample and the reference is constantly monitored and sent to a control module. The heating power of the reference is adjusted so as to reduce the temperature difference with the sample. In case a thermal event occurs during the temperature scanning, i.e. an endothermic or an exothermic transformation, this will require more or less heat to be sent to the reference. A DSC measurement will consist of plotting the rate of heat applied to the reference against the temperature. Endotherms or exotherms will then appear as peaks.

Platinum sensors

Heaters
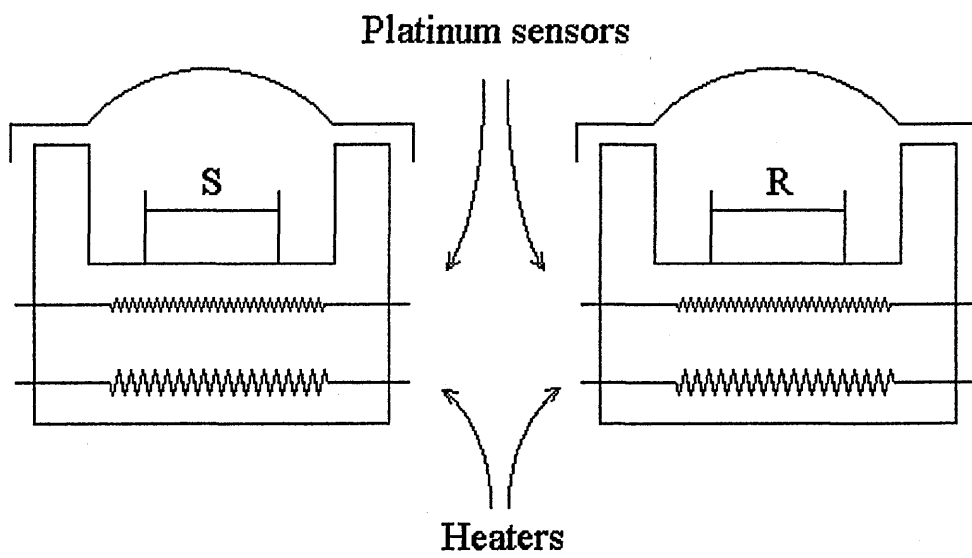
Figure 2.7.

Block diagram of the differential scanning calorimeter.

Chapter 3

Neutron Scattering Technique

3.1. Theoretical basis of scattering

Introduction

Neutron scattering in the study of polymers presents several advantages in comparison to other scattering techniques such as light and X-ray scattering. Incident beams of long wavelength can be used ($\lambda \sim$ 1-2 nm). This allows us to access small momentum transfer ranges which are otherwise difficult to reach with the other techniques. These values of the momentum transfer q are within the range of the characteristic lengths of macromolecules. Typically q varies from 2.10^{-2} to 3 nm^{-1}. The use of a labelling technique allows one to 'highlight' chosen molecules in the sample in order to study their individual conformation. Finally, when polymer/solvent compounds are studied, up to four structure factors are available depending on which component, either the polymer or the solvent, is labelled.

In this chapter, we only give a general background on the neutron scattering technique. Detailed descriptions can be found elsewhere [1, 82, 83].

3.1.1. Definition of the differential cross-section and the scattering length

We consider a scattering experiment schematically shown in figure 3.1. The incident beam of neutrons is characterized by a wave vector k_0. A uniform flux Φ falls on the sample of transmission T. Some neutrons will be scattered with a wavevector k_1 parallel to the scattering direction. The sample has N identical atoms in the beam, and the detector subtends a solid angle $\Delta\Omega$ and has efficiency η.
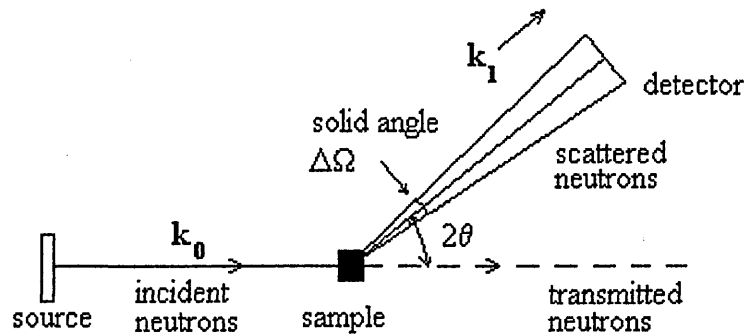
Figure 3.1.

Schematic diagram of a neutron scattering experiment.

The momentum transfer vector q is defined by

$$q = k_1 - k_0 \tag{3.1}$$

We consider scattering events where the neutron does not exchange energy with the sample, so its wavelength λ is not altered and $k_0=k_1=2\pi/\lambda$. The magnitude of $\mathbf{q}$ is then

$$q = \frac{4\pi}{\lambda}\sin\theta \tag{3.2}$$

where 2θ is the scattering angle.

The measured intensity $I(q)$ is proportional to Φ, $\Delta\Omega$, η, T and N. The constant of proportionality is called the differential cross section and is defined by :

$$\frac{d\sigma}{d\Omega} = \frac{I(q)}{\Phi NT(\Delta\Omega)\eta} \tag{3.3}$$

The quantity $\Phi NT(\Delta\Omega)\dfrac{d\sigma}{d\Omega}$ corresponds to the total number of neutrons scattered per second into $\Delta\Omega$, regardless of their energies. In the case where atoms in the sample are both noninteracting and identical, the differential cross section is just a constant

$$\frac{d\sigma}{d\Omega} = b^2 \tag{3.4}$$

The quantity b is the scattering length and is a property only of the nucleus of the scattering atom. If we come back to the definition of the differential cross section, b^2 is the probability of an incoming neutron being scattered into one steradian per unit flux of neutrons. b arises from the potential describing the interaction between the neutron and the nucleus, the Fermi pseudopotential. This interaction is a short range interaction (10^{-14} m), and can be written as the product of a delta function and a constant which is the scattering length.

3.1.2. Scattering by a system of N nuclei

The differential cross section for an assembly of N scattering units, of which the average scattering length is $\bar{b}$, can be written [82]

$$\frac{\partial\sigma}{\partial\Omega} = N\overline{\Delta b^2} + \bar{b}^2 \sum_{j=1}^{N}\sum_{k=1}^{N} \left\langle \exp[i\mathbf{q}\cdot(\mathbf{r_k}-\mathbf{r_j})]\right\rangle \qquad (3.5)$$

where

$$\overline{\Delta b^2} = \overline{b^2} - \bar{b}^2 \qquad (3.6)$$

$\overline{b^2}$ is the averages of the square of the scattering lengths made over the N scattering units. The first term in equation 3.5 is the incoherent scattering which depends only on the fluctuations of the length b, therefore no information can be obtained about the relative positions of the scattering units in the sample. The second term is the coherent scattering which contains information about the relative positions of the scattering units in the sample. This term can be written

$$\left.\frac{\partial\sigma}{\partial\Omega}\right)_{coh} = \bar{b}^2 \sum_{i=1}^{N}\sum_{j=1}^{N} \left\langle \exp[-i\mathbf{q}\cdot(\mathbf{r_i}-\mathbf{r_j})]\right\rangle \qquad (3.7)$$

3.1.3. Scattering by a mixture of two different nuclei

Let us consider a two species mixture with N_1 molecules of scattering length b_1 and N_2 of scattering length b_2 [83]

$$\left.\frac{\partial\sigma}{\partial\Omega}\right)_{coh} = b_1^2 S_{11}(\mathbf{q}) + 2b_1 b_2 S_{12}(\mathbf{q}) + b_2^2 S_{22}(\mathbf{q}) \qquad (3.8)$$

where

$$S_{kl}(\mathbf{q}) = \sum_{i=1}^{N_k}\sum_{j=1}^{N_l}\left\langle \exp[-i\mathbf{q}\cdot(\mathbf{r}_i - \mathbf{r}_j)]\right\rangle \qquad (3.9)$$

Here k,l=1 or 2. If we assume that any density fluctuations are negligible, then the system is incompressible and

$$S_{11}(\mathbf{q}) + S_{21}(\mathbf{q}) = 0 \qquad (3.10a)$$

$$S_{12}(\mathbf{q}) + S_{22}(\mathbf{q}) = 0 \qquad (3.10b)$$

Equation 3.8 becomes

$$\left.\frac{\partial\sigma}{\partial\Omega}\right)_{coh}(b_1 - b_2)^2 S_{11}(\mathbf{q}) = (b_1 - b_2)^2 S_{22}(\mathbf{q}) = -(b_1 - b_2)^2 S_{12}(\mathbf{q}) \qquad (3.11)$$

3.1.4. Generalisation to a mixture of p+1 species

These results can be generalized to a system consisting of p+1 different species i ($0 \le i \le p$) of molar volume V_i [82]

$$\left.\frac{\partial\sigma}{\partial\Omega}\right)_{coh} = \sum_{i=1}^{p}(b_i - \frac{V_i}{V_0}b_0)^2 S_{ii}(\mathbf{q}) + 2\sum_{i<j}(b_i - \frac{V_i}{V_0}b_0)(b_j - \frac{V_j}{V_0}b_0)S_{ij}(\mathbf{q}) \qquad (3.12)$$

and the hypothesis on incompressibility

$$\sum_{i=0}^{p} S_{ki}(\mathbf{q}) = 0 \qquad (3.13)$$

63

3.1.5. Applications

3.1.5.1. A mixture of hydrogenous polymer and its deuterium labelled counterpart

We assume that the two polymers are identical and differ only by coherent scattering length b_H and b_D and also that the volumes of the scattering units are identical. We assume also that the total number of molecules is N, $N_D=xN$ of them being deuterated and $N_H=(1-x)N$ being protonated and z is the degree of polymerization. We can write

$$\left.\frac{\partial\sigma}{\partial\Omega}\right)_{coh} = (b_D - b_H)^2 S_{DD}(q) = (b_D - b_H)^2 S_{HH}(q) = -(b_D - b_H)^2 S_{HD} \qquad (3.14)$$

The $S_{kk}(q)$ can be decomposed into intra- and inter-molecular interferences. We can define a scattering unit with two indices, one of which is characteristic of the chain and ranges from 1 to N_k (p and q), and the second is characteristic of the position on the chain and goes from 1 to z_k (j and l)

$$S_{kk}(q) = \sum_{p=1}^{N_k} \sum_{q=1}^{N_k} \sum_{j=1}^{z_k} \sum_{l=1}^{z_k} \left\langle \exp[-iq \cdot (r_{p,j} - r_{q,l})] \right\rangle \qquad (3.15)$$

We extract the terms corresponding to the same molecules (p=q) and the terms corresponding to two different molecules (p≠q).

$$S_{kk}(q) = N_k \sum_{j_1=1}^{z_k} \sum_{l_1=1}^{z_k} \left\langle \exp[-iq \cdot (r_{j_1} - r_{l_1})] \right\rangle + N_k^2 \sum_{j_1=1}^{z_k} \sum_{l_2=1}^{z_k} \left\langle \exp[-iq \cdot (r_{j_1} - r_{l_2})] \right\rangle \qquad (3.16)$$

or

$$S_{kk}(q) = N_k z_k^2 P_k(q) + N_k^2 z_k^2 Q_{kk}(q) \qquad (3.17)$$

and similarly, we can define

$$S_{nk}(q) = N_n N_k z_n z_k Q_{nk}(q) \qquad (3.18)$$

where

$$P_k(q) = \frac{1}{z^2} \sum_{j_1=1}^{z_k} \sum_{l_1=1}^{z_k} \left\langle \exp[-i\mathbf{q} \cdot (\mathbf{r}_{j_1} - \mathbf{r}_{l_1})] \right\rangle \qquad (3.19)$$

$$Q_{nk}(q) = \frac{1}{z^2} \sum_{j_1}^{z_n} \sum_{l_2}^{z_k} \left\langle \exp[-i\mathbf{q} \cdot (\mathbf{r}_{j_1} - \mathbf{r}_{l_2})] \right\rangle \qquad (3.20)$$

$P_k(q)$ and $Q_{nk}(q)$ are normalized so as to go to unity at q=0. Remembering that $z_D = z_H = z$ and

thus $P_D = P_H = P$ and $Q_{DD} = Q_{HD} = Q$, we can express S_{DD}, S_{HH} and S_{HD} in terms of P(q) and

Q(q) to obtain

$$xNz^2P(q) + x^2N^2z^2Q(q) = (1-x)Nz^2P(q) + (1-x)^2N^2z^2Q(q)$$
$$= -x(1-x)N^2z^2Q(q) \qquad (3.21)$$

Using these equalities it can be shown that

$$Nz^2P(q) + N^2z^2Q(q) = 0 \qquad (3.22)$$

or

$$NQ(q) = -P(q) \qquad (3.23)$$

Using this value of Q(q) in any of the three relationships gives

$$\left. \frac{\partial \sigma}{\partial \Omega} \right)_{coh} (q) = (b_D - b_H)^2 x(1-x)Nz^2P(q) \qquad (3.24)$$

3.1.5.2. A mixture of deuterated and hydrogenous polymer in a solvent

We assume that the molar volumes of the protonated and deuterated polymers are equal

($v_D = v_H = v$), and we dissolve them in a solvent of molar volume v_S and scattering length b_S

$$\frac{\partial \sigma}{\partial \Omega} = (b_D - \frac{v}{v_S} b_S)^2 S_{DD} + (b_H - \frac{v}{v_S} b_S)^2 S_{HH} + 2(b_D - \frac{v}{v_S} b_S)(b_H - \frac{v}{v_S} b_S) S_{HD}$$

$$(3.25)$$

Since both polymers are characterized by the same P(q) and Q(q) values

$$S_{DD} = xNz^2 P(q) + x^2 N^2 z^2 Q(q) \qquad (3.26)$$

$$S_{HH} = (1-x)Nz^2 P(q) + (1-x)^2 N^2 z^2 Q(q) \qquad (3.27)$$

$$S_{HD} = -x(1-x)N^2 z^2 Q(q) \qquad (3.28)$$

Finally [83]

$$\frac{\partial \sigma}{\partial \Omega}\bigg)_{coh} = (b_D - b_H)^2 x(1-x)Nz^2 P(q) + (xb_D + (1-x)b_H - \frac{v}{v_S} b_S)^2 [Nz^2 P(q) + N^2 z^2 Q(q)]$$

$$(3.29)$$

If one adjusts the average scattering length b_S of the solvent by using instead of a pure liquid, a mixture with a concentration y of deuterated solvent (scattering length $b_D{}^S$) and (1 - y) of ordinary solvent (scattering length $b_H{}^S$), such that $b_S = b_D{}^S y + b_H{}^S(1-y)$, then one can achieve the condition

$$xb_D + (1-x)b_H - \frac{v}{v_S} b_S = 0 \qquad (3.30)$$

The average polymer-solvent contrast and hence the corresponding scattering becomes zero.

3.2. Neutron scattering ranges

Neutron scattering ranges can be classified into four categories as follows

a) Small angle (SANS) $q < 0.1 \text{Å}^{-1}$

b) Intermediate angle (IANS) $0.1 \text{ Å}^{-1} < q < 0.4 \text{Å}^{-1}$

c) Wide-angle (WANS) $0.4 \text{ Å}^{-1} < q$

d) Crystallographic range

3.2.1. The behaviour at small q

Let us come back to the definition of the form factor

$$P(q) = \frac{1}{z^2} \sum_{i=1}^{z} \sum_{j=1}^{z} \langle \exp[-i\mathbf{q} \cdot \mathbf{r}_{ij}] \rangle \tag{3.31}$$

where $\mathbf{r}_{ij}$ is the vector joining two scattering points of the same molecule. The $\langle \ \rangle$ indicate that an average value has to be taken over the sum or over each term of the sum. If we average over the orientation, we find the relation first derived by Debye

$$P(q) = \frac{1}{z^2} \sum_{i=1}^{z} \sum_{j=1}^{z} \left\langle \frac{\sin q r_{ij}}{q r_{ij}} \right\rangle \tag{3.32}$$

where the average has to be taken over the r_{ij} distances only. For small q, we can expand P(q) in powers of q [82]

$$P(q) = 1 - \frac{q^2}{6z^2} \sum_{i=1}^{z} \sum_{j=1}^{z} \langle r_{ij}^2 \rangle + \frac{q^4}{5!z^2} \sum_{i=1}^{z} \sum_{j=1}^{z} \langle r_{ij}^4 \rangle - \dots \tag{3.33}$$

The second term of this expansion has a geometrical meaning : the radius of gyration. The radius of gyration of a particle made of z identical elements is given by

$$\overline{R_G^2} = \frac{1}{z}\sum_{i=1}^{z}\left\langle r_i^2 \right\rangle = \frac{1}{2z^2}\sum_{i=1}^{z}\sum_{j=1}^{z}\left\langle r_{ij}^2 \right\rangle \qquad (3.34)$$

where r_i is the vector joining the scattering point i to the centre of gravity of the molecule. Equation 3.33 can be rewritten

$$P(q) \approx 1 - \frac{q^2}{3}\overline{R_G^2} \qquad (3.35)$$

In addition, if the absolute intensity has been calculated, the molecular weight can be obtained at the limit q=0 (see 3.3.2).

3.2.2. Neutron crystallography

As with wide angle X-ray scattering, neutron scattering gives information about the crystalline structure of the sample under study. The theoretical derivations given in the WAXS chapter are also valid when using neutrons of wavelengh similar to crystallographic distances, provided that the atomic scattering factor f is replaced by the scattering length. The unit cell structure factor pertaining to the reflection (hkl) is

$$F(hkl) = \sum_{j=1}^{N} b_j \exp[2\pi i(hx_j + ky_j + lz_j)]\exp[-B_j(\sin^2\theta)/\lambda^2] \qquad (3.36)$$

λ is the neutron wavelength and B_j is the thermal parameter of the jth atom. The second exponential factor accounts for the falloff in scattering intensity power of the jth atom due to thermal motion. As can be seen, when one is dealing with a polymer solvent complex, no

68

less than four structure factors are available, depending on which combination of species (deuterated or protonated) are used for the solvent and the polymer.

The resulting intensity is

$$I(hkl) = N_{cells}F(hkl)F*(hkl) \qquad (3.37)$$

where N_{cells} is the number of unit cells present in the sample. Finally, in the case where the thermal parameters for all the atoms are equal ($B_j = B_0$) [11]

$$I(hkl) = N_{cells}^2 \exp[-2B_0(\sin^2\theta)/\lambda^2] \sum_{m=1}^{N}\sum_{n=1}^{N} b_m b_n \cos 2\pi[(x_m - x_n)h + (y_m - y_n)k + (z_m - z_n)l]$$

$$(3.38)$$

3.3. Data processing

3.3.1. Subtractions of the empty cell and incoherent intensity

For isotopic labelling of molecules, a measurement of I(q) requires the recording of count rate versus angle for

a) the isotope mixture

b) equivalent polymer sample of one (or both) pure isotopes

c) the empty specimen container

d) the container with a neutron-absorbing piece of cadmium in place of the specimen

e) an isotropic scatterer (usually H_2O)

f) the container for e)

The methods of algebraic manipulation in order to extract I(q) are described elsewhere. The parasitic intensities from the diffractometer (c and d) must be subtracted, with due allowance for that intensity contribution which is attenuated when the sample is in place. These two first steps of the data analysis were carried out using the software available at the neutron scattering facilities we visited.

All the equations derived in the previous section assume that the incoherent scattering has been subtracted. For a dilute mixture of a deuterated polymer in a hydrogenous matrix, the incoherent scattering is due almost entirely to that from the hydrogenous matrix. In this case the scattering from a 100% hydrogenous sample (b) can be subtracted with virtually no error because of the very small amount of incoherent scattering from the deuterium.

3.3.2. Normalisation of the intensity

The measured scattered intensity I(q) after subtraction of the incoherent scattering is related to the coherent differential cross section per monomer $d\sigma/d\Omega$ via equation 3.3

$$I(\mathbf{q}) = \Phi N_D \Delta\Omega \eta T \frac{d\sigma}{d\Omega}\bigg)_{coh} \qquad (3.39)$$

In order to be able to correct for detector efficiency, it is necessary to use a substance that scatters entirely incoherently in the q range of the experiment. The scattering from a standard incoherent scatterer can be written as

$$I_s(\mathbf{q}) = \Phi N_s \Delta\Omega \eta T_s \frac{\sigma_s}{4\pi} \qquad (3.40)$$

70

N_s is the total number of scattering atoms (or monomers) of cross section σ_s. The ratio of the two intensities gives the coherent cross section for the deuterated monomer

$$\left.\frac{\partial\sigma}{\partial\Omega}\right)_{coh}(q)=\frac{\sigma_s}{4\pi}\frac{N_s}{N_D}\frac{T_s}{T}\frac{I(q)}{I_s(q)}\qquad(3.41)$$

which can be related to equation 3.24, assuming $x\cong1$.

$$\left.\frac{\partial\sigma}{\partial\Omega}\right)_{coh}(q)=(b_D-b_H)^2(1-x)N_Dz^2P(q)\qquad(3.42)$$

The normalized intensity is $zP(q)$ [1]

$$zP(q)=\frac{1}{N_Dz}\frac{1}{(1-x)(b_D-b_H)^2}\frac{N_s}{N_Dz}\frac{\sigma_s}{4\pi}\frac{T_s}{T}\frac{I(q)}{I_s(q)}\qquad(3.43)$$

where

$$N_Dz=xN_A\frac{m}{M_D}\qquad\text{and}\qquad N_s=\frac{m_s}{M_s}N_A\qquad(3.44)$$

m and m_S are the masses of the sample and the standard. N_A is Avogadro's number and M_D and M_H the molar masses of the deuterated and standard monomers.

3.3.3 Zimm plot and Kratky plot

By combining equations (3.35) and (3.43), the behaviour of the normalized intensity at small q is given by

$$\frac{1}{I}(q)\propto\frac{1}{M_W}(1+q^2\frac{R_g^2}{3})\qquad(3.45)$$

71

For small angles, the plot of the inverse of the intensity against the square of the momentum transfer should be linear. Such a plot is called a Zimm plot. The molecular weight is then given by the intercept at q=0 and the slope yields the radius of gyration. Another type of representation, which will use, is that consisting of plotting the intensity times the square of the momentum transfer $(I(q)q^2)$ against q. This type of representation is called a Kratky plot. It was initially introduced in order to highlight the expected behaviour of the intensity for a gaussian chain at large angles, for which $1 / I(q) \propto q^2$.

3.4. Instruments

Neutron scattering experiments were carried out in two different facilities. SANS measurements were made using the LOQ instrument at the ISIS neutron source (Rutherford-Appleton Laboratory, Chilton, England). IANS experiments were performed at the Institut Laue-Langevin (ILL, Grenoble, France), with the D17 instrument.

ILL uses a reactor neutron source, while ISIS uses a pulsed neutron spallation source. In the reactor core, neutrons are released by the fission of enriched ^{235}U. Each fission event produces 2 to 3 neutrons, though one of these is needed to sustain the chain reaction. The other approach to neutron production is that used in spallation neutron sources. These use particle accelerators and synchrotrons to generate intense, high-energy, proton beams which are directed at a target composed of heavy nuclei. Provided that the protons have

sufficient kinetic energy they are able to blast the target nuclei apart. The word spallation is a quarrying term for "chipping away".

Neutrons are counted by detecting the product of their reaction with certain nuclei, in particular ^{10}B, ^{3}He or ^{6}Li. The products of these reactions can then be detected either by ionization of a gas, or by light emission (in scintillation detectors). D17 and LOQ are both equipped with gas detectors (BF$_3$ and ^{3}He-CF$_4$ respectively). At the time we carried out the second set of SANS measurements (June 1996), the first module of the LOQ high-angle bank (HAB) was installed. With this new scintillator detector, neutrons of momentum transfer of up to approximately 1.4Å^{-1} can be detected.

With a steady-state source, it is usual to vary q by effectively scanning θ at a pre-selected value of λ. On pulsed sources, a "fixed instrument geometry" (effectively a constant θ mode) is employed and a range of q values are obtained by time-sorting different λ's from the polychromatic incident beam as they arrive at the detector. The selection of λ is done for the D17 instrument using a velocity selector. This device involves rotating a cylinder with a set of helical grooves cut into its outer surface. The cylinder spins on its axis, and neutrons are transmitted with a mean wavelength depending on the pitch of the helix and its speed of rotation, and a wavelength spread depending on its length and slot width. At ILL, the velocity selector we used provided a spectrum characterized by a Gaussian distribution centered at λ=8.5Å, and a relative width at half-height Δλ/λ=10%. The sample-detector distances were 83 cm for D17, and 405 cm and 50 cm respectively for the main and for the HAB detectors at LOQ. Table 3.1 compares the characteristics and

performances of D17 and LOQ. Figures 3.2 and 3.3 show the experimental settings of the

LOQ and D17 intruments at ISIS and ILL respectively.

Instrument	LOQ (HAB)	D17
Source	Spallation	Reactor
Incident Wavelength (Å)	2.2-10.0 (25Hz)	8.5
Flux at sample ($n\,cm^{-2}\,s^{-1}$)	2×10^5	10^6
q_{min} ($Å^{-1}$)	0.008 (0.15)	0.8
q_{max} ($Å^{-1}$)	0.24 (1.4)	25
Detector type	^{3}He (^{6}Li)	BF_3
Sensitive area of the detector (cm^2)	64×64 (1500)	64×64
Pixel size (mm^2)	5.3×5.3 (6.0×6.0)	5×5
Sample/detector distance (m)	4.05 (0.50)	available : 0.80 to 3.5 used : 0.83

Table 3.1.

Characteristics and performances of D17 and LOQ instruments.
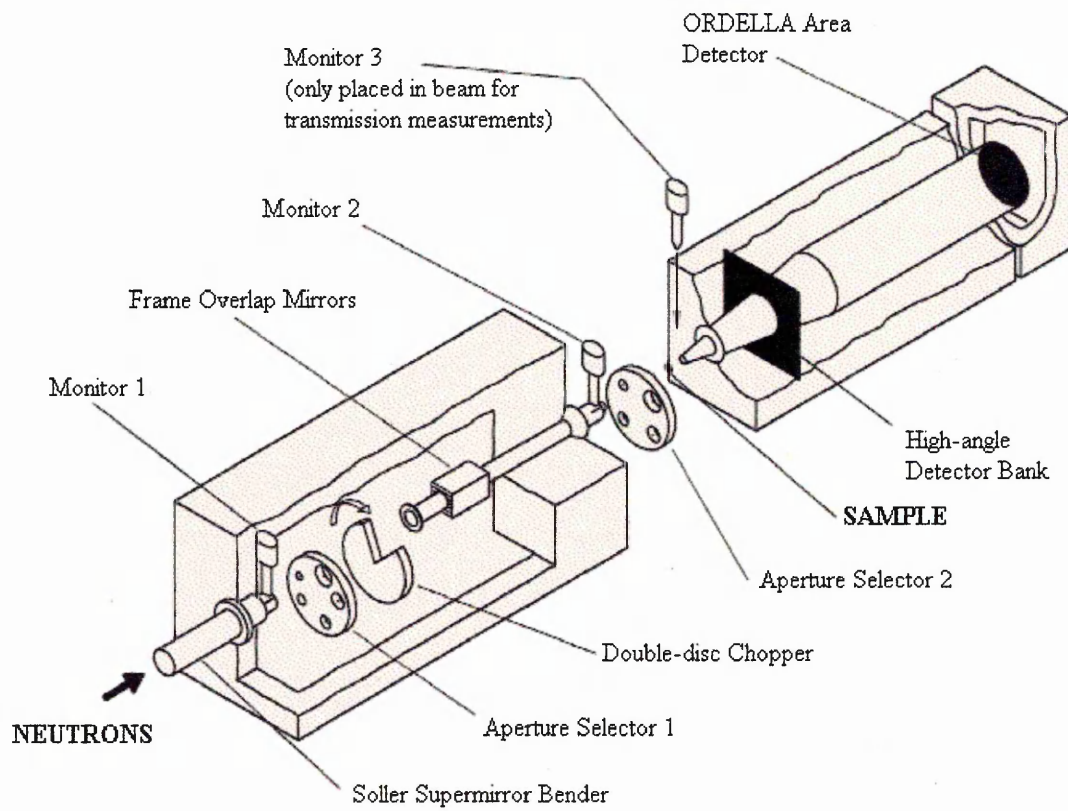
Figure 3.2.

Schematic diagram of the LOQ instrument at ISIS.

cold beam H17

velocity selector

neutron guide

main monitor

attenuator and alignment system

collimator or polariser

chopper

sample changer

multidetector
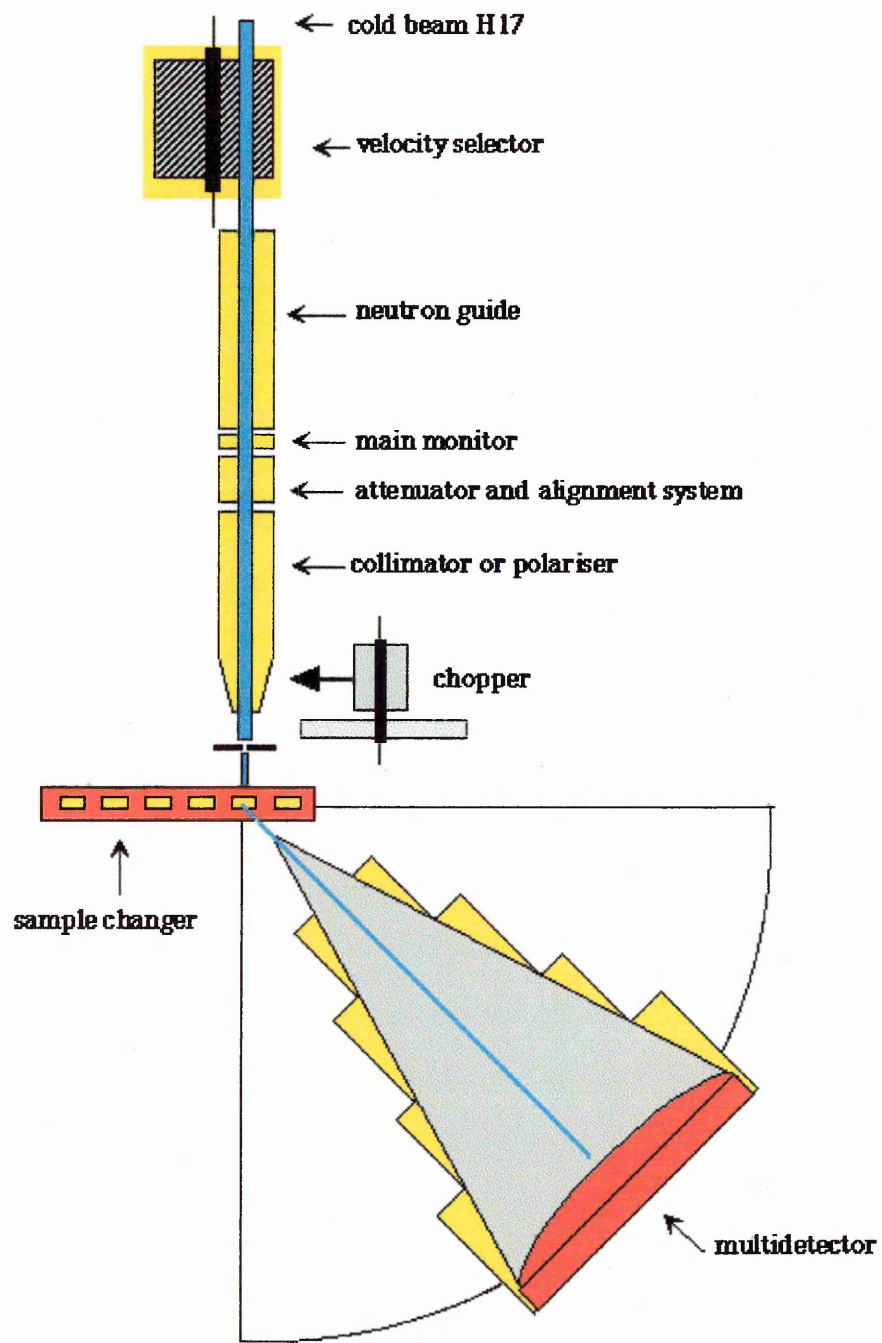
Figure 3.3.

Schematic diagram of the D17 instrument at ILL.

3.5 The statistical model and the calculation of the scattered intensity from this model

Introduction

We have already described the various attempts made to model the sheetlike arrangements of stems in polymer crystals in chapter 1. The statistical model created by Sonntag et al. [17] features two free parameters and is used numerically to generate a population of crystal stems corresponding to a molecule. As with the previous models, it is used to describe a sheetlike structure. A pair correlation function of the stems can thus be obtained and the resulting scattered intensity can be calculated. The original program was written in C++ by P. Sonntag for the purpose of calculating the neutron scattering intensity of PE. We adapted it for sPS and added a routine for the calculation of the radius of gyration.

3.5.1. The model

In the model, the sheet within the lamellar crystal is considered to be a one-dimensional sequence of stems, each of which may be either labelled or unlabelled. A crystal sheet is assumed to contain σ labelled stems and is generated by the following procedure (figure 3.4):

1. An initial labelled stem is placed down.

2. Subsequent labelled stems are placed down with probability P_A, the probability of adjacency, if the previous stem was a labelled stem or probability P_U, if the previous stem was unlabelled.

3. Step 2 is repeated until σ labelled stems have been placed.

The model thus only depends on the nearest neighbours and is called a first order Markov chain.
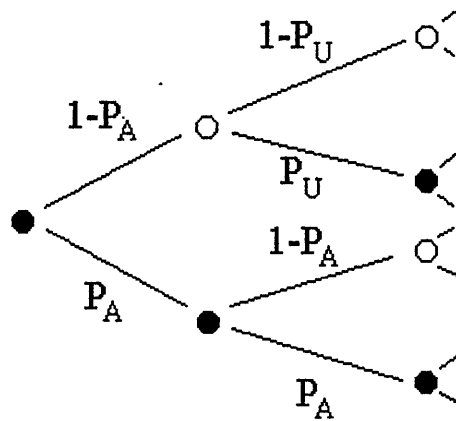
Figure 3.4.

Schematic diagram showing how stems are deposited into a sheet using the probabilities P_A and P_U.

When superfolding is introduced, the number of stems per sheet is fixed. When this number is reached, a new sheet is filled in the same manner. The initial stem of this new sheet is adjacent to the last stem of the previous sheet.

The key innovation of this model is the introduction of the probability P_U. The model has the following advantages: (a) it is adaptable to a wide variation in the probability of

adjacency and in the degree of superfolding; (b) it yields simple analytical results for key model characteristics (see below) and (c) the analytical results provide tests for the sampling statistics of the computer simulations used to generate 'molecules'.

We give hereafter some important analytical results. The total number of lattice sites in the region occupied by the labelled molecule, called the mean length $< L >$ in reference 8, is defined as follows, where $<\sigma'>$ is the average number of unlabelled stems

$$< L >= \sigma + < \sigma' >= \sigma + (\sigma - 1)\left(\frac{1 - P_A}{P_U}\right) \tag{3.46}$$

From this the dilution $\Phi = \sigma/(\sigma + <\sigma'>)$ can be calculated

$$\Phi = \frac{1}{1 + \left(1 - \frac{1}{\sigma}\right)\left(\frac{1 - P_A}{P_U}\right)} \tag{3.47}$$

The average number of clusters of size t per sheet $< n_\sigma(t)>$ is given by

$$< n_\sigma(t) >= (P_A^{t-1})\left[Q_A^2(\sigma - t - 1) + 2Q_A)(1 - \delta_{t\sigma}) + \delta_{t\sigma}\right] \tag{3.48}$$

where $Q_A = 1 - P_A$, $Q_U = 1 - P_U$ and δ_{ij} is the Kronecker delta.

The average cluster size $<t>$, i.e. the average number of stems per cluster, is

$$\langle t \rangle = \frac{\sigma}{\sigma - P_A(\sigma - 1)} \tag{3.49}$$

The average distance $<d>$ between two consecutive stems in a sheet is

$$\langle d \rangle = d_i\left[P_A + (1 - P_A)\frac{(1 + P_U)}{P_U}\right] \tag{3.50}$$

Where d_i is the shortest interstem distance. In addition to the calculation of the intensity, we added to the original program the calculation of the radius of gyration for each

79

molecule "thrown", and finally calculated its average. This gives us an additional test for the fits between data and simulations, since results will have to satisfy both the test of the intensity and of the radius of gyration. The square of the radius of gyration of σ stems is

$$R_g^2 = \frac{1}{\sigma}\sum_{i=1}^{\sigma} R_i^2 \qquad (3.51.a)$$

where R_i is the distance of the stems from the center of gravity of the stem arrangement. If R_{ij} is the separation between stems i and j , an equivalent expression for this is

$$R_g^2 = \frac{1}{2\sigma^2}\sum_{i=1}^{\sigma}\sum_{j=1}^{\sigma} R_{ij}^2 \qquad (3.51.b)$$

3.5.2. Calculation of the scattered intensity

From the correlation function of the pair, the scattering intensity is calculated using the following expression valid for an array of σ stems [93]

$$I(q) = [nP_S(q)]\frac{1}{\sigma}\sum_{i=1}^{\sigma}\sum_{j=1}^{\sigma} J_0(qR_{ij}) \qquad (3.52)$$

where J_0 is a zeroth order Bessel function. n is the number of hydrogen nuclei per stem and $P_S(q)$ is the the form factor of a stem. This term takes into account the atomic structure of the stem. It can be calculated using Debye's equation

$$P_S(q) = \frac{1}{n^2}\sum_{i=1}^{n}\sum_{j=1}^{n} \frac{\sin qr_{ij}}{qr_{ij}} \qquad (3.53)$$

where r_{ij} is the distance between hydrogen nuclei i and j. A good approximation to this is the exponential approximation given by Sadler [4]:

$$P_S(q) = \frac{\pi}{n_{st} l_0 q} \exp(-\frac{1}{2} q^2 R^2) \qquad (3.54)$$

n_{st} is the number of monomers necessary to build up a stem, and l_0 is the length of the

monomer unit. R is the root mean square of the distance of hydrogen nuclei from the long

axis of the molecule. R can be calculated using the published model of the unit cell of sPS

and is found to equal 3.77 Å. Note that $q^2 P_S(q)$ has a maximum at $q_m = 1/R$. Let us introduce

the number of hydrogen atoms per unit length of stem, n_L :

$$n_L = \frac{n}{n_{st} l_0} \qquad (3.55)$$

Hence

$$n P_S(q) = \frac{n_L \pi}{q} \exp(-\frac{1}{2} q^2 R^2) \qquad (3.56)$$

We present in figure 3.5 the form factors of a stem of sPS and a stem of PE. Note the good

agreement between Debye's and Sadler's formulae. In the case of PE, R=1.46 Å so that the

maximum of this curve is shifted to higher q. The crystal structure of the crystalline

polymer is used for the calculation of the correlation function. In practise, one has to

choose between several folding habits, i.e. different fold directions, before running the

simulations. The geometry and the dimensions of the two dimensional lattice are

parameters of the program. Once a molecule has been "thrown", each pair of stems is

detected and the distance between the stems of this pair is calculated and stored in an

histogram. The contribution to the intensity of this pair is also calculated and stored in an

histogram. This is done for each molecule thrown, and finally an average of the intensity is

made over all the molecules.
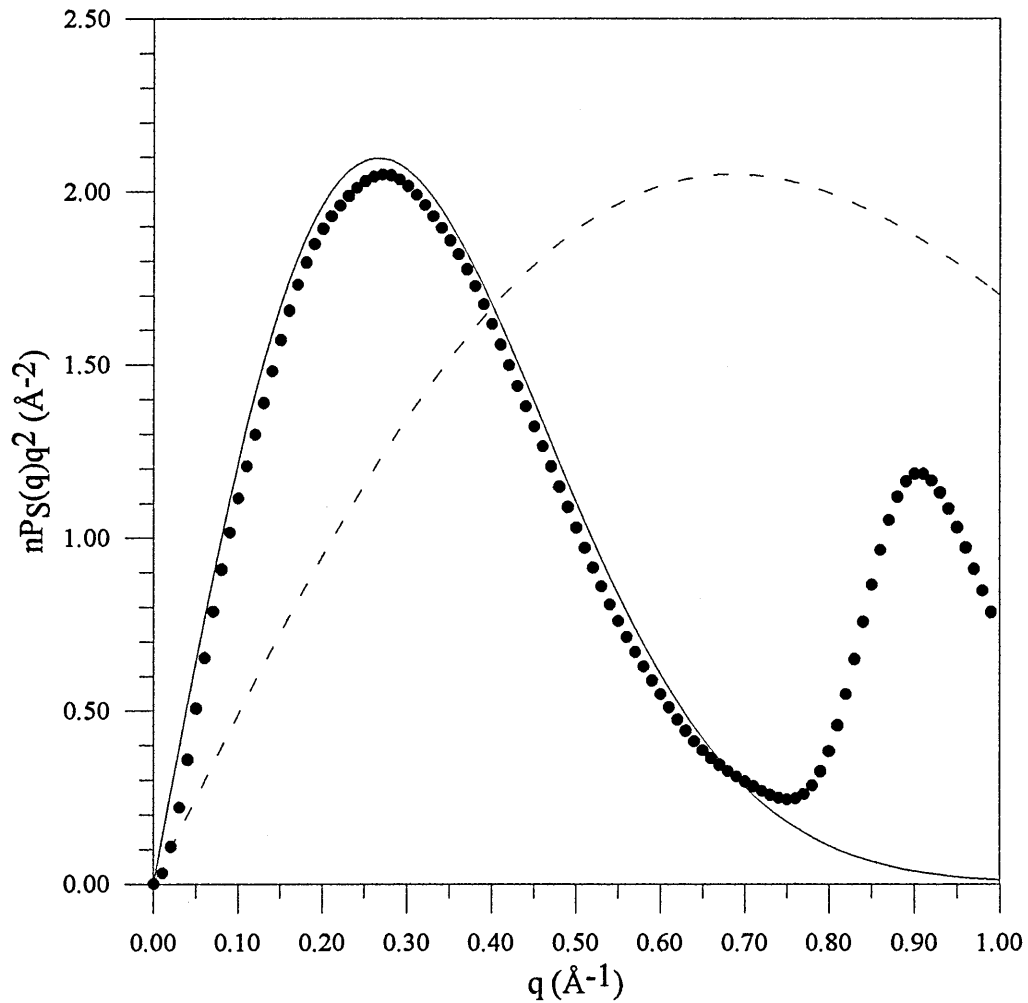
Figure 3.5.

Form factor $P_S(q)$ of a stem for sPS in the Kratky representation: (•) calculated according to Debye's equation, (—) calculated according to Sadler's approximation. In dashed line, the form factor is shown for a stem of PE.

As an example, and in order to understand how the intensity is calculated, we plotted in figure 3.6 the intensity calculated using equations 3.52 and 3.56 for a sheet of 10 adjacent stems. Two curves are presented, corresponding to two different fold directions. The ripples are due to the finite dimensions of the sheet, the periodicity of the ripples varying with this dimension which is determined here by the stem separation. When statistical parameters are used and an average of the intensity for a large number of molecules is calculated, the size of the sheet is allowed to vary and therefore the ripples disappear.

At high q a peak is present. The position q' of this peak corresponds in real space to the distance d_l between two adjacent stems, so that $q'=2\pi/d_l$. As can be seen, for PE this distance is too small to be seen in the q range presented. On the other hand, the length of the sheet is smaller in comparison to sPS, so that the periodicity of the ripples is longer. Due to the shape of the form factor of the sPS stem, the intensity decreases quickly and becomes zero at $q=1.0$ Å^{-1}, a quite different behaviour from that of PE.

In Sadler's work, the data were presented in terms of the scattering intensity of an array of infinitely thin, long stems. This means that only the contribution of the double sum in equation (3.52) was used and that the experimental data were divided by the exponential term of equation (3.56). We chose to keep the experimental data for direct comparison with the calculated intensity as it is written in equation (3.52). One has to remember this when comparing our results with Sadler's.
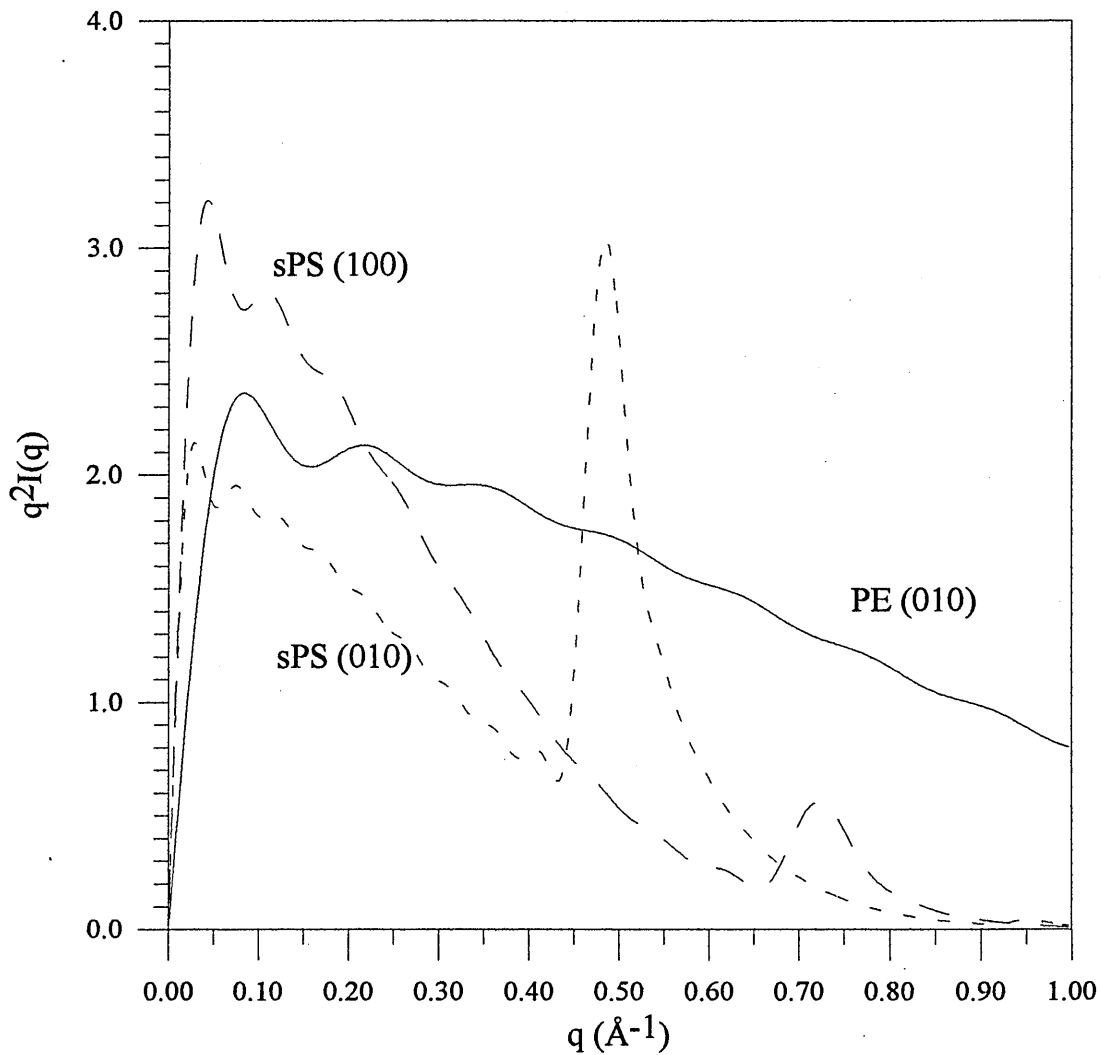
Figure 3.6.

Calculated Kratky plots for a sheet of 10 adjacent stems according to equation 3.55 and 3.59. (— —) sPS, folding along the (100) direction, (- - -) sPS, folding along the (010) direction and (——) PE, folding along the (110) direction.

Chapter 4

Results

4.1. Crystallization of sPS/ethylbenzene

Samples of sPS and fully deuterated sPS were kindly supplied by Professor V. Vittoria (Universita di Salerno) and Dr. J-M. Guenet (Université Louis Pasteur, Strasbourg). NMR measurements confirmed tacticities in excess of 99%. GPC measurements were kindly supplied by RAPRA Technology Ltd. (Shawbury, UK). Table 4.1 gives the characteristics from GPC of the samples used in this study for the different experiments. The number-average molecular weight $\overline{M}_n = \sum N_i M_i / \sum N_i$, and the weight-average molecular weight $\overline{M}_w = \sum N_i M_i^2 / \sum N_i M_i$ are given for each sample. N_i is the number of molecules of molar mass M_i. The ratio $\overline{M}_w / \overline{M}_n$ is called the polydispersity and must by definition be greater or equal to unity. This value is used as a measure of the breadth of the molar mass distribution.

Samples of polymer were dissolved by heating to form 0.1% w/w solutions in ethylbenzene. The solutions were transferred to an oil bath held at the required crystallisation temperature to within 0.5°C. Filtration at room temperature, using a stack of flat horizontal filter papers, produced a mat which was allowed to dry in air. In the later stages, the mat was sandwiched between several dry filter papers, with gentle pressure applied from a glass plate. Mats obtained in this way were shown, from WAXS data (see section 4.2.), to have a preferred c-axis orientation.

	Name	$\overline{M}_w$	$\overline{M}_n$	$\overline{M}_w / \overline{M}_n$	Use
H Material	AH	85 400	17 100	5.0	NS, X-rays, DSC
	BH	55 700	17 500	3.2	NS
	CH	43 600	18 200	2.4	DSC
D Material	AD	42 700	11 900	3.6	NS
	BD	124 500	42 400	2.9	DSC, NS
	CD	144 500	61 400	2.4	NS
	DD	124 000	45 200	2.7	NS

Table 4.1.

Characteristics of the sPS samples.

Measurements of sample weight before and after heating and removal of solvent indicated a weight loss of around 14%, corresponding to a solvent/monomer ratio of 1/6.

0.50 μm

Picture 4.1.

Transmission Electron Micrograph of sPS Crystals formed from Dilute Solution in Ethylbenzene.

TEM carried out by P. Sonntag showed a characteristic lamellar morphology obtained for crystallisation at 40°C (picture 4.1). The vacuum in the TEM sample chamber removes solvent from the crystals leading to a transition into either the γ or the empty-δ phase, but it is believed that the observed features are still characteristic of the δ-phase. The formation of lamellar stacks is typical, with widespread Moiré fringes indicative of dislocation networks. It was found to be difficult to observe individual single crystals, in part because of extensive twinning. For a crystallisation temperature (T_c) of 50°C, a change to a more fibrous morphology was observed, similar to the ribbon-like morphology reported by Wang et al. [16]. For this reason, later experiments involved only a crystallisation temperature of 40°C. To what extent the lamellar morphology is typical of polymer/solvent complexes remains uncertain.

4.2. Wide Angle X-Ray Scattering

Introduction

The crystal structure of the α- and β-phases of sPS has been extensively studied and the unit cell dimensions are well known. Although Chatani et al. [11] studied the δ-phase with a variety of solvents, there are no data in the literature for sPS/ethylbenzene crystallized at 40°C. The chain packing is expected to vary with the nature of solvent. The results presented by Wang et al [16] are relevant to a crystallisation temperature of 50°C, and the

morphology obtained was fibrous. Thus, is was necessary to determine the crystalline structure of the sPS/ethylbenzene in the δ-phase. For the γ-phase, Chatani [11] proposed a monoclinic structure identical to that of the δ-phase but with shrinkage of the b-dimension of about 2Å, although no exact unit cell dimensions were given.

The determination of the crystalline structure was made by wide angle X-ray scattering. Oriented samples such as drawn fibres are necessary for the determination of the exact crystalline structure. Although our solution grown crystals were shown to be well oriented within the mat (see section 4.3.), they are not ideal for this characterisation in comparison to uniaxially oriented fibres, as used by Chatani et al. [11]. The knowledge of the crystalline structure is relevant to the calculation of the intermediate angle neutron scattering intensity for two reasons. First the molecular stems are positioned on the crystalline lattice and the correlation function between the stems is dependent on the dimensions of this lattice. Secondly, the exact atomic structure of the stem is necessary in order to calculate its form factor, each stem being built up by stacks of several unit cells along the c direction.

4.2.1 Instrumentation

Wide Angle X-Ray Scattering were carried out on a Warhus camera with a camera length of 73 mm. Copper K_α radiation, pinhole collimation and photographic detection were used. The specimen to film distance D was calibrated using calcite powder which gives a strong reflection ring at a d-spacing of 0.3035 nm. The interplanar spacings were generally
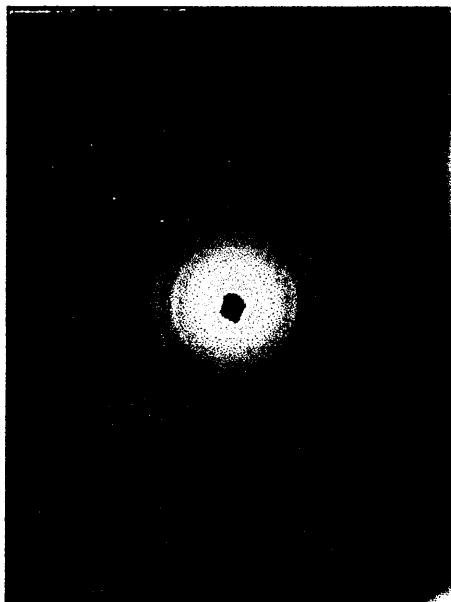
Picture 4.2.

Typical WAXS pattern for the δ-phase. The mat surface was oriented perpendicular to the X-ray beam.
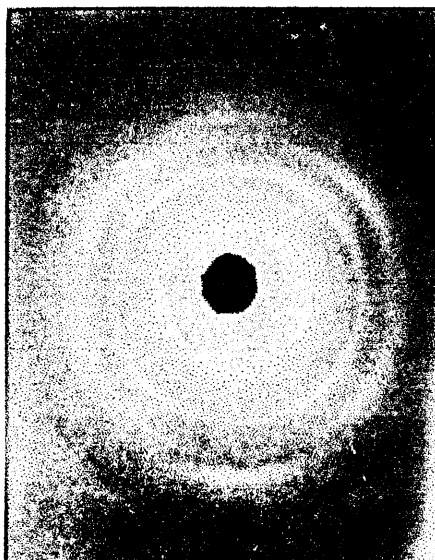
Picture 4.3.

Typical WAXS pattern for the γ-phase. The mat surface was oriented perpendicular to the X-ray beam.
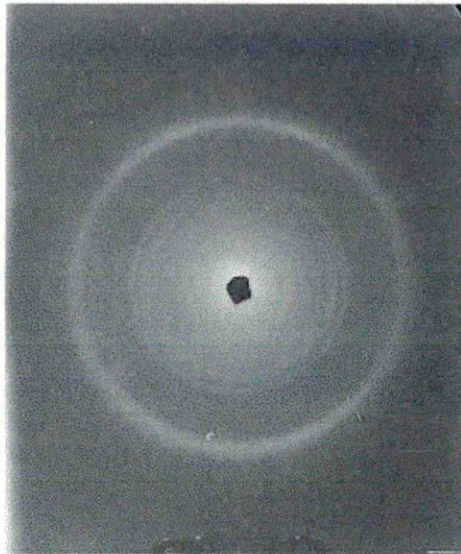
Picture 4.4.

Typical WAXS pattern for the α-phase. The mat surface was oriented perpendicular to the X-ray beam.
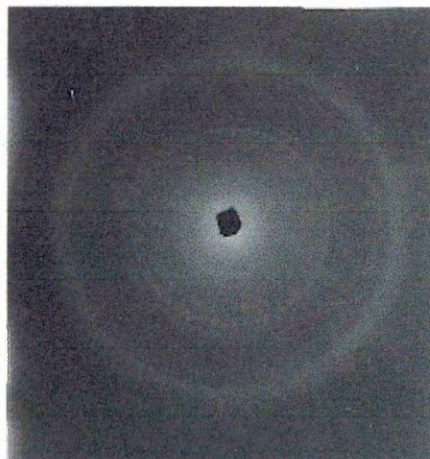
Picture 4.5.

Typical WAXS pattern for the β-phase. The mat surface was oriented perpendicular to the X-ray beam.

measured directly from the X-ray patterns using a ruler with a vernier rule. In some cases, densitometer traces were recorded using a Wooster Mark III microdensitometer from Crystal Structure Ltd.

4.2.2. The δ-, γ-, α- and β-phases

We present the typical WAXS patterns obtained for samples placed edge on, for the four phases of sPS/ethylbenzene, namely the δ-(picture 4.2), γ-(picture 4.3), α-(picture 4.4), and β-(picture 4.5) phases. The three latter phases were obtained from the former by the following heat treatments : for the γ-phase a piece of mat was heated at 135°C for 5 hours ; the α-phase was obtained by slowly heating (5°C/min) the sample to 200° ; a sudden heating at 200°C brings the sample to the β-phase. As can be seen, the initial orientation of the crystallites remains in the γ-phase, but is lost in the α- and β-phases.

4.2.2.1. The δ-phase

A densitometer trace of the δ-phase pattern was recorded along the equator. It is presented in figures 4.1. The corresponding interplanar spacings were then calculated using Bragg's law, and compared with those obtained by Wang et al. [16] and those calculated from the unit cell proposed by Chatani et al. [11] (table 4.2).
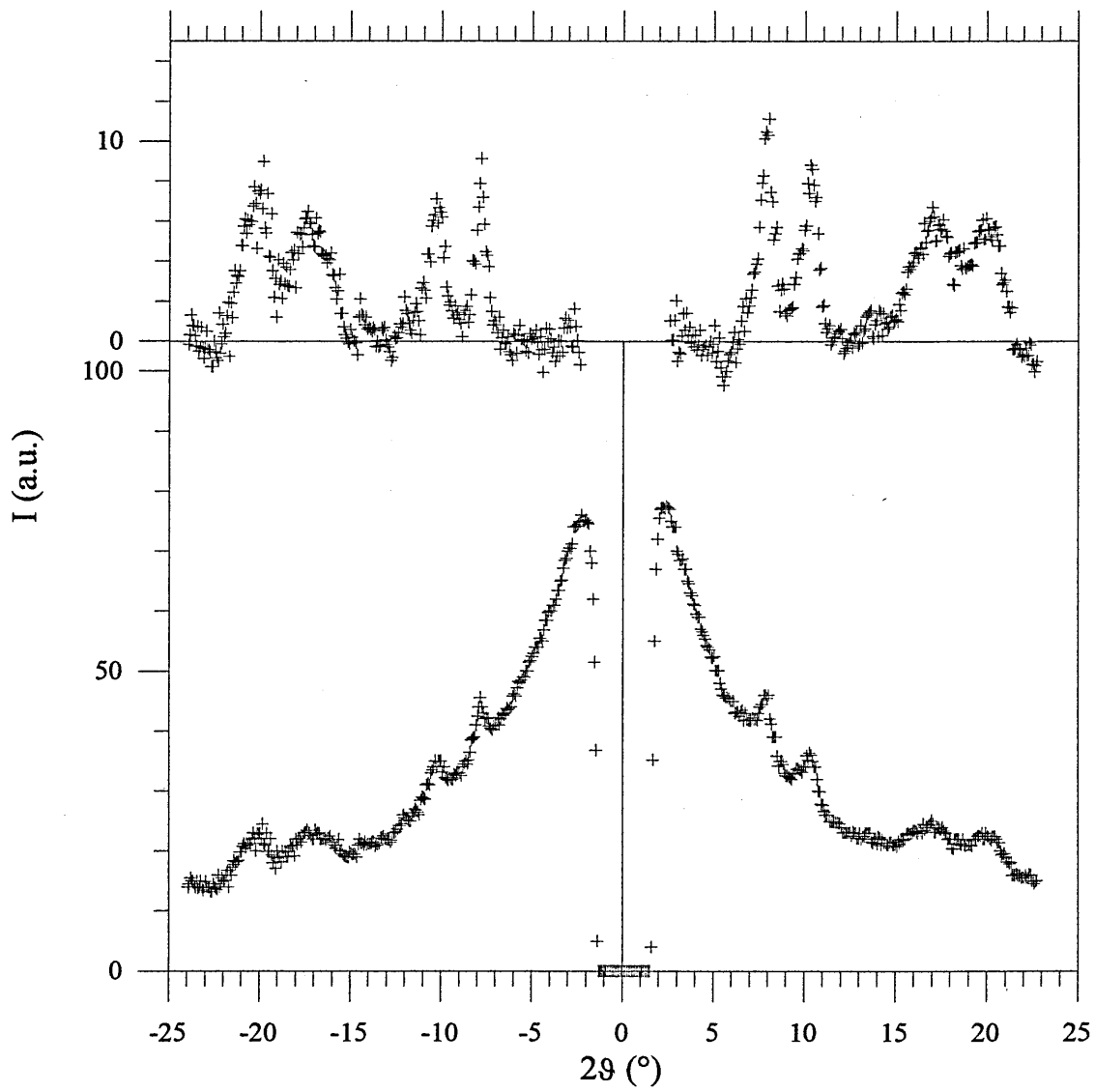
Figure 4.1.

Scattered intensity across the equator for a δ-phase sample before (bottom) and after (top) background subtraction.

Interplanar Spacings (Å)			Assignment from
Measured	Chatani et al. [11] sPS/toluene	Wang et al. [16] sPS/ethylbenzene	Chatani's unit cell
11.40	11.34	11.34	010
8.72	8.66	8.77	$\bar{2}10$
6.27	6.60	6.64	$\bar{1}11$
5.15	5.15	5.16	210
4.32	4.42, 4.33, 4.29	4.39	$\bar{2}30, \bar{4}20, \bar{4}10$
3.77	3.78, 3.76, 3.69 3.83, 3.77, 3.75, 3.73	3.84	030, 400, 220 $\bar{2}31, \bar{4}21, \bar{4}11, \bar{3}31$
3.19	3.27, 3.20 3.14, 3.09, 3.06	3.24	$\bar{2}40, \bar{4}40$ $\bar{3}22, 212, 302$
4.02	3.85		002

Table 4.2.

Comparison between measured and published

interplanar spacings for the δ-phase and assignments.

The sPS/toluene complex has been shown to have a monoclinic $P2_1/a$ structure, with the

parameters listed in table 4.3 [11]. Systematic absence conditions are as follow : hk0 when

h is even and 00l when l is even. No evidence was found for departures from a monoclinic

structure, and the unit cell parameters were refined on this basis. The cell parameters

obtained in this way for sPS/ethylbenzene showed only minor differences compared with those reported for sPS/toluene (table 4.3).

Unit Cell Parameters	Work of Chatani et al [11]	This work
a / nm	1.76	1.77
b / nm	1.33	1.34
c / nm	0.77	0.80
γ /deg	121.2	121.7

Table 4.3.

Values obtained for the unit cell parameters of sPS/ethylbenzene (final column) compared with previous values quoted for sPS/toluene [11] (middle column).

4.2.2.2. The γ-phase

The γ phase was indexed by Chatani et al. [11] in terms of a monoclinic structure, but the exact unit cell dimensions were not provided. We indexed our X-ray pattern in a similar way to the pattern for the δ-phase (table 4.4).

The resulting cell parameters are consistent with data presented earlier, in that the b dimension shrinks by about 1.6Å [11, 16] upon the transition from the δ to the γ phase, while the a and c dimensions remain approximately constant. Results are presented in table 4.5.

Interplanar Spacings (Å)			Assignment
Measured	Wang et al. [16]	Manfredi et al. [14]	(hkl)
9.44	9.59	9.61	010
8.40	8.62	8.59	$\overline{2}10$
	7.31		200
6.24	6.40	6.37	$\overline{1}11$
5.50	5.66	5.57	$\overline{2}20$
4.39	4.50	4.48	210
3.99	4.00		002
3.55	3.61		$\overline{2}12$
3.12	3.22	3.19	$\overline{3}22$

Table 4.4.

Comparison between measured and published interplanar spacings for the γ-phase and assignments.

Unit Cell Parameters	Work of Chatani et al [11]	This work
a / nm	"retained"	1.70
b / nm	"shortened by about 2Å"	1.18
c / nm	"almost the same"	0.80
γ /deg		127.1

Table 4.5.

Values obtained for the unit cell parameters of sPS in the γ-phase compared with information quoted previously [11] (middle column).

4.2.2.3. The α-phase

Interplanar spacings for the sample in the α-phase are presented in the table 4.6

Interplanar Spacings (Å)		Assignment
Measured	Greis et al. [12]	(hkl)
13.23	13.13	110
7.58	7.580	300
7.12	See text	
6.53	6.565	220
4.80	4.962	410
4.32	4.351	211

Table 4.6.

Comparison between measured and published interplanar spacings for the α-phase and assignments.

Because of the uncertainties, we are not able to distinguish between the two modifications of the α-phase, α' and α'' [44], the interplanar spacings differing from one form to the other by about 0.5% only. The reflection at d = 7.12Å is not expected for the α-phase, but (see following section) : it occurs in the β-phase and corresponds to the 040 reflection. Thus the heating process we employed for the formation of the α-phase also allows the formation of a small proportion of crystallites in the β-phase.

4.2.2.4. The β-phase

Interplanar spacings for the sample in the β-phase are presented in the table 4.7

Interplanar Spacings (Å)		Assignment
Measured	Chatani et al. [54]	(hkl)
14.51	14.40	020
8.55	8.425	110
7.12	7.205	040
6.45	6.493	130
4.76	4.803	060
4.39	4.338	111

Table 4.7.

Comparison between measured and published interplanar spacings for the β-phase and assignments.

As for the α-phase, because of the uncertainties, we are not able to distinguish between the two modifications of the β-phase, β' and β'' [44].

The α- and β-phases were obtained by heating a sample initially in the δ-phase. Samples in the α- and β-phases can also be obtained by crystallisation from the melt. The resulting morphologies and the cell parameters obtained by these two processes are identical. Since the α and β forms were not investigated in detail here, the unit cell dimensions were not determined.

4.3. Small Angle X-Ray Scattering

Small angle X-ray scattering was used in order to determine the long period l_x of the crystalline lamellae. This will allow us to correlate this dimension of the crystallite to the chain configuration. This will also provide us information about the mechanisms involved during the phase transitions. This information will be presented in conjunction with FTIR, DSC and TGA data in a combined study (section 4.7). The orientation of the lamellae within the mat can also be determined by SAXS. The complete orientation function was determined and an important parameter for the analysis of anisotropic small angle neutron scattering measurements was also extracted.

Instrumentation

Small Angle X-Ray Scattering were carried out on a Rigaku-Denki camera with a camera length of 316 mm. Copper K_α radiation, pinhole collimation and photographic detection were used. Densitometer traces were recorded using a Wooster Mark III microdensitometer from Crystal Structure Ltd. When heating of a sample was required, a hot stage equipped with a temperature controller TMS 92 from Linkam was used.

4.3.1. Results

4.3.1.1. Determination of the long period

Pictures 4.6 and 4.7 show typical SAXS patterns for the δ phase and the γ phase respectively. They consist of two symmetric arcs extending over an azimuthal angle of 60° and corresponding to the first order reflection. The radial width of these arcs is approximately 0.5°. The shadow of the beam stop appears in the center, surrounded by air scattering.

We took densitometer traces of these X-ray pictures through the intensity maxima. The results are shown on figures 4.2 and 4.3. The intensity after subtraction of the background is presented on the top of these figures. A Gaussian function gives a good fit to these peaks,
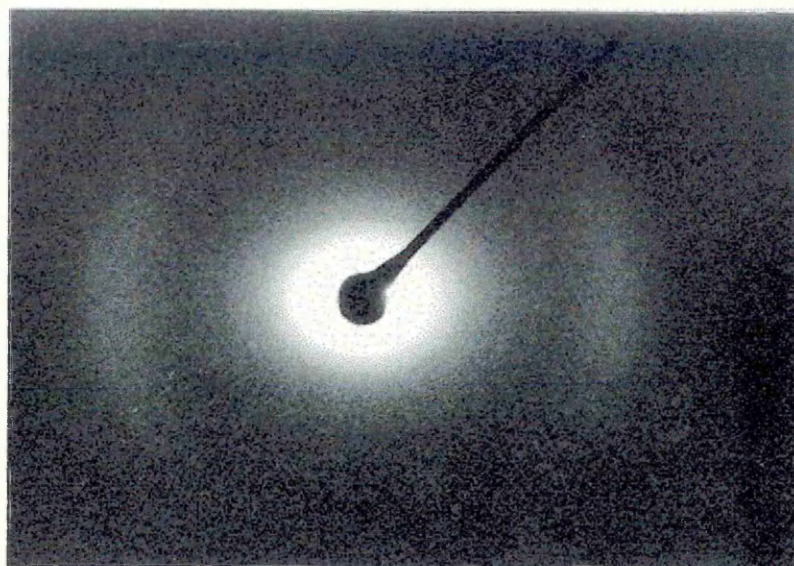
Picture 4.6.

Typical SAXS pattern for the δ-phase. The mat surface was oriented perpendicular to the X-ray beam.
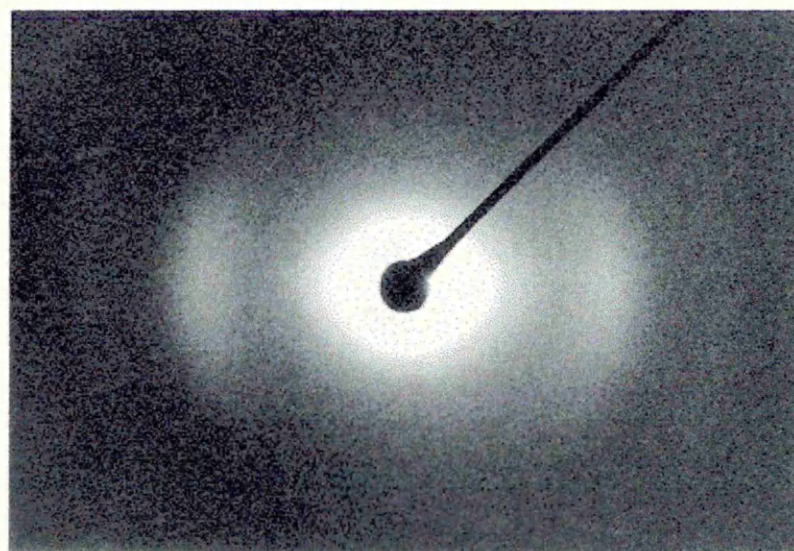
Picture 4.7.

Typical SAXS pattern for the γ-phase. The mat surface was oriented perpendicular to the X-ray beam.
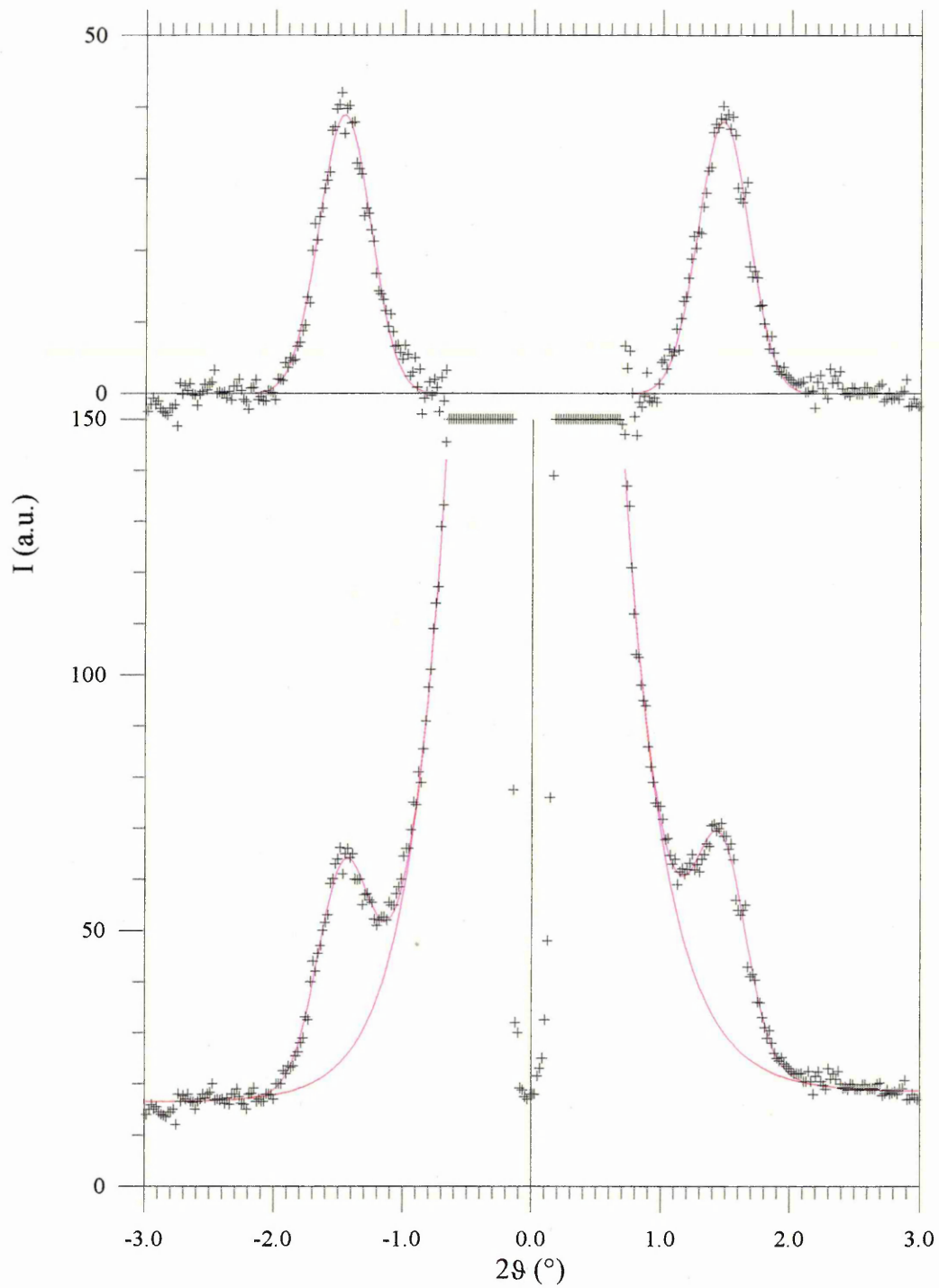
Figure 4.2.

Typical Small Angle X-ray intensity curve for a mat in the δ phase crystallized at 40°C. The sample was placed edge on. The top trace was obtained after background subtraction.
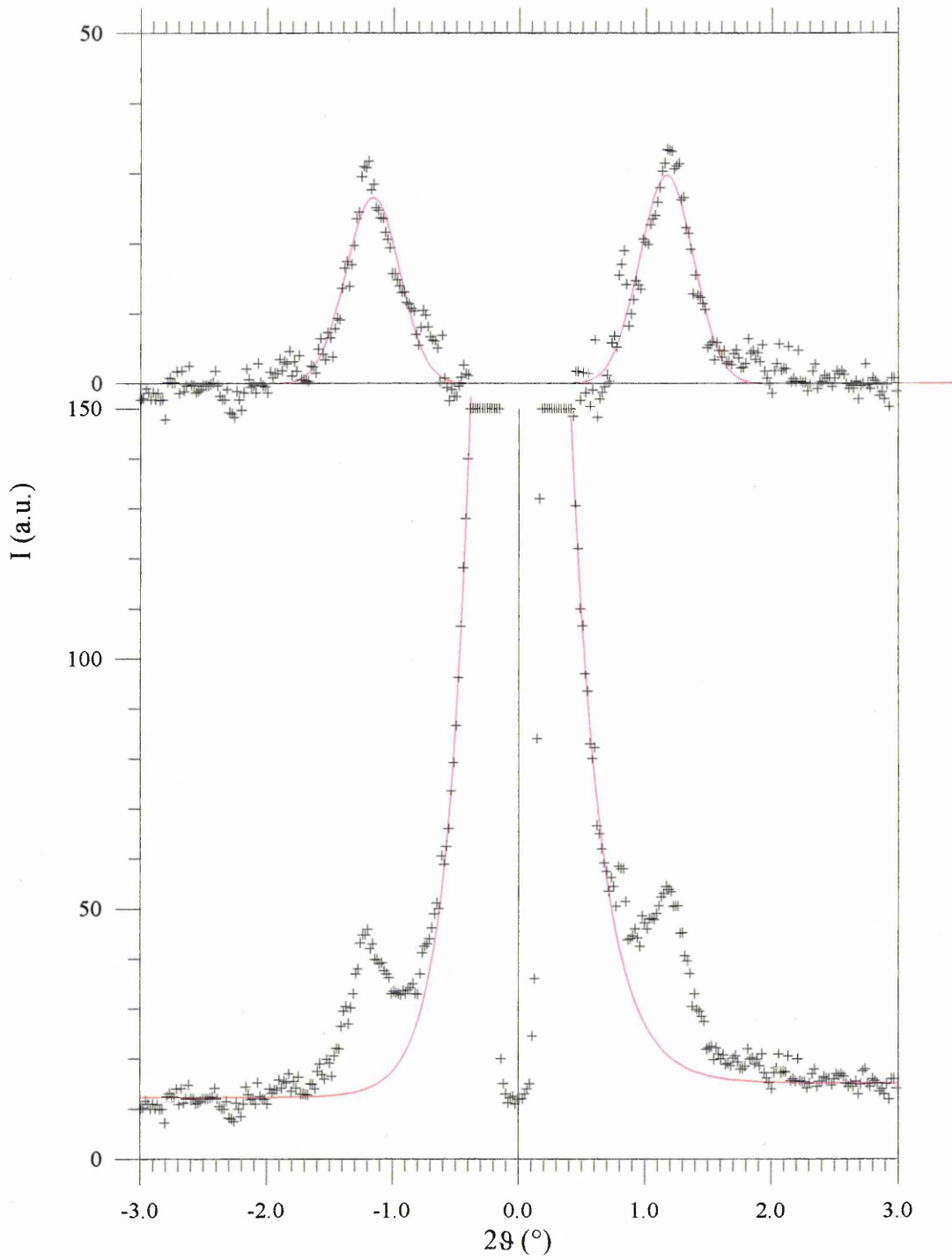
Figure 4.3.

Typical Small Angle X-ray intensity curve for a mat in the γ phase. The sample
was placed edge on. The top trace was obtained after background subtraction.

from which their exact positions were determined and used in order to calculate the long periods :

$$\delta \text{ phase :} \qquad l_x = 60.1 \pm 1.1 \text{Å}$$

$$\gamma \text{ phase :} \qquad l_x = 75.7 \pm 2.0 \text{Å}$$

For different samples crystallized under the same conditions, the long period was found to be identical. Also, very small variations of the long period were detected for samples submitted to identical heat treatments.

From the width of the Gaussian functions used for the fits, the full widths at half maximum of the intensity maxima were

$$\delta \text{ phase :} \qquad \Delta\theta = 0.467°$$

$$\gamma \text{ phase :} \qquad \Delta\theta = 0.502°$$

The slight increase (7.5%) indicates that there is a small heterogeneity of lamellar thickening on transition from δ to γ. This is generally expected for annealed solution grown crystals. Broad low-angle X-ray diffraction maxima imply a wide distribution of lamellar thickness.

4.3.1.2. Determination of the lamellar orientation distribution

A series of densitometer traces were taken at different azimuthal angles γ through the intensity maxima. It was assumed that each lamella with normal **n'** will contribute equally to the diffraction intensity. In this case the integrated intensity measured at an angle γ is

proportional to the number of lamellae of which the normal **n'** is at this angle to the normal of the mat **n**.

Results for the angular distribution of the lamellae are presented on figure 4.4. As can be seen, the lamellae are preferentially oriented along **n**. The orientation is well described by a Gaussian.

To characterise the distribution, we will calculate the Legendre polynomyal $P_2(\gamma)$, defined by

$$P_2(\gamma) = \frac{3 < \cos^2 \gamma > -1}{2}$$

where

$$< \cos^2 \gamma > = \frac{\int_0^{\pi/2} I(\gamma) \sin\gamma \cos^2 \gamma d\gamma}{\int_0^{\pi/2} I(\gamma) \sin\gamma d\gamma}$$

$P_2(\gamma)$ is the first term of the orientation distribution. For perfect orientation of the lamellae parallel to **n**, $P_2(\gamma)=1$, while in the case of a random distribution $P_2(\gamma)=0$. Using the plot of figure 4.4 we found $P_2(\gamma)=0.34$, a somewhat smaller value than Sadler's value of 0.57 [18] for solution crystallized polyethylene.
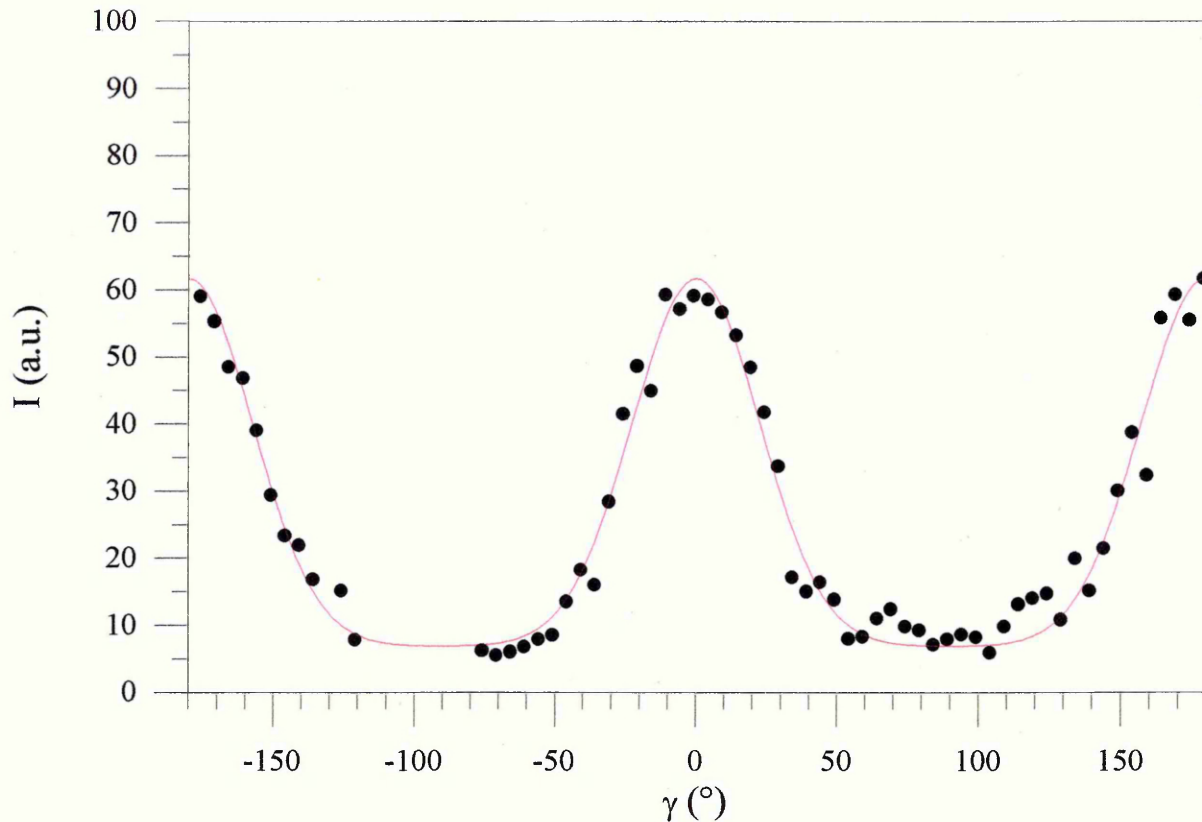
Figure 4.4.

Azimuthal variation in diffraction intensity for small angle scattering for a mat in the δ phase crystallized at 40°C.

4.3.1.3. Long period with crystallization temperature

Samples crystallized at different temperatures were prepared by P. Sonntag. Figure 4.5 shows the variation of the X-ray long period (l_x) with T_c. Although the magnitude of the change is small, the observed increase in l_x with increasing T_c is consistent with the behaviour normally observed for crystalline polymers (see ref. [84]). An inverse proportionality between the long period and the degree of undercooling $\Delta T = T_m^0 - T$

(where T_m^0 is the melting temperature of a crystal without surfaces, and T is the

crystallization temperature) is predicted theoretically.
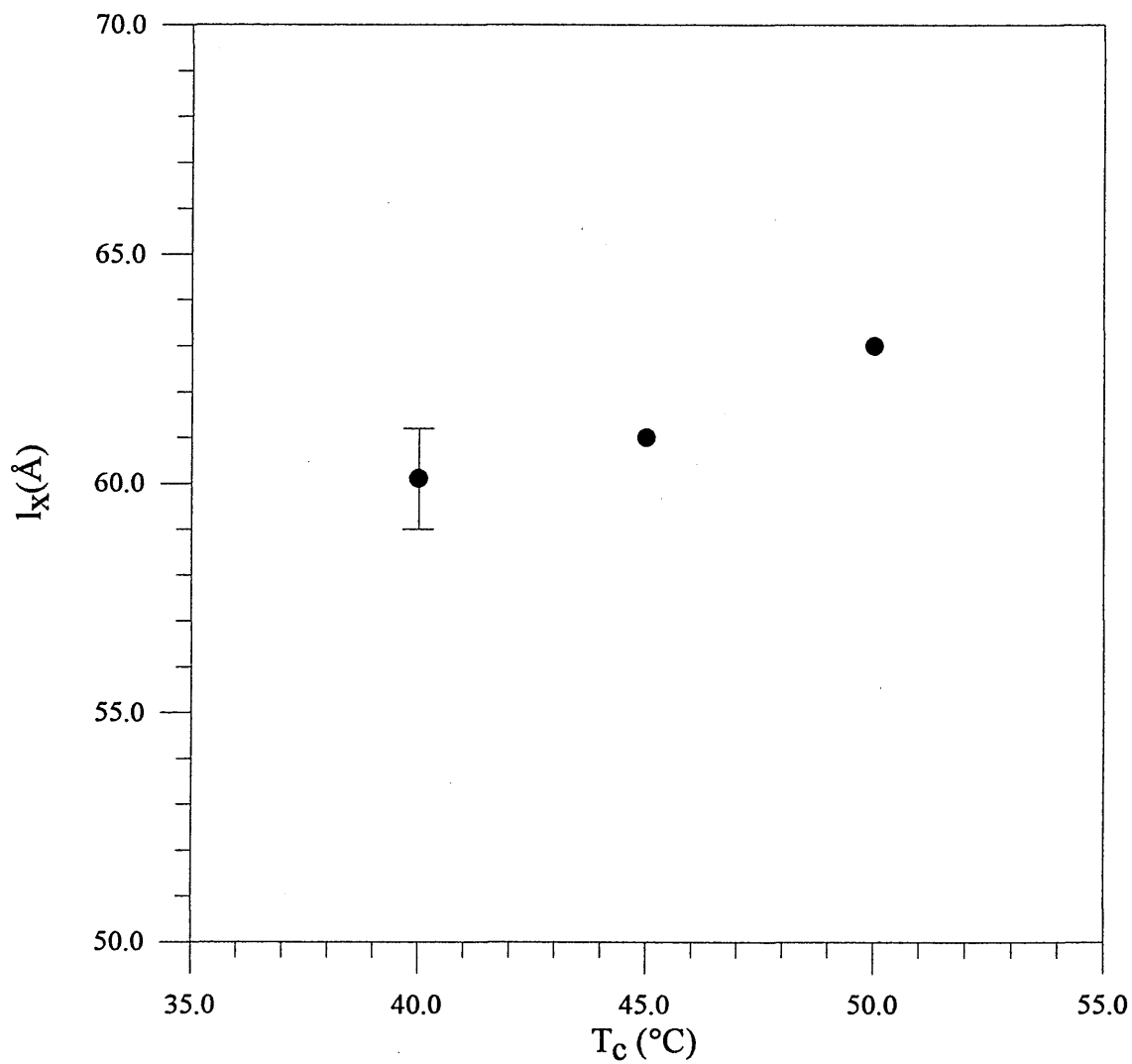
Figure 4.5.

Long period versus crystallization temperature for sPS crystallised from dilute solution in ethylbenzene.

4.3.1.4. Long period with annealing temperature

We heated a piece of mat initially in the δ phase from room temperature to T_a, by steps of 10°C, T_a ranging from 80 to 170°C. The rate of heating was 10°Cmin^{-1}. After reaching T_a, the sample was cooled to room temperature and analyzed by SAXS before heating from the previous T_a to the next value. Another set of SAXS experiments was performed by P. Sonntag. It consisted of heating a piece of mat for 30 min at a given temperature before recording the SAXS pattern at room temperature.

Results are shown on figure 4.6. The long period, initally 59 Å, starts increasing at about 80°C. This increase continues up to around 120°C, after which the thickness remains constant up to 180°C, and then increases again.

It is well known that annealing generally results in the thickening of polymer crystals. Two mechanisms may explain this thickening : crystallization and annealing. In the first process, crystallization of amorphous material increases the periodicity of the electron density function along the stack. In the second process, chains have a mobility which allows them to slide longitudinally. We will see later that this thickening at the transition from δ to γ cannot be explained by crystallization of amorphous material, and that annealing probably occurs.

As previously mentioned, the γ-phase samples used for neutron scattering were obtained by fast heating in comparison to the relatively slow heating (10°Cmin^{-1}) used here. For the fomer samples, the measured long periods were significantly smaller (75.7Å) than the value obtained at 135°C from figure 4.6 of about 92Å. Dependence of the long period on

the heating rate, as well as the annealing temperature, has previously been noted for polyethylene [36], and the behaviour here is consistent with a delay in the thickening process for high heating rates in comparison to slower heating rates.

The transition from the γ phase to the α phase occurs with a significant change in long period. There are two possible explanations for this thickening in addition to lamellar thickening generally observed on approaching the melting temperature. First, recrystallisation may occur with the transition. Second, we know that the transition involves a change in molecular configuration from helical to planar zigzag. Both phenomena may result in changes of long period, in the first case through the transformation of amorphous material into the crystalline state and in the second through a decrease in the number of monomers per unit length of stem of about 25% (figure 1.7), and as a result an overall increase of the chain extension within the crystal.
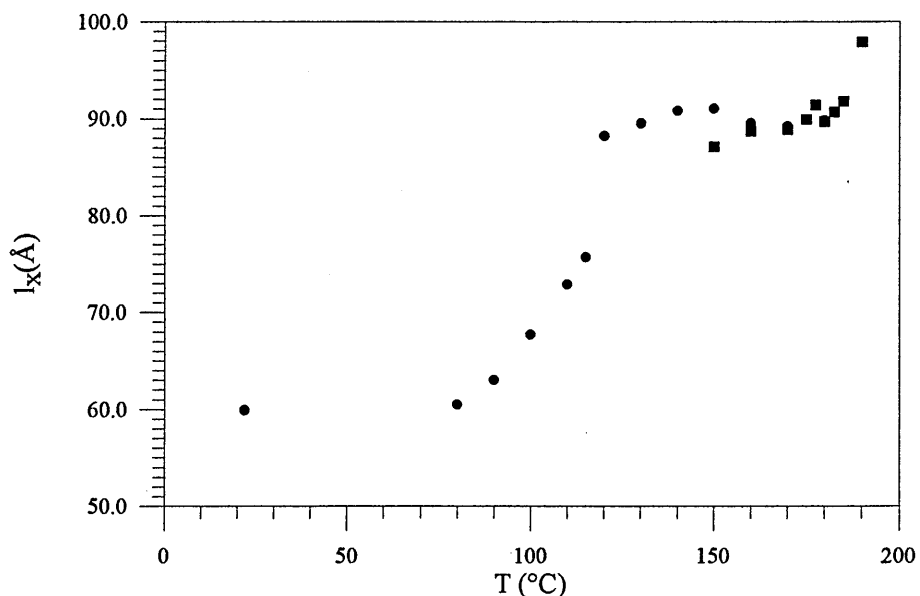

Figure 4.6.

Long period versus annealing temperature for solution-crystallised mats ● annealing time 15 s, ■ annealing time 30 min.

109

4.4. Neutron crystallography

Although a crystallographic study of the different phases was not our first concern, the available momentum transfer range used with the D17 instrument at ILL and the new HAB detector at ISIS allowed to cover partially the crystallographic range. For sPS crystals, the unit cell dimensions are quite large, and thus the corresponding momentum transfer range required is relatively low (the first reflection, namely [010] is expected for the δ-phase at $q=0.55\text{Å}^{-1}$).

For the δ-phase, two types of material were available: protonated polymer in protonated solvent and deuterated polymer in protonated solvent. As was demonstrated in section 3.2.2, the form factor of such mixtures is different and so is the intensity of a given reflection. This is illustrated in figure 4.7 where the intensities of these two samples are compared. For the deuterated polymer the [010] peak appears very clearly and, with a smaller intensity, the [$\bar{2}$10]. On the other hand, the intensity of the protonated sample shows no such peaks. We calculated the intensities using equation 3.38 for these two materials. We used the simple approximation of considering the total scattering length density of a solvent molecule as located at its centre of gravity. This approximation is considered reasonable where the solvent molecules undergo rotational motion. The results of these calculations are shown in figure 4.8 and demonstrate that a significant [010] peak is only expected for the deuterated polymer with protonated solvent. The particular behaviour of this peak upon deuteration can be understood in view of the crystal structure proposed by Chatani, where sheets of polymers and sheets of solvent alternate in the [010]

direction (figure 1.9), giving a maximum scattering density variation along this direction. These results confirm this aspect of Chatani's model.

In figure 4.9, the neutron diffraction peaks of the [010] reflection obtained by the two instruments are compared. For D17, the incident beam is characterized by a relative width at half-height $\Delta\lambda/\lambda$=10%. The relative widths at half-height for the [010] peak are $\Delta q/q$=10.2% and 11.0% for D17 and LOQ respectively. Figure 4.9 also shows the diffraction pattern of the sPSD sample in the γ-phase obtained by D17. In this case, the [010] peak is beyond the wavevector range available.
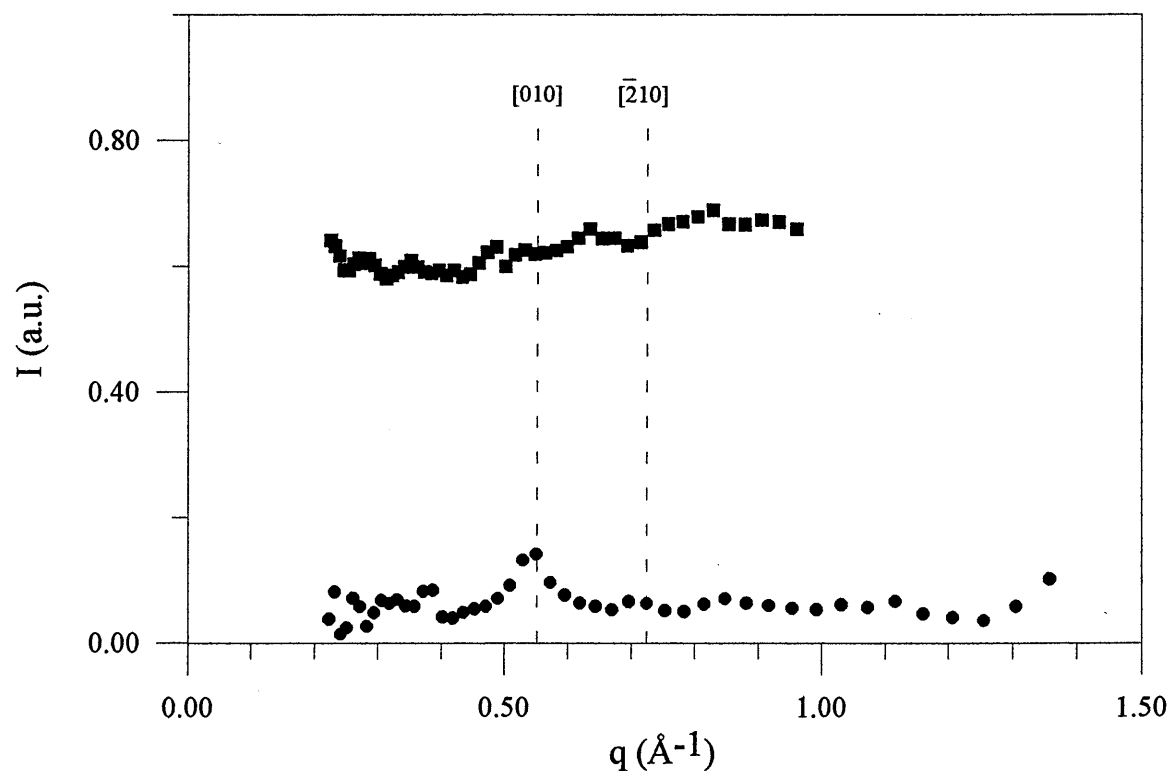
Figure 4.7.

Measured neutron diffraction patterns for sPS/ethylbenzene in the δ-phase: top hydrogenous sPS in hydrogenous ethylbenzene (■), bottom deuterated sPS in hydrogenous ethylbenzene (●).
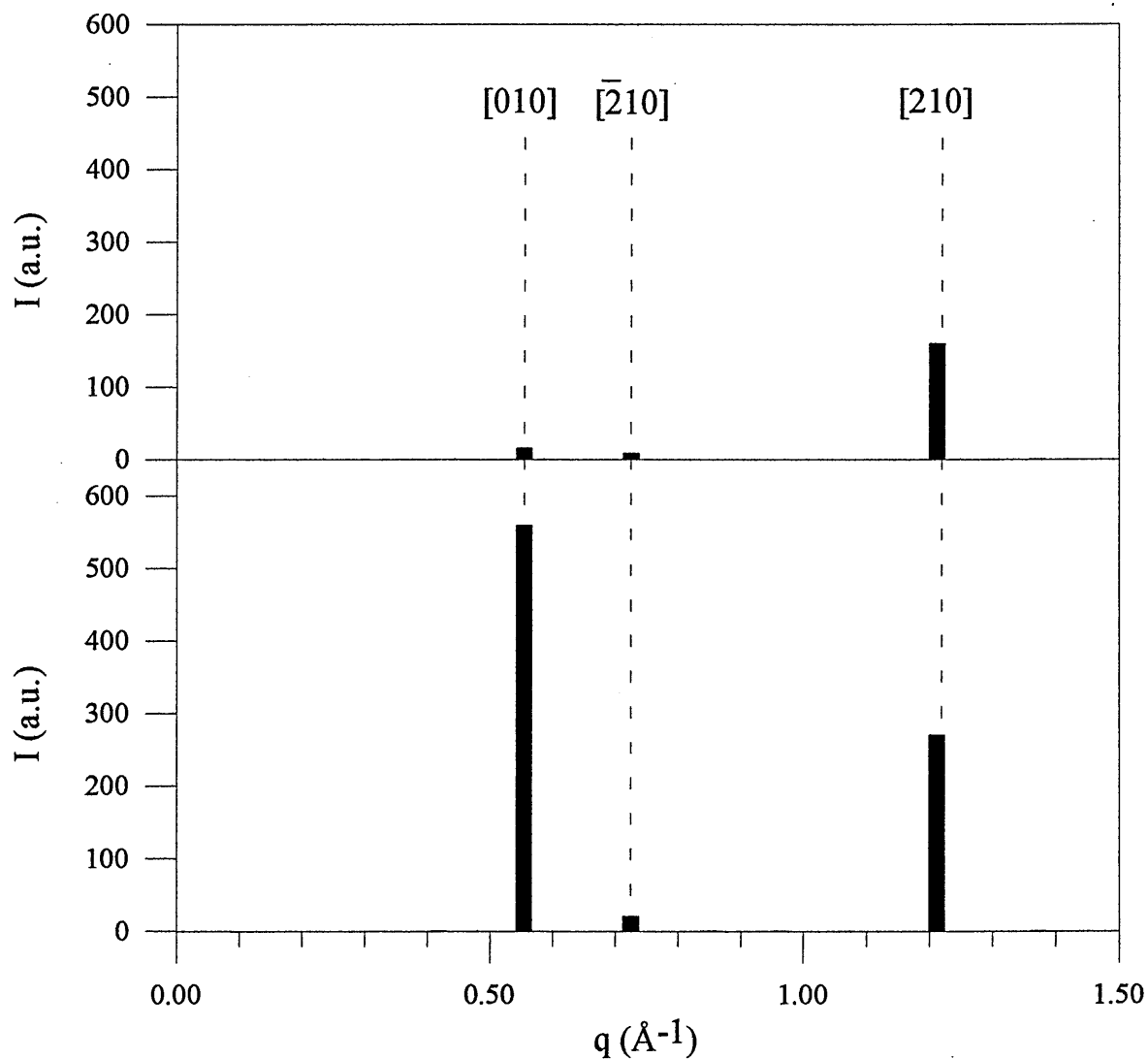
Figure 4.8.

Calculated neutron diffraction pattern for sPS/ethylbenzene in the δ-phase: top: hydrogenous sPS in hydrogenous ethylbenzene, bottom: deuterated sPS in hydrogenous ethylbenzene. Calculations were based on the crystal structure presented by Chatani, using the simple approximation of considering the total scattering length density of a solvent molecule as located at its centre of gravity.
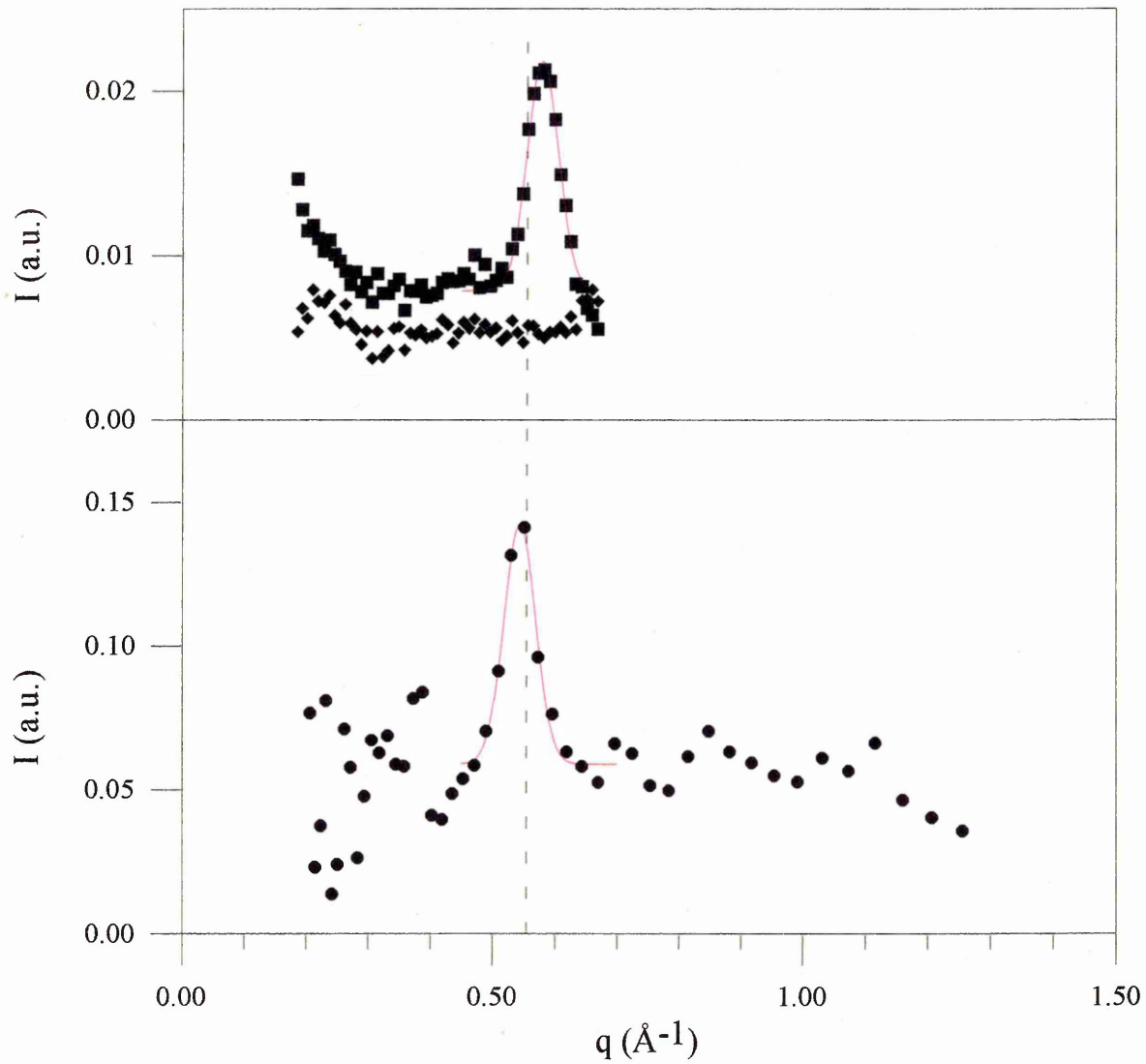
Figure 4.9.

Comparison of the [010] reflection obtained by LOQ ($\bullet$) and D17 ($\blacksquare$) instruments for sPSD/EthylH in the δ-phase. Also presented on this graph, the neutron diffraction pattern of the γ-phase by D17 ($\blacklozenge$).

4.5. Differential Scanning Calorimetry

4.5.1. Phase diagram

4.5.1.1. Experimental

The thermal behaviour of sPS gels, and the phase diagram were established by means of a Mettler DSC 30 apparatus. Calibration was made using indium for which the enthalpy and the melting temperature are well known (T_{In}=156.6°C, ΔH_{In}=28.45 J/g). For gel concentrations below 25% (w/w), homogeneous solutions were prepared in test-tubes and a gel was formed. Pieces of gel were then introduced into stainless steel pans that were hermetically closed. For the high concentrations, pieces of gel were prepared by solvent evaporation. Prior to any measurements, the gels were melted at 150°C for 15 min in the DSC pan and quenched to room temperature in order to ensure homogeneity of the gels. A heating rate of 5°Cmin^{-1} was then used for all the samples.

4.5.1.2. Results

Typical DSC heating traces are given in figure 4.10 for different polymer concentrations. As can be seen, the DSC traces display one endotherm up to a concentration C_p=0.39 gg^{-1}. The temperature associated with the low-melting endotherm increases with increasing

polymer concentration up to $C_p=0.35$ gg^{-1}, and then remains nearly constant at larger concentrations ($T_{low} \cong 120°C$ for $C_p>0.35$ gg^{-1}).

For more concentrated systems, the low-melting endotherm is followed by two endotherms, one appearing as a shoulder on the side of a high melting endotherm (see figure 4.10, $C_P=51\%$). The temperature associated with the high-melting endotherm increases continuously with increasing concentration in the range of concentrations investigated. The temperature of the third edotherm is constant. For the highest concentrations ($C_p>0.65$ gg^{-1}), a fourth endotherm appears. Its temperature is also constant. The temperature/concentration phase diagram drawn in figure 4.11 highlights these different types of behaviour. The variations of the enthalpies calculated from the area of each endotherm as a function of polymer concentration are represented in the same figure. The enthalpy associated with the low-melting endotherm (●) first increases linearly up to a polymer concentration $C_P=0.41$ gg^{-1} and then decreases to become zero at about $C_P=0.67$ gg^{-1}. Conversely, the enthalpy associated with the high-melting endotherm (+) increases continuously. Also presented in figure 4.11 is the enthalpy of the third endotherm (∗). Again the enthalpy first increases linearly up to $C_p=0.67$ gg^{-1} (where the enthalpy of the low melting endotherm becomes zero) and then decreases to become zero at about $C_p=0.79$ gg^{-1}. If we assume that there is no significant change in sample crystallinity over the phase diagram, which could modify the form of the Tamman plots, then the variations of the low-melting enthalpies and the melting temperatures are consistent with the existence of three polymer/solvent compounds C_1, C_2 and C_3. The stoichiometry of C_1 is given by the position of the maximum of the enthalpy for the low-melting endotherm,
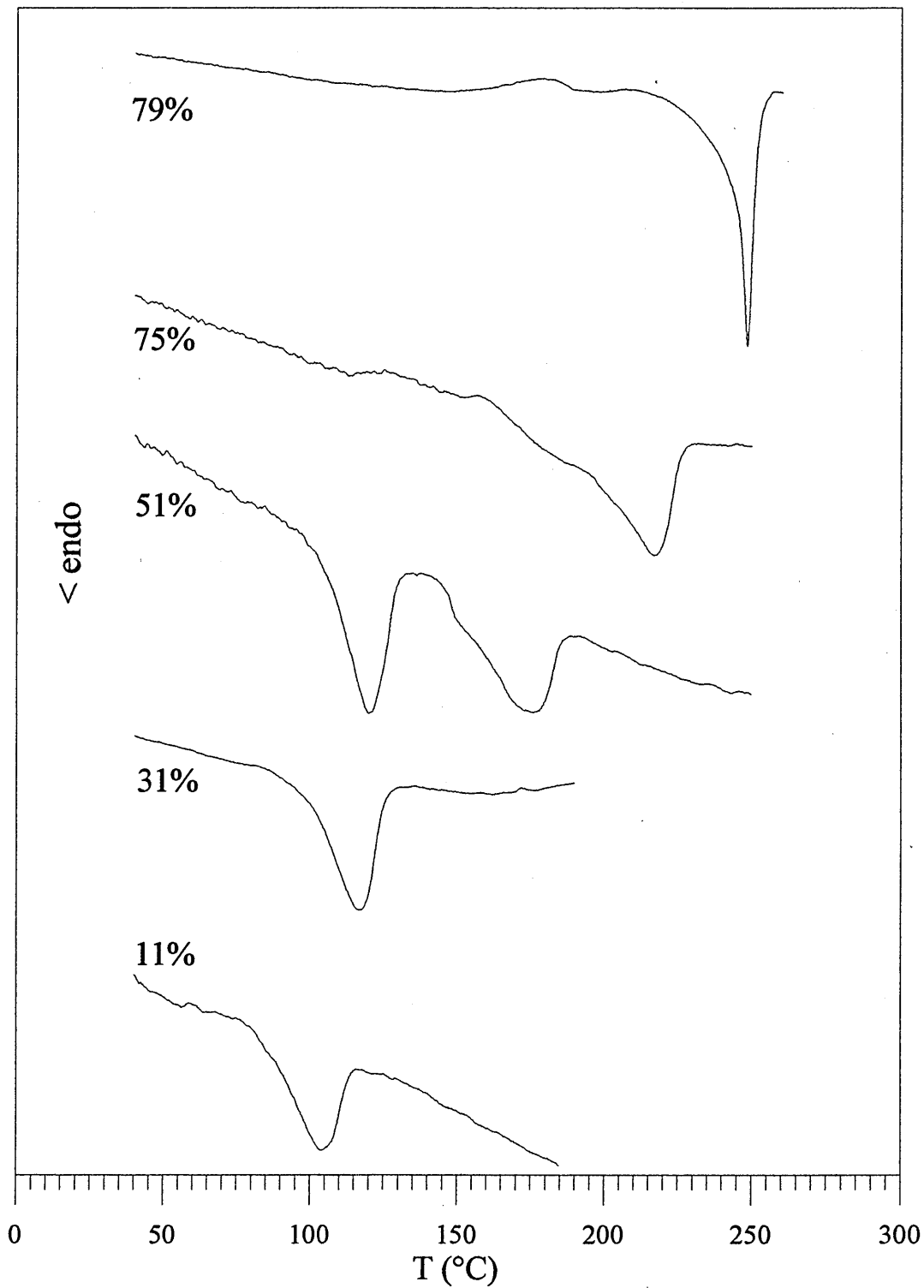
Figure 4.10.

Typical DSC traces obtained on heating sPS/ethylbenzene gels at 5°Cmin⁻¹.
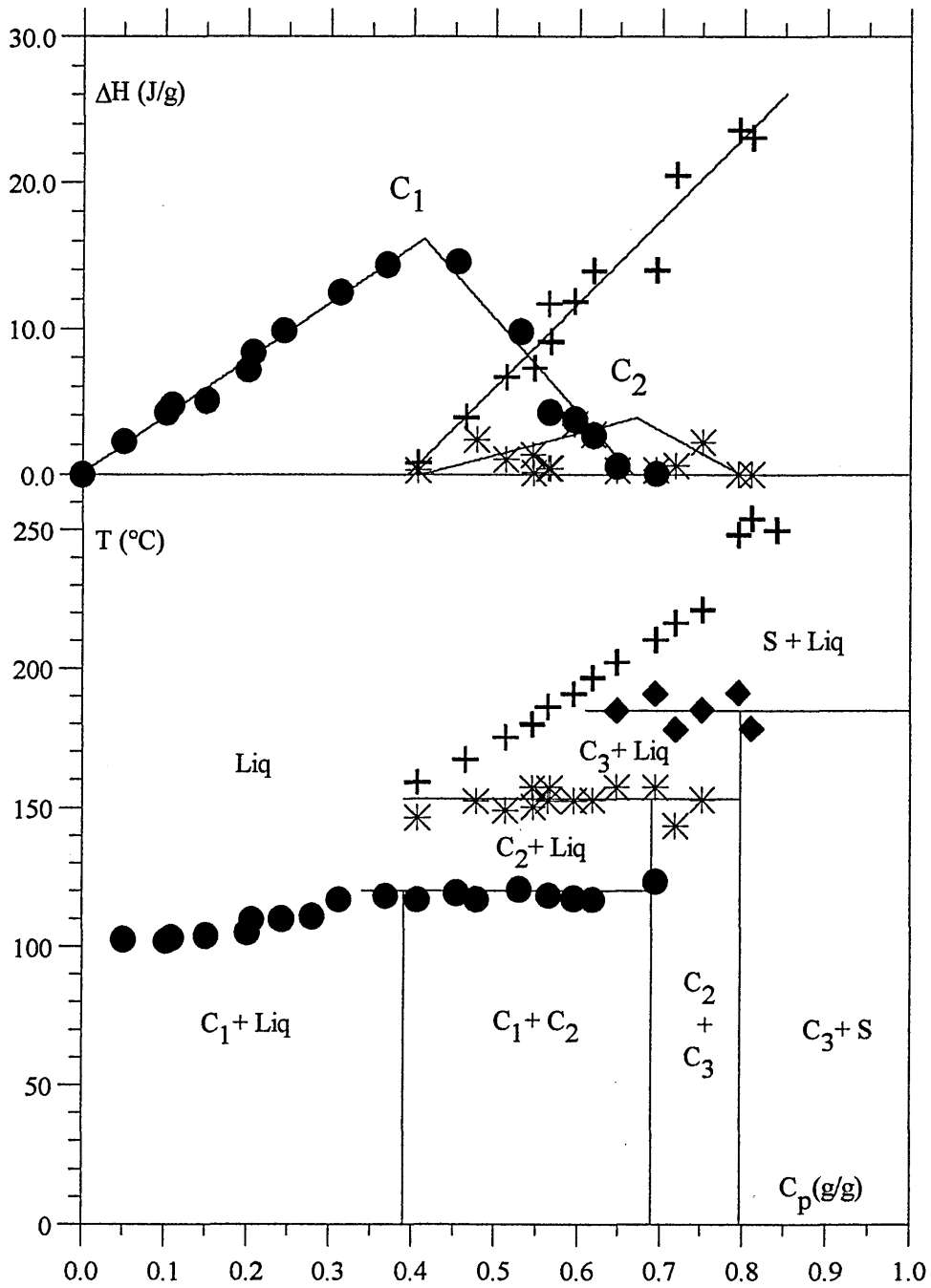
Figure 4.11.

Bottom: temperature/concentration phase diagram for the sPS/ethylbenzene system. As is customary, full lines stand for known transitions. ●=fusion of C_1, ✳=fusion of C_2, ◆=fusion of C_3, +== fusion of S. Top: Enthalpies associated with the various thermal events: ●=fusion of C_1, ✳=fusion of C_2, += fusion of S.

namely 1.4 ethylbenzene molecules per monomer unit. This compound is also an incongruently-melting compound as the maximum in the low-melting endotherm enthalpy and the onset of the invariance of T_{low} do not occur at the same concentration (see section 2.3.1.3). The stoichiometry of the second compound C_2 is given by the concentration at which the low-melting enthalpy becomes zero, namely about 0.5 ethylbenzene molecules per monomer unit. At this concentration the enthalpy of compound C_2 is maximum. The stoichiometry of compound C_3 is given by the concentration where the enthalpy of C_2 becomes zero, approximately 0.25 ethylbenzene molecules per monomer. This stoichiometry corresponds to that given by Chatani et al. for the compound obtained by exposure to toluene vapour. It is worth noticing that according to stoichiometry measurements, compound C_1 of the sPS/ethylbenzene complex is less solvated than sPS/benzene (4/1) and more solvated than sPS/chloroform (1/1) and sPS/toluene (0.8/1).

4.5.1.3. Comments

In table 4.8, we show stoichiometries obtained for complexes formed by sPS with various solvents, as determined from DSC measurements. We also show stoichiometries of δ-phases, where these have been reported.

The wide variation in solvent concentration is particularly notable, and would seem to suggest some variability in the solvent distribution within, for example, the C_1 complexes formed. Nevertheless, the ratio of stoichiometries in the C_1 and C_2 complexes is shown to be remarkably similar in all cases (around 3 except for benzene which gives a ratio of 4).

The concept of the complex C_2 involving tightly bound solvent molecules and the complex C_1 including additional loosely bound solvent molecules has previously been introduced for sPS gels [57]. This result indicates that the proportions of the two types of solvent molecules remain constant, irrespective of the molecule involved.

From neutron crystallographic studies by Daniel et al., the [010] reflection appears for the complex C_1 in benzene at $q=0.39\text{Å}^{-1}$ [57] instead of $q=0.51\text{Å}^{-1}$ observed for

Solvent	Stoichiometry (solvent molecules per monomer unit)				Ratio
	C_1	C_2 (*=or S)	C_3	δ	C_1/C_2
Decalin	1.2 [85]				
Toluene	0.8 [58]	1/4 [58]		0.25 [11]	3.2
Iodine				0.5 [51]	
Ethylbenzene	1.4	0.5	0.25	0.25	2.8
Chloroform	1 [58]	0.33* [58]			3
Benzene	4 [57]	1 [57]	C_3 ?		4
Bromobenzene	0.5 [86]	0.17 [86]			2.9

Table 4.8.

Comparison of the stoichiometries for the different sPS gels and crystals with various solvents. Brackets refer to the appropriate references. [†] may be slightly inexact.

compound C_2 in benzene and for all the compounds obtained with chloroform and toluene [58]. This observation has to be combined with the highly solvated nature of C_1 in benzene. It seems therefore that the packing densities of solvent molecules can vary markedly for complexes involving different solvent molecules, keeping the unit cell dimensions identical. It is very likely that in the case of sPS/ethylbenzene, complexes C_2 and C_3, and maybe also C_1, have identical unit cell dimensions corresponding to those of the δ-phase (cf. section 4.2). The reason for such variations in packing density is not clear, since the wide variation in stoichiometries for only slight variations in solvent are not consistent with steric effects alone.

In their model of sPS/toluene crystals, Chatani et al. proposed a crystal structure involving a solvent to monomer ratio of 1:4. This was a different value from the ratio of 1:5.4 obtained from the weight loss measurements (14.1%). In the case of sPS/ethylbenzene, the weight loss is 14.5%, corresponding to a solvent to monomer ratio of 1:6.

From result of Daniel et al. on toluene complexes, it seems that C_2 and the δ-phase in toluene are similar in terms of crystalline structure and stoichiometry. Similarly, in view of the stoichiometry of compound C_3 in ethylbenzene, we think that a ratio of 1:4 is also valid for sPS/ethylbenzene crystals (δ phase). In both cases, the amorphous region can account for the difference between observed and theoretical weight loss. On the other hand, in view of the possibility of producing an "emptied δ" form [14], the variable proportion of solvent molecules is not surprising, and has previously been observed as a result of annealing sPS/methylene chloride samples [53].

4.5.1.4. Summary

We have used DSC measurements to obtain the temperature/concentration phase diagram for sPS/ethylbenzene gels. This shows the presence of three polymer/solvent compounds. Compound C_1 contains 1.4 ethylbenzene molecules per monomer unit, C_2 contains 0.5 solvent molecules per monomer unit and C_3 contains 0.25 solvent molecules per monomer unit. For this last compound, the stoichiometry corresponds to that proposed by Chatani et al. for the δ-phase of sPS in toluene.

4.5.2. The thermogram of the δ-phase

The DSC plot obtained with a heating rate of 10°C/min of a sample initially in the δ-phase shows many events which have previously been described elsewhere (figure 4.12). The feature at 71.5°C on initial heating appears to be the glass transition, albeit at a somewhat lower value than has been reported [47]. Peaks observed at 123.6°C and 158.5°C are identified with the δ to γ transition and recrystallization of γ respectively. At 193.0°C there appears a small endothermic peak immediately followed by a small exothermic peak at 208.0°C. The endotherm is the γ to α transition (slow heating rate [44]), while the exotherm is associated with the recrystallisation of the α form [44]. Finally the large endothermic peak of melting of the α phase appears at 253.3°C.
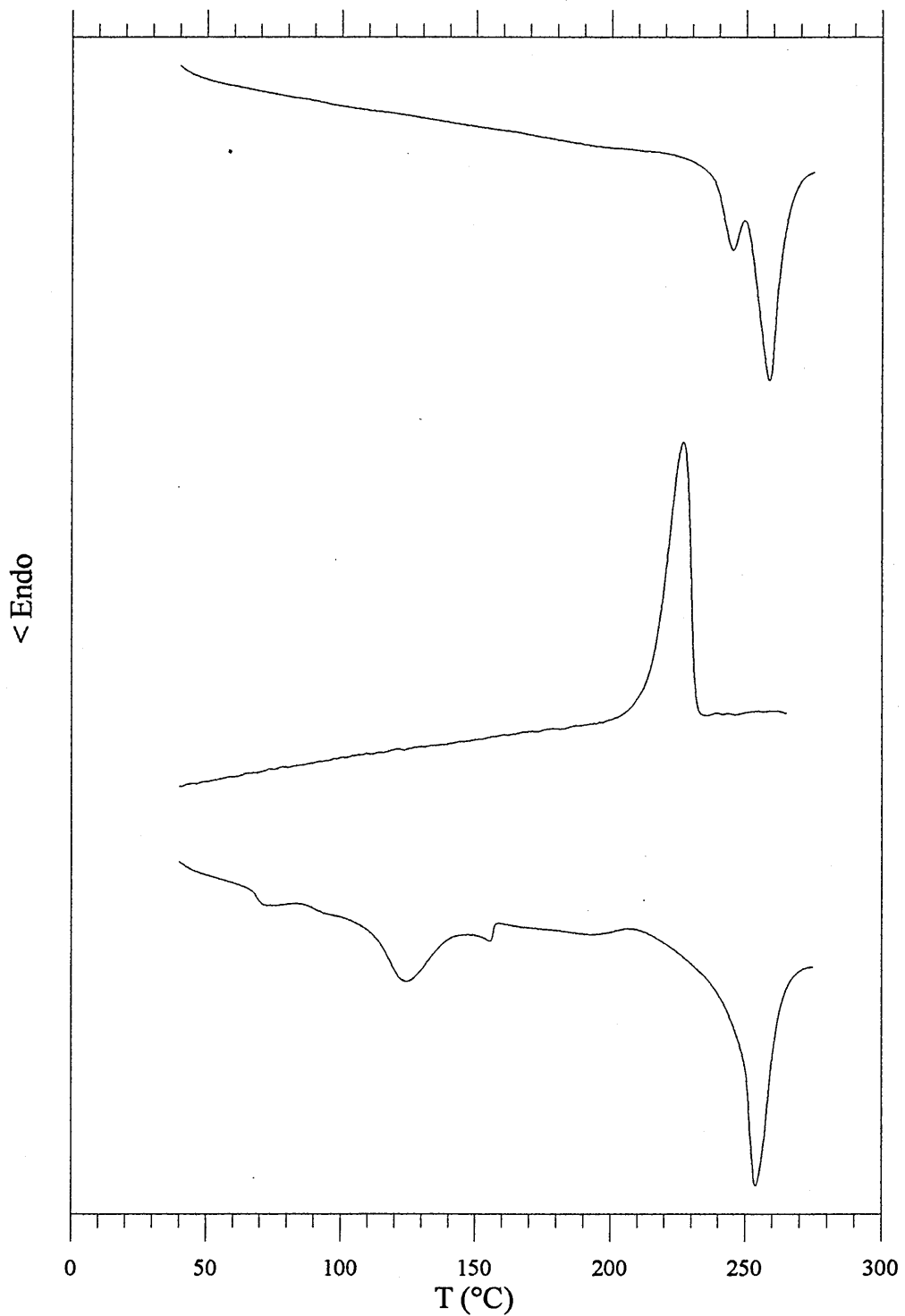
Figure 4.12.

Successive heating (bottom), cooling (middle) and re-heating (top) of a sample of protonated sPS/ethylbenzene initially in the δ-phase. The heating/cooling rates were in all cases 10°C/min.

In figure 4.12, we also show the thermogram of the same sample immediately cooled to room temperature, and heated again. In each case, the cooling and heating rates were 10°C/min. It is known that rapid quenching from the melt leads to the formation of an amorphous sample while slow cooling at room temperature, or moderate quenching can lead to the formation of α- and β-phases repectively. From the presence of two melting endotherms on the DSC trace, it is very likely that both crystalline forms were formed during the previous cooling process. Each endotherm in figure 4.12 (top) represents the melting of one of these forms. Note that we saw in section 4.2.2.3 that upon slow heating of a δ-phase sample, both forms are formed.

4.5.3. Melting temperature of deuterated sPS vs. melting temperature of protonated sPS

It is well known that different molecular weights lead to different crystallization rates. This can lead to segregation upon crystallization if a mixture of two species is involved (molecular weight fractionation), giving rise to inhomogeneity in molecular type over the sample. There are then fluctuations in the density function describing the positions of the molecular centres of gravity, leading to a correlation function which is not uniform.

Another factor which influences the crystallization temperature is different isotopic species (isotopic fractionation). Deuterated polymers have significantly lower melting temperatures then their protonated counterparts. For example, this difference is 4.9°C for polyethylene

and 5.5°C for isotactic polystyrene [39]. Figures 4.13 and 4.14 show the typical DSC thermograms of deuterated (M_w= 124 500) and protonated (M_w=85 400) sPS samples, initially in the δ-phase. From figure 4.13, where the heating rate was 2°C/min, the melting temperatures of protonated and deuterated polystyrene are 266.3°C and 253.9°C respectively, yielding a difference of 12.4°C. For a faster heating rate (10°C/min), the melting temperatures are 253.3°C and 246.1°C respectively, yielding a difference of 7.2°C. The temperatures corresponding to the transitions between the different crystalline forms are also shifted. In table 4.9, these temperatures deduced from figure 4.14 are listed and comparison can be made between the two species for a heating rate of 10°C/min.

Transition	Temperature of Transition (°C)	
	H-sPS	D-sPS
δ→γ	123.6	143.3
γ→α	193.0	?
Melting of α	253.3	246.1

Table 4.9.

Comparison between the temperature of transition of deuterated and protonated sPS as measured by DSC with a heating rate of 10°C/min.
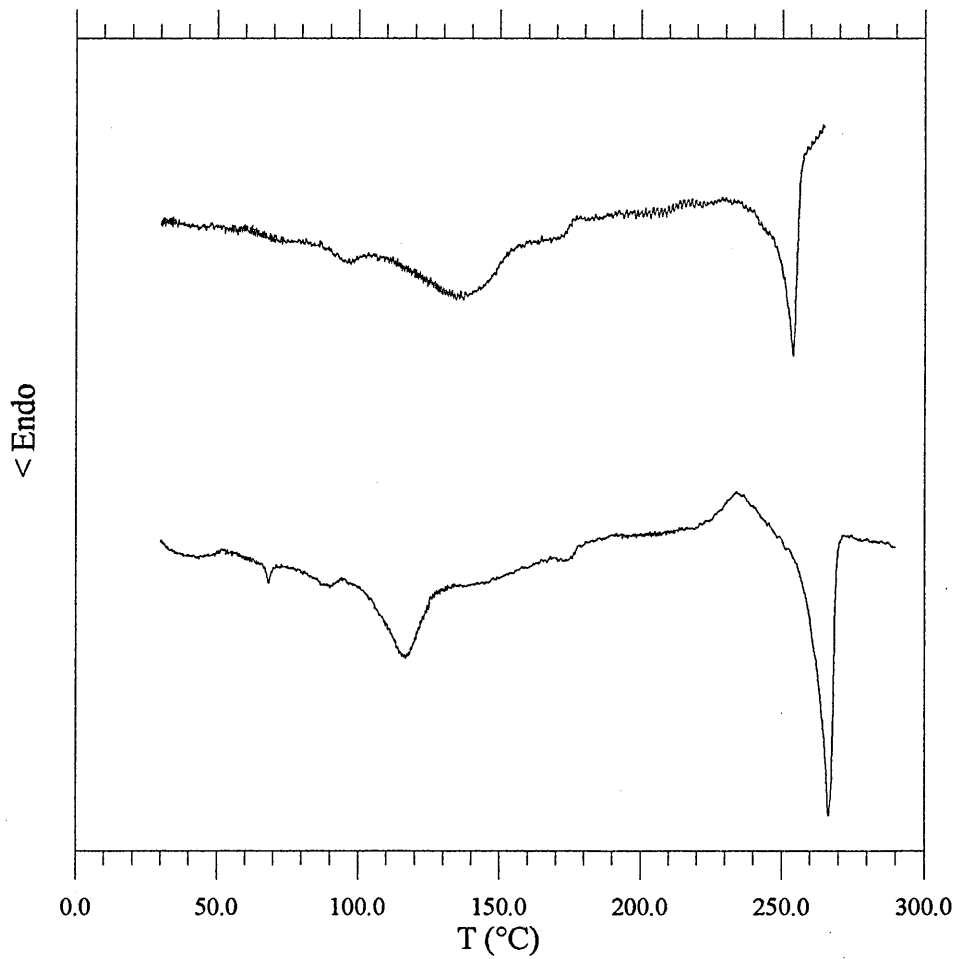
Figure 4.13.

Differential scanning calorimetry thermograms of two samples intially in the δ-phase, protonated sPS (bottom) and deuterated sPS (top). Heating rate 2°C/min.
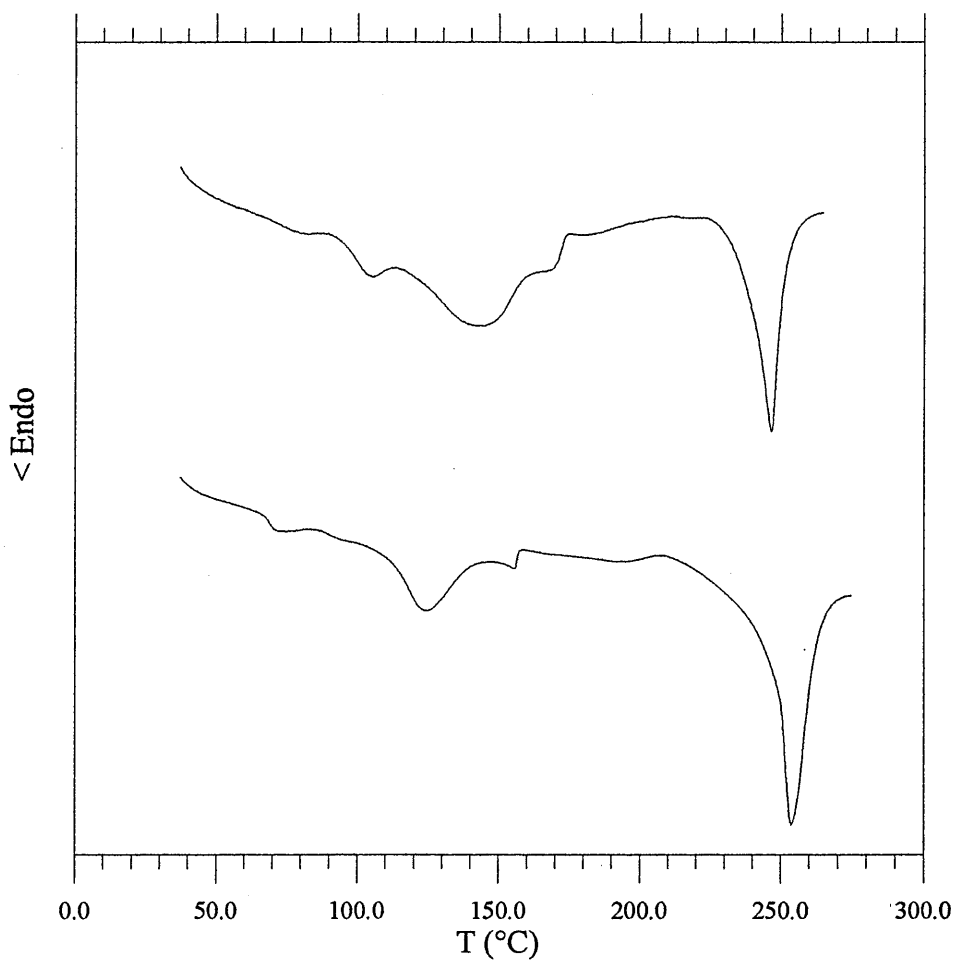
Figure 4.14.

Differential scanning calorimetry thermograms of two samples intially in the δ-phase, protonated sPS (bottom) and deuterated sPS (top). Heating rate 10°C/min.

For the transition δ→γ, the transition temperature of the deuterated polymer is very much higher, and the difference in temperature is 19.7°C. We will make other comments about these differences after the infrared section.

4.6. Infrared Analysis

Introduction

The evolution of the chain configuration can be studied by monitoring the integrated intensity of the bands assigned to the helix and the planar zigzag configurations. Before this, it is necessary to find a configurationally insensitive band which can be used for the normalisation of the spectra. For this, we tested two bands mentioned in the literature as suitable bands, but they were finally found to be inadequate. We found a band which, contrary to the two others, could be used over the whole temperature range under study.

We also studied deuterated sPS. Here no assignment of the infrared bands obtained for the different phases is available. By comparing the spectra obtained for different configurations, we have demonstrated the relationship between certain bands and particular chain configurations. Then, we tried to find the relationship between these bands and those known for the protonated material. We also needed a non configurationally sensitive band for the deuterated material for the normalisation of spectra.

For both the deuterated and the protonated sPS, we started with a sample initially in the δ-phase. The sample was heated at a rate of 10°C/min to a given temperature and then placed in the infrared sample holder at room temperature, and a spectrum was recorded. The sample was then removed and heated to the next temperature. We used the same sample over the whole process. This experimental part was carried out by a project student, Olivier Laveix.

Finally we plotted the integrated intensity of the different bands versus the annealing temperature. These curves were used to determine the transition temperatures of the different samples. This allowed us to determine differences in the thermal behaviour of the two species.

For some phenyl ring modes, we could also find equivalent bands in the spectra of the protonated and deuterated materials. These bands will be useful for the determination of the concentration of isotopic species in blends.

4.6.1. Normalisation

Typical infrared spectra for the different phases are shown in figure 4.15. The choice of the band used for the normalisation of the spectra is a difficult issue. In this study, we used only one sample in order to avoid problems of changing thickness. Nevertheless, the correct procedure is to use an "internal thickness" band, and to determine the ratio of the integrated intensity of the band under study versus that of the band chosen for the normalisation. The transmitted intensity depends on the thickness of the sample. When different samples are used their thickness may vary. Similarly, when a unique sample is annealed, its thickness may change. A band for which the intensity will only vary with the sample thickness (i.e. not sensitive to conformational nor configurational effects) is called an internal thickness band. In previous work, the bands used for the normalisation of spectra were the bands at 1585 [47] and 1183 cm^{-1} [87]. They were used for the normalisation of spectra of samples in the zigzag configuration only. In other works on the
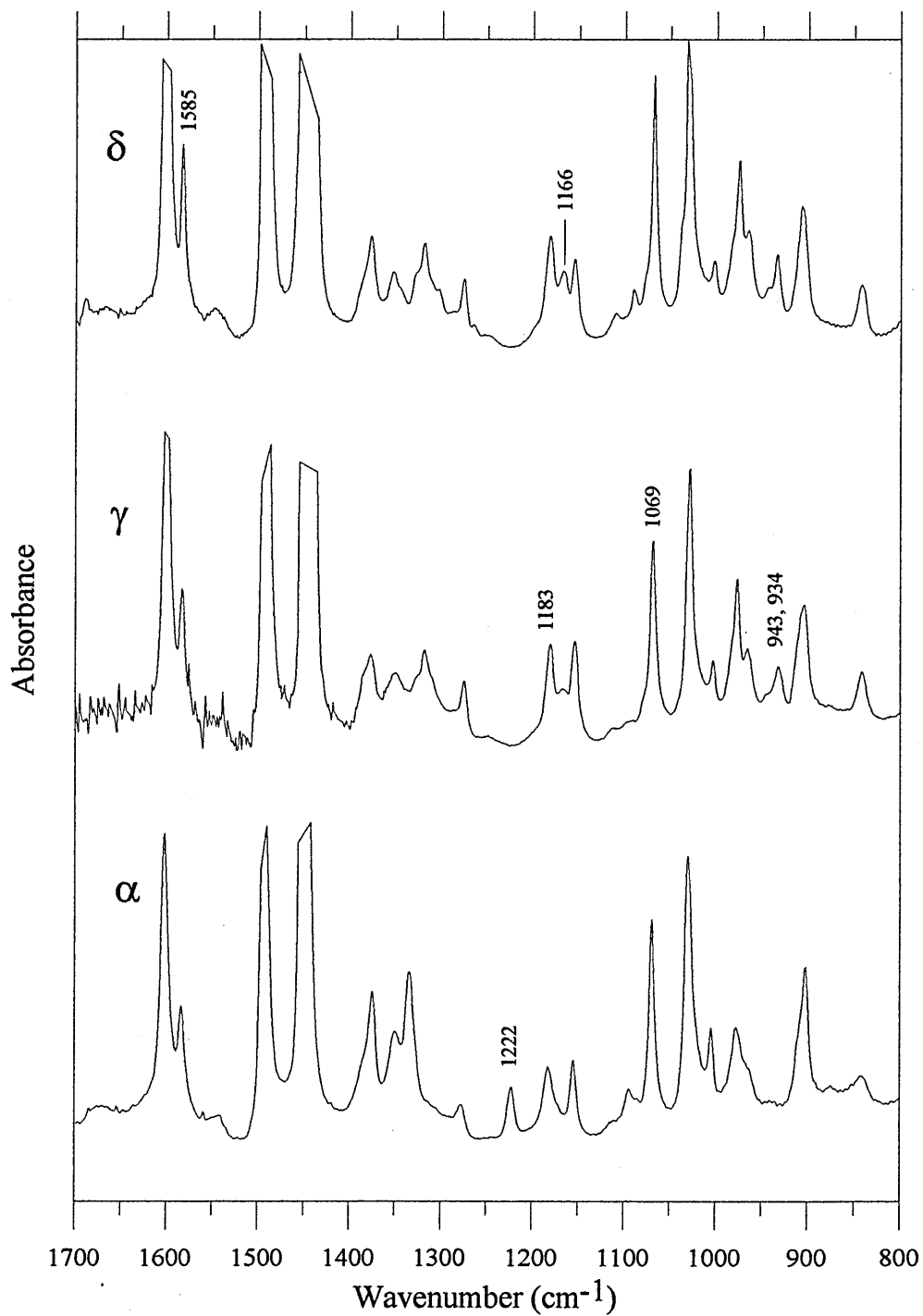
Figure 4.15.

Typical infrared spectra for a protonated sample in the δ-, γ- (annealed at 160°C) and α- (annealed at 200°C) phases.

helical configuration [64, 14], the authors do not give the band they used for the normalisation.

The intensity profile in the 1210-1135 cm^{-1} range was separated into 4 and 3 (above 190°C) components. This was the minimum number of peaks necessary to give a reasonable fit. The integrated intensity of the band at 1183 cm^{-1} was plotted against the annealing temperature (figure 4.16).

According to Nyquist, in the planar zigzag form a band at 1181.48 cm^{-1} is assigned to a ring in plane CCH bending mode, while in the spectrum of the helix form, a band at 1180.8 cm^{-1} is assigned to a mode involving helix backbone deformation. These assignments are confirmed by the evolution of the intensity with temperature, and more precisely by the falloff in intensity at the transition from helical to planar form. Once in the planar form, the intensity remains constant. In conclusion, the band observed at 1183 cm^{-1} cannot be used for the normalisation of the spectra in the whole temperature range.

Two bands assigned to the benzene ring stretching vibrations at 1601 and 1585 cm^{-1} were used by Reynolds et al. [47] for the normalisation of their spectra of samples in the planar zigzag form. The intensity profile in the 1561-1643 cm^{-1} range was separated into 2 components. We present in figure 4.16 the evolution of the intensity of the band at 1585 cm^{-1} with the annealing temperature. As can be seen, there is a large scatter in the data points which seems to be reduced in the planar form. In conclusion, this band cannot be used for the normalisation of the spectra in the whole temperature range. Because of the variability in the absorbance of these bands, we tested a band at 1069 cm^{-1}. As can be seen in figure 4.16, this band seems to be insensitive to the change of configuration from helix

to planar zigzag. This band has been assigned by Nyquist to a ring in-plane C-C-H bending mode for both configurations [69]. While the scatter in data points is small, the intensity of this band shows no sign of the δ to γ transition. It was therefore concluded that this would be a suitable band for the normalisation of spectra.

4.6.2 Configurationally sensitive bands in HsPS

We have separated the initial doublet in the region between 920 and 955 cm^{-1} into two components (figure 4.17). Above 120°C, a third band had to be added (figure 4.18). In each case, the frequencies were allowed to vary with temperature by up to 2 cm^{-1}. The presence of two bands below 120°C and three above was confirmed by the deconvoluted spectra (figure 4.19 and 4.20) and by the second derivatives of the spectra.

The region between 1210 and 1134 cm^{-1} is full of information. After decomposition into different components, there is a band characteristic of the planar configuration (1171 cm^{-1}), in addition to the band at 1183 cm^{-1}, which we have already mentioned in the paragraph about normalisation.

It is worth noting the results of Nakaoki and Kobayashi [64] on films cast from chloroform at room temperature. They studied 5 bands characteristic of the helix configuration. The 571, 548 and 502 cm^{-1} bands showed a decrease of their intensity with decomplexation followed by an increase before the transition from helix to planar zigzag. On the other hand, two bands at 538 and 511 cm^{-1} showed an increase upon decomplexation continuing up to the transition to planar zigzag.

We have similar results for the bands we studied (cf. figure 4.21). The band at 943 cm^{-1} shows a decrease at the δ to γ transition, and a new band at 940 cm^{-1} appears when the intensity of the 943 cm^{-1} band starts decreasing. Both these bands have their intensity falling to zero at the transition to the planar zigzag form. Thus the 940 cm^{-1} band can be called a γ-phase band and the 943 cm^{-1} band a δ-phase band. Presumably, the origin of the bands is the same, but polymer/solvent intercalation leads to a frequency shift in the δ-phase. The sum of the integrated intensities of the 940 and 943 cm^{-1} bands have a behaviour similar to that of the bands studies by Nakaoki : namely an increase following the decrease at the transition temperature. The band at 934 cm^{-1} shows a peculiar behaviour with a minimum occuring before the transition. Although this band is related to the helical configuration, its exact origin is unclear.
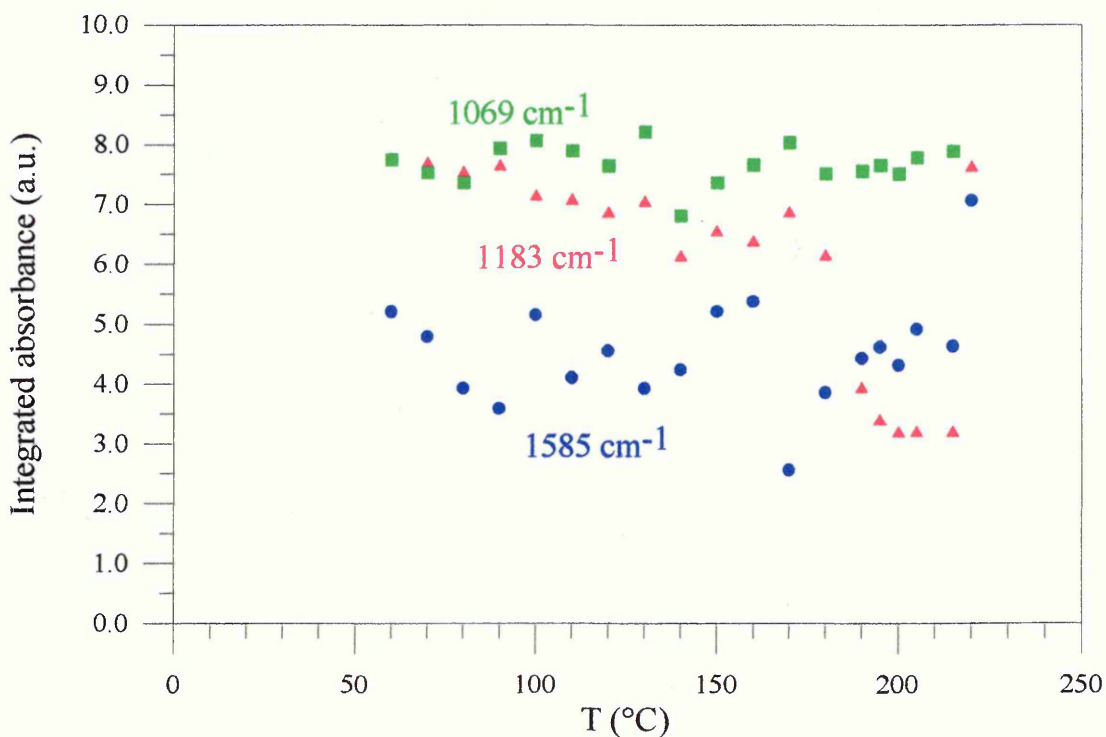
Figure 4.16.

Integrated intensities of the bands used for the normalisation of the spectra in HsPS.
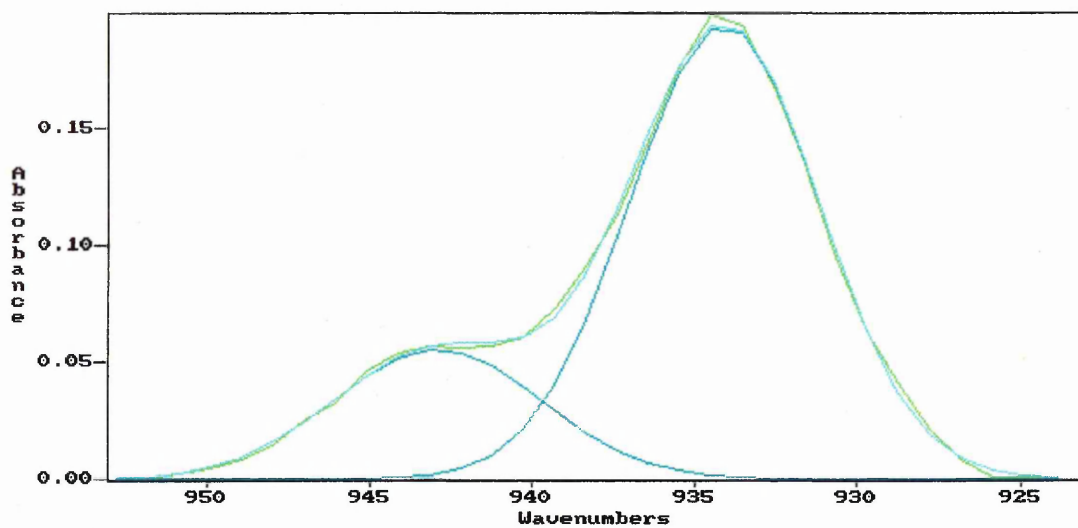
Figure 4.17.

Curve fitting of the region between 920 and 955 cm^{-1} in the spectrum of a protonated sample as crystallized in the δ-phase.
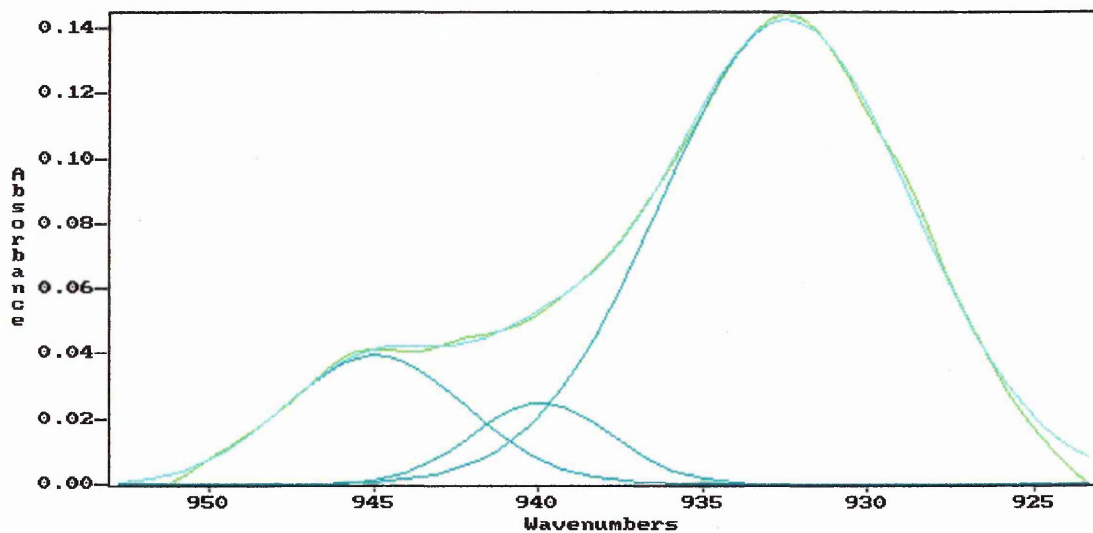
Figure 4.18.

Curve fitting of the region between 920 and 955 cm^{-1} in the spectrum of a protonated sample annealed at 130°C.
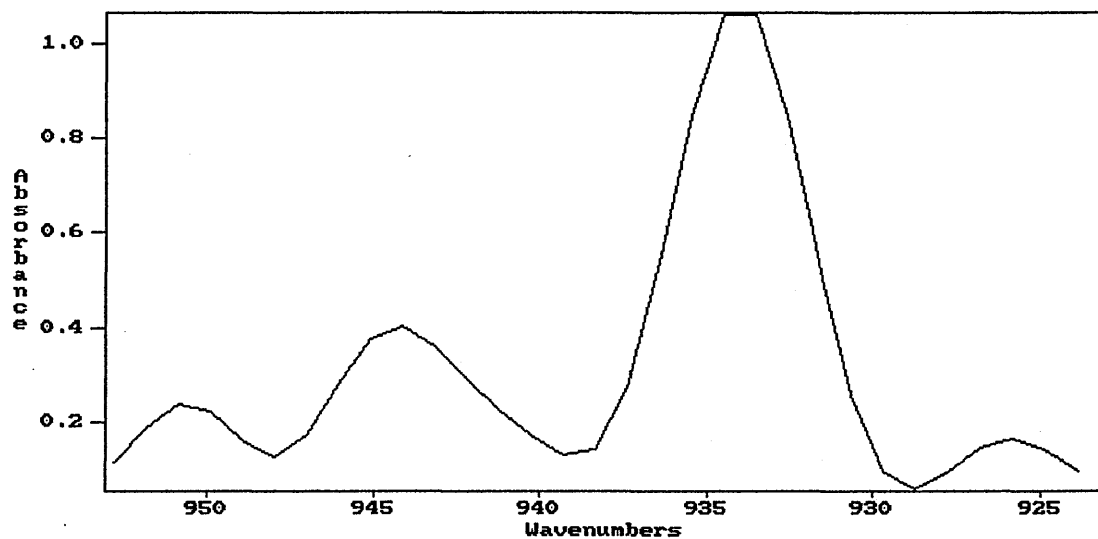
Figure 4.19.

Deconvoluted spectrum of the region between 920-925 cm^{-1} for a protonated

sample as crystallized in the δ-phase.
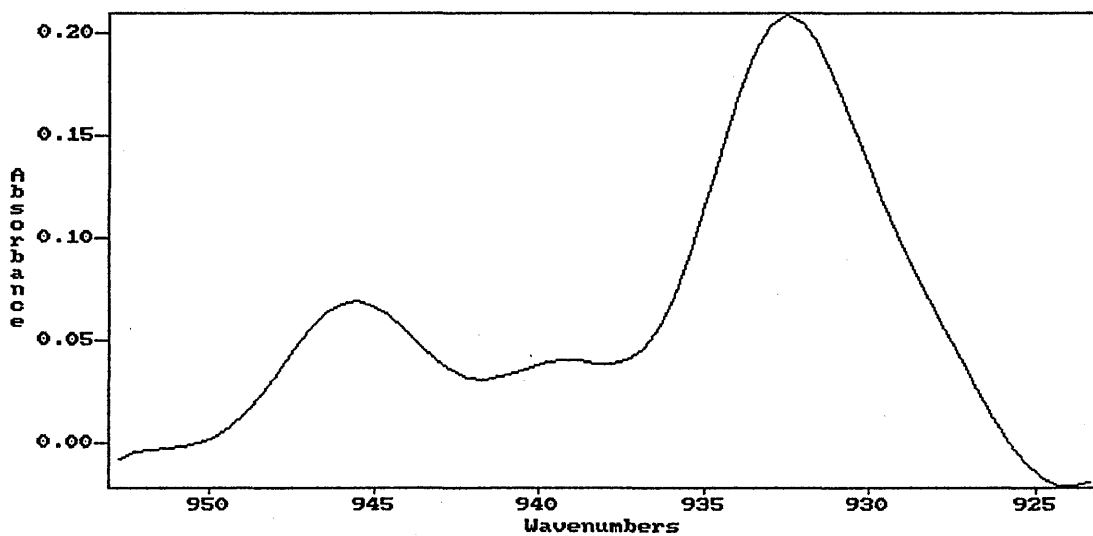
Figure 4.20.

Deconvoluted spectrum of the region between 920-925 cm^{-1} for a protonated

sample annealed at 130°C.
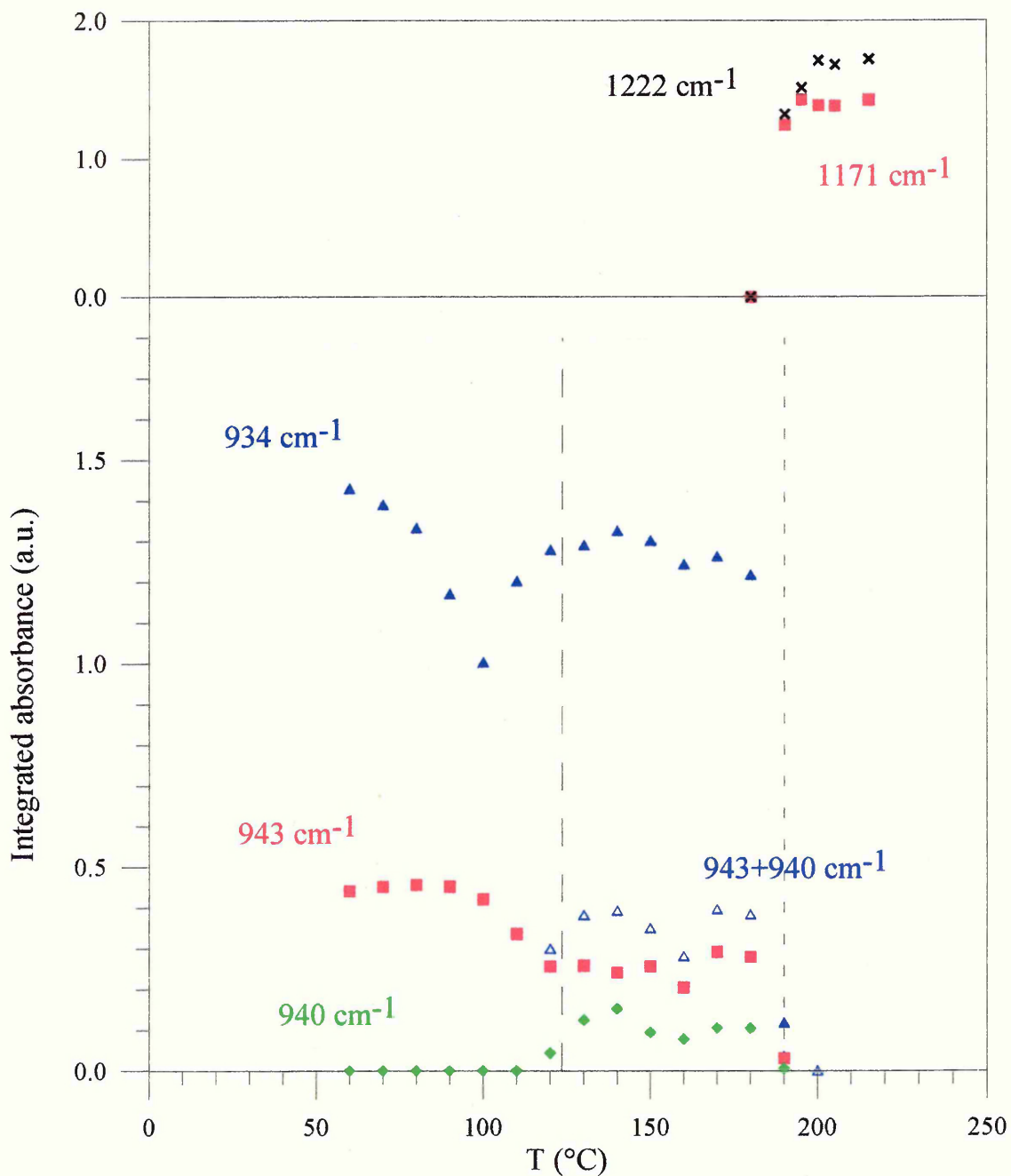
Figure 4.21.

Variation of the integrated intensity of the configurational sensitive bands with annealing temperature for HsPS. These bands were normed using the band at 1069 cm^{-1}.

4.6.3. Deuterated sPS

Typical infrared spectra for the different phases are shown in figure 4.22. By comparing the spectra obtained for each type of configuration, we have identified a set of bands which seem characteristic of the helix configuration at 758.0, 787.8 and 722 cm^{-1} and of the zigzag configuration at 948.0 cm^{-1}. We also selected two bands for the normalisation of the spectra at 1380 cm^{-1} and 1327 cm^{-1} (figure 4.23). We finally chose the latter band because of less scatter, and we carried out a similar study to that done on protonated sPS, by following the evolution of the integrated intensity of these bands with annealing temperature. Results are presented in figure 4.24. In addition, the amount of solvent present in the sample was also monitored. This task is difficult in the case of the protonated material because the bands characteristic of ethylbenzene are generally also present in the spectrum of protonated sPS. By contrast, they can be clearly identified and discriminated in the deuterated material. We chose the bands at 736 and 1473 cm^{-1} as representative of solvent. Results are presented in figure 4.25.

Figure 4.24 shows the temperature variation of integrated absorbance for various configurationally sensitive bands. There is no decrease of the amount of helix material at the transition as was observed for some bands of the protonated material. The behaviour of the intensity of the band at 758 cm^{-1} indicates a correlation with the γ-phase, although its intensity is not zero at temperatures below the transition from the δ- to the γ-phase. Note that the temperature range of existence of the γ-phase seems to be less extended in the case of the deuterated polymer : decomplexation seems to begin at widely differing
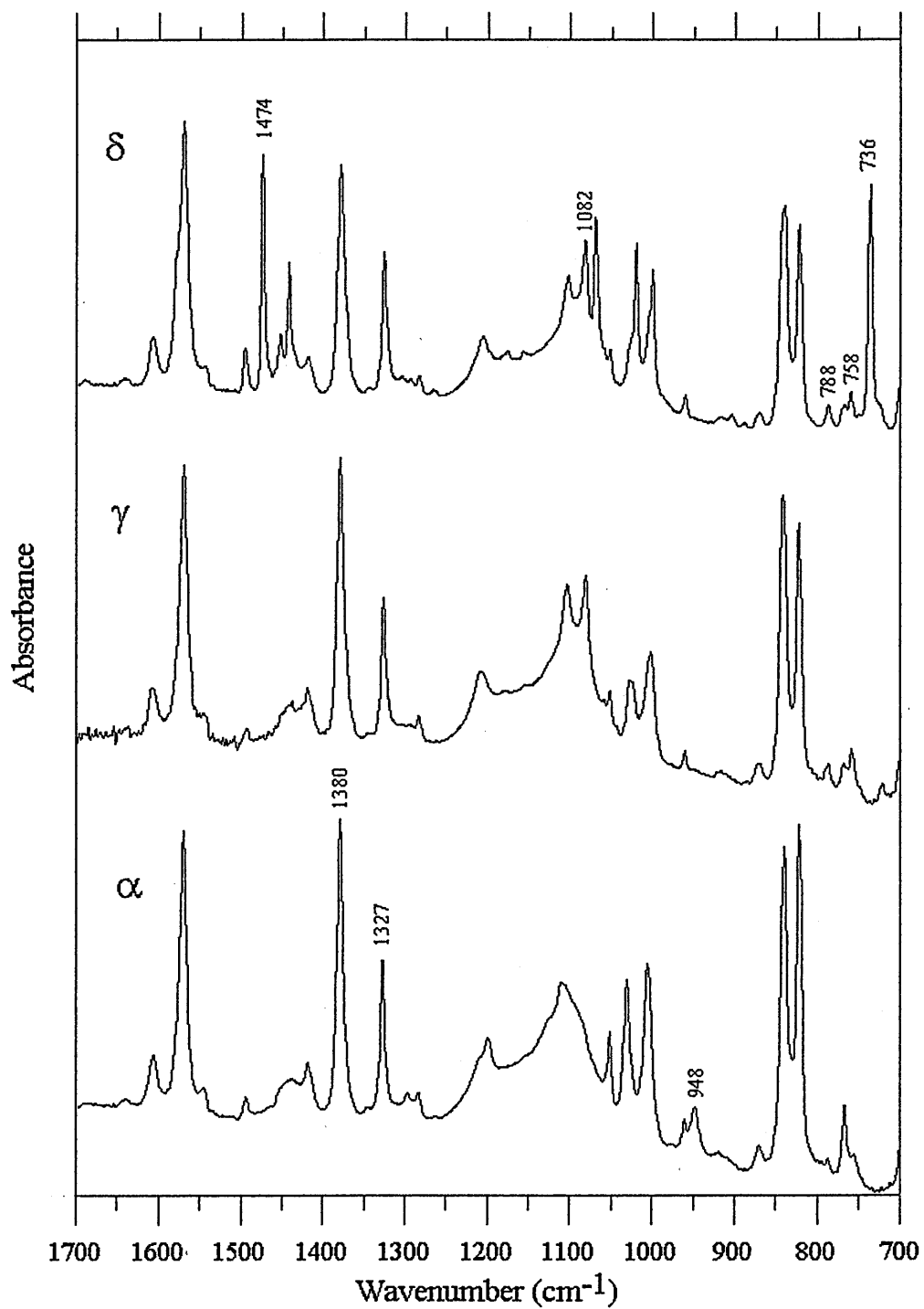
Figure 4.22.

Typical infrared spectra for a deuterated sample in the δ-, γ- (annealed at
180°C) and α- (annealed at 210°C) phases.
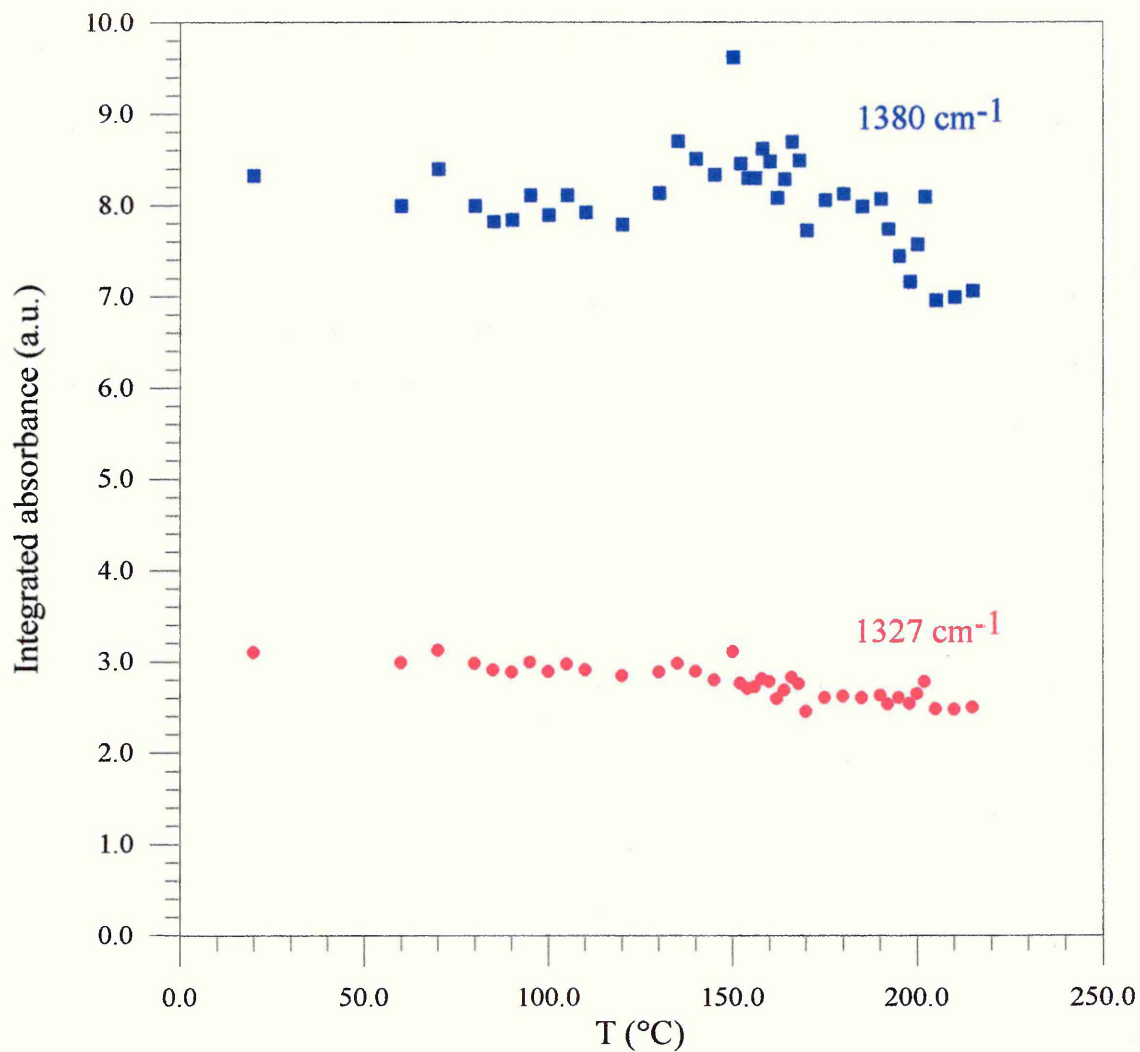
Figure 4.23.

Integrated intensities of the bands used for the normalisation of the spectra in DsPS.

temperatures depending on the type of material involved (cf. figure 4.21). We have not found among the bands studied one for which the behaviour is similar to that the 943 cm^{-1} band in the spectrum of the protonated material. This observation may illustrate the existence of a different polymer/solvent interaction depending on the type of materials.

These results confirm previous DSC measurements and, in the case of the γ to α transition in DsPS, provide information not obtainable from DSC. The temperature at which the bands characteristic of the planar zigzag configuration appear and those characteristic of the helix configuration disappear gives directly the temperature of the transition from γ to α phase. The temperature of transition from δ to γ phase for the protonated sPS is determined using the temperature at which intensity of the infrared band characteristic of δ-phase reaches its minimum value. These values and the transition temperatures as found by DSC are compared in table 4.10. The transition from the δ- to the γ-phase and the melting of the α-phase occur at different temperatures for the two species. The transition from helix to planar zigzag occurs at a similar temperature to within 5°C (the step we used for the heating process in the case of FTIR measurements).

Transition	T HsPS (°C)		T DsPS (°C)	
	DSC	FTIR	DSC	FTIR
δ to γ	123.6	123	142.8	143*
γ to α	193.0	190	?	195
Melting of α	253.3		246.1	

Table 4.10.

Temperatures of transitions from DSC and FTIR for protonated and deuterated sPS. The heating rate was 10°C/min. * temperatures at which the intensities of the solvent bands are half their initial values.

139

4.6.4. Correspondance between the bands in the spectra of D and H sPS

It is possible to find the equivalent of the bands for the protonated material in the spectrum of a deuterated one. In some cases, the shift has been calculated and compared with the experimentally observed shifts of PE.

A particular region of the spectrum (between 2800 and 3100 cm^{-1}) of the protonated material is occupied by ring stretching and bending modes and backbone C-H and C-H$_2$ stretching. Infrared bands are observed at 2906 (K'$_b$), 3001.6 (K'$_a$), 3026.1 (K'$_a$), 3059.9, 3082.1 (K'$_a$) and 3104.3 (K'$_a$) cm^{-1} (see figure 4.26). They correspond to ring C-H stretch (K'$_a$), backbone C-H stretch (K'$_b$) [66]. The expected unlabelled to isotopically labelled frequency ratio for the latter type of vibrations is 1.355 [80]. The bands at 2847 and 2924 cm^{-1} are also assigned to CH$_2$ symetric and assymetric stretch respectively [66, 61]. The ratios of the protonated to the deuterated frequencies for these modes were calculated by Krimm [80] and are 1.379 and 1.349. In general these bands are expected to be found in the equivalent spectrum of the deuterated material in the region between 2090 and 2300 cm^{-1}. An examination of this region confirms the existence of a group of bands for which the shape is similar to that of the initial group of bands. Bands are found at 2099.4, 2126.5, 2193.9, 2236.3, 2273.9, 2288 cm^{-1} (see figure 4.26). The association between some of the bands for the two materials is given in the following table with the corresponding frequency ratios.
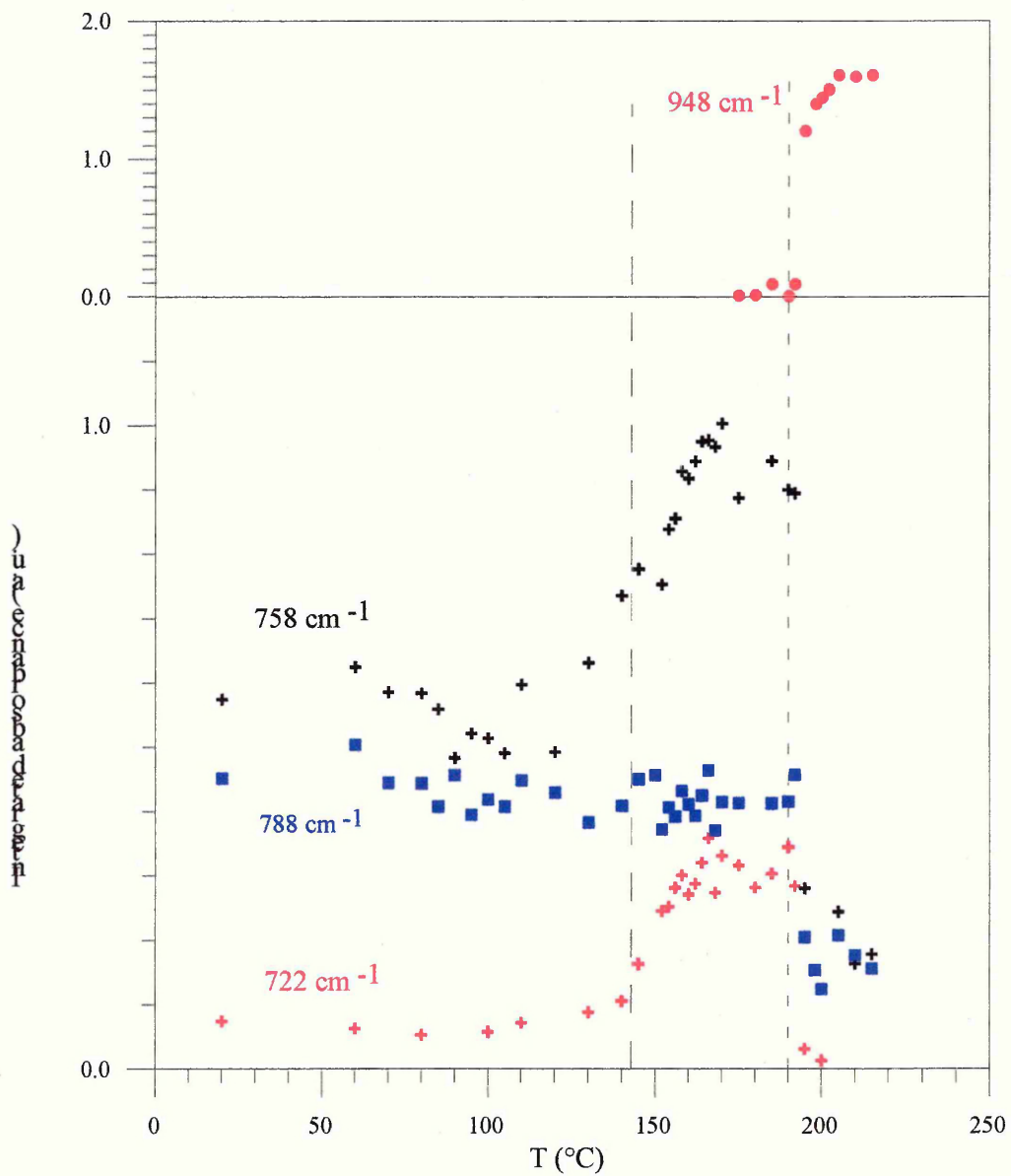
Figure 4.24.

Variation of the integrated intensity of the configurational sensitive bands with annealing temperature for DsPS. These bands were normalised using the band at 1327cm^{-1}.
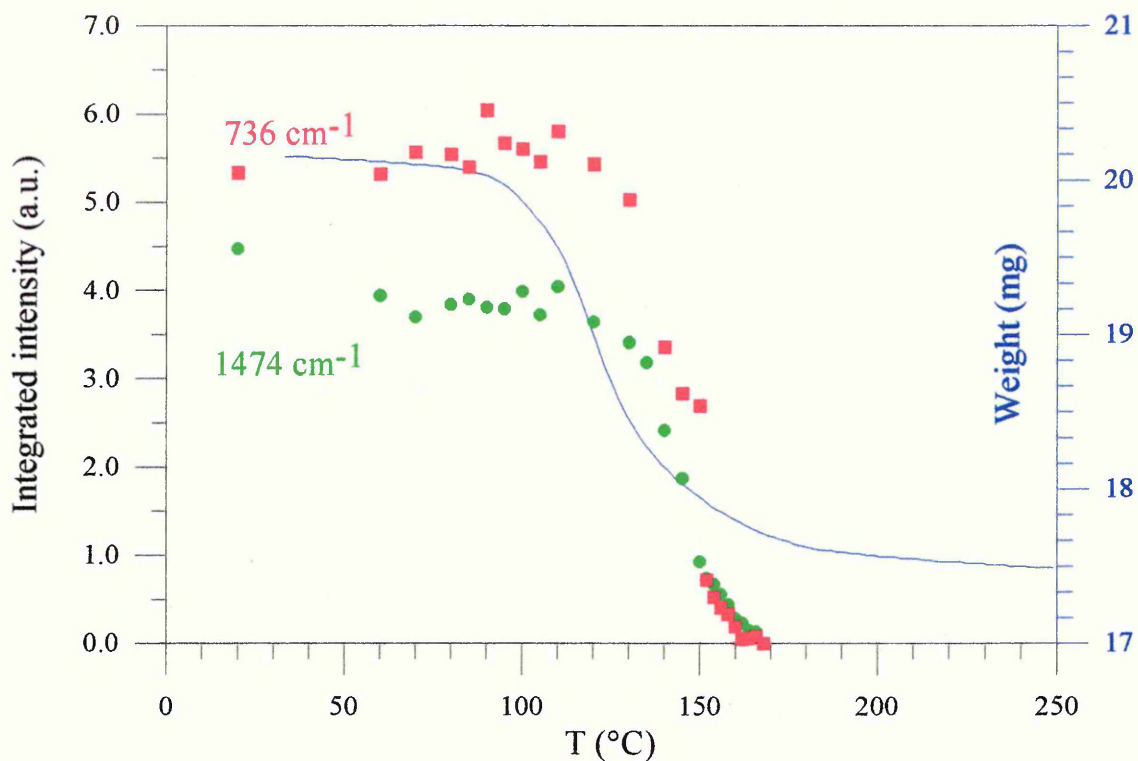
Figure 4.25.

Red squares and green spots : variation of the intensity of two bands assigned to the solvent after normalisation using the band at $1327 cm^{-1}$ in a DsPS/ethylbenzene sample. Blue line : Thermogravimetric measurements on a HsPS/ethylbenzene sample. The heating rate was 10°C/min.

From the calculated ratios for the CH_2 stretch bands, the corresponding bands are expected in the deuterated material at 2065.2 and 2169.0 cm^{-1}. In the deuterated material, the band at the lowest wavenumber is at 2097.7 cm^{-1}, giving a ratio of 1.358. The band in the deuterated material at 2193.7 cm^{-1} could correspond to the other CH_2 stretch band, giving a ratio of 1.334. The ratio for the backbone C-H stretch band (K'_b) is 1.346. These experimental ratios are very close to predicted values.

Assignment	HsPS (cm^{-1})	DsPS (cm^{-1})	Ratio / Deviation %
K$_c$' ($\nu_{sym.}$)	2847.9	2097.7	1.358 (calc. 1.379) -1.5
K'$_b$	2906	2158.6	1.346 (calc. 1.355) -0.7
K$_c$' ($\nu_{assym.}$)	2926.0	2193.7	1.334 (calc. 1.349) -1.1
K$_a$'	3026.9	2272.4	1.332
K$_a$'	3060.2	2287.3	1.338

Table 4.11.

Possible relationship between the infrared bands observed in the protonated and the deuterated samples of sPS. In brackets are the values calculated using the approximate isotope rule [80].

Concerning the configurationally sensitive bands, the band at 722 cm^{-1} in the spectrum of DsPS and the band at 940 cm^{-1} in the spectrum of HsPS have a similar behaviour, and the ratio of their wavenumbers gives 1.30. Similarly, the ratio of the wavenumber of the bands at 948 cm^{-1} for DsPS and 1222 cm^{-1} for HsPS gives 1.29. In both cases, the peaks appear to have the same origin.
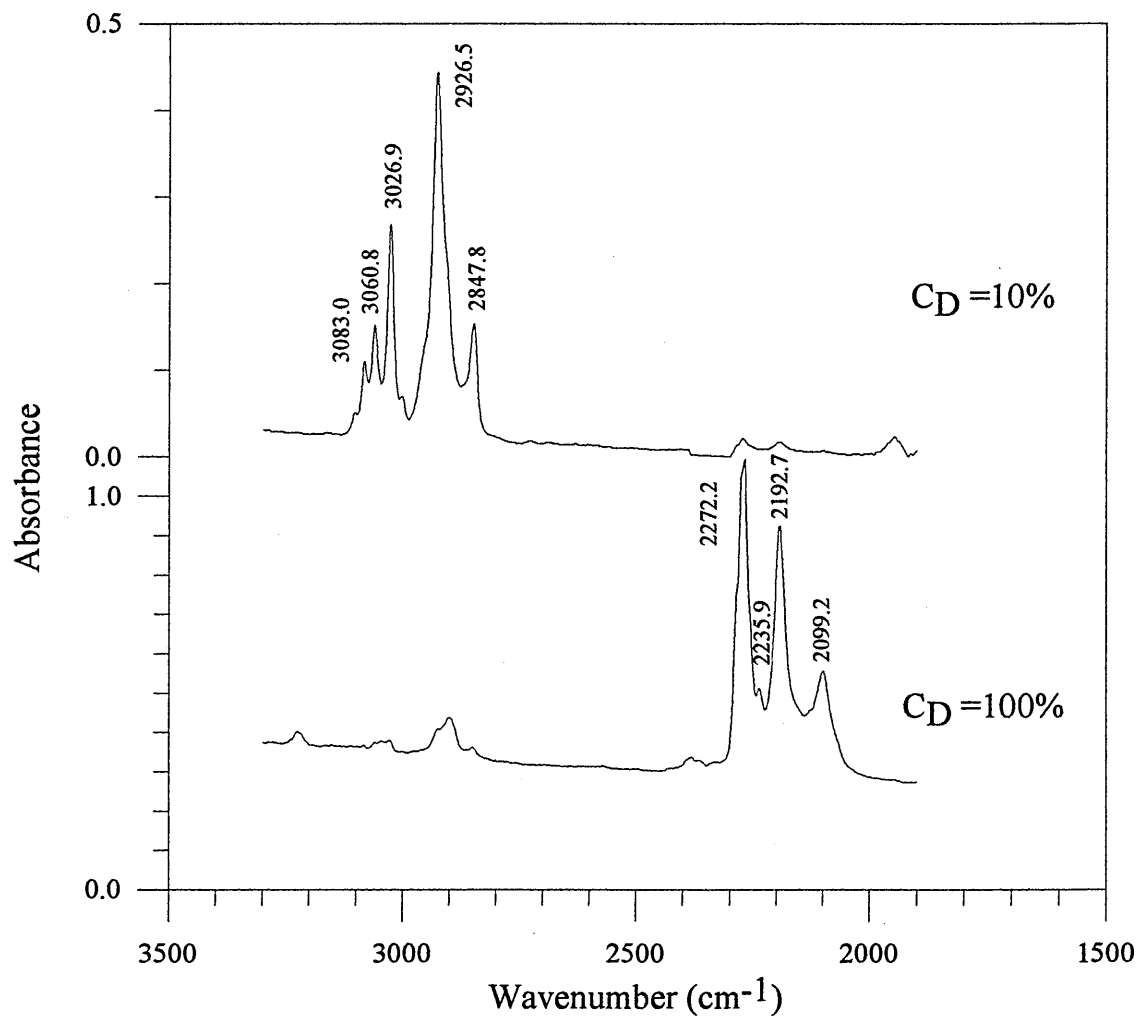
Figure 4.26.

Infrared spectra of 90% protonated and purely deuterated sPS showing the shifts of some bands resulting from deuteration.

Summary

We have shown by means of infrared spectroscopy some differences between the behaviour of the two isotopic species at the transition from the δ to the γ phase. DSC measurements showed that the temperature at which the transition from δ to γ occurs is shifted by 20°C

independantly of the heating rate. This different behaviour is also observed by infrared spectroscopy. In particular, the temperature at which decomplexation starts is rather different: a higher temperature is required before removal of solvent molecules can occur. This indicates that the solvent molecules are more strongly bound in the crystalline structure of the deuterated sPS. This explains why the transition is delayed in the deuterated material: a delay in the start of decomplexation delays the onset of the transition.

On the contrary, the transition from helix to planar zigzag configuration in the case of deuterated material ressembles closely that of the protonated material, while the melting temperature of the α-phase shows a difference of 7°C. One may ask how this will influence the crystallization. From the results we will examine later, and in particular from the concentration of isotopic species in the final sample, and from SANS measurements we can say that there is no measurable isotopic segregation.

From their results Nakaoki et al. [64] concluded that there is a disordering of the helix configuration at the transition. The reasoning is shown to be partially wrong because the different helix bands observed correspond to different type of helices as shown by the existence of solvent free - helix bands in both protonated and deuterated sPS. The decrease of one particular type of helix could be accompanied by an increase of an other type, the overall amount of chains in the helical configuration remaining nearly constant. Note that in the deuterated material, we have not found bands showing a decrease in intensity at the transition from the δ- to the γ-phase.

We will discuss these results again in the next section where we combine SAXS, TGA, DSC and FTIR results.

4.7. Combined study and conclusion

We now need to put together the data we have just presented in this chapter in order to help elucidate the mechanisms involved during the different stages of the annealing of a δ-phase sample. This will allow us to correlate the specific information provided by each of these techniques, namely long period, amount of helical and planar zigzag content, thermal events and solvent content. We have just seen that the transition occurs with some significant modifications in the morphology of the material: decomplexation, thickening and modification of the chain configuration.

Figure 4.27 shows in one diagram the results obtained by DSC, TGA, SAXS and FTIR. From this figure, it is clear that lamellar thickening accompanies decomplexation. With decomplexation, the amount of one type of helical material starts decreasing (infrared band at 943 cm^{-1}), while another type of helix appears (infrared band at 940 cm^{-1}). We do not know the exact origin of these two bands, but the band at 940 cm^{-1} is obviously related to the existence of the γ-phase and the band at 943 cm^{-1} to the solvated helix. The total amount of helical material can be obtained by summing the intensity of the two bands and this decreases with decomplexation. Thus, there is a loss in helix content at the transition, and consequently there is no overall increase in the helical content upon transition from the

δ- to the γ-phases. In consequence, crystal thickening cannot be explained by crystallization of amorphous material as this would require an increase of the amount of material in helical configuration. Therefore, another mechanism has to be envisaged which will allow thickening to occur without increasing the amount of helical material. Crystal thickening during annealing is a well known general phenomenon of crystalline polymers, but it usually happens within ~30°C of the melting temperature. The mechanism of sliding diffusion has been suggested for PE specifically [35].

From the correlation between weight loss and long period measurements, it is clear that the expulsion of solvent facilitates this sliding of the macromolecules. We suggest that solvent removal is responsible for an increase of the longitudinal and, as will be seen, also lateral chain mobility. The latter process accompanies the shrinkage of the b dimension of the crystal lattice. It is worth mentioning that lamellar thickening has been observed for nylon-6,6 crystals annealed in suspension [88]. This type of thickening has to be related to the ablility of the nylon crystal lattice to interact with solvents. In this sense, the behaviour observed for sPS at the δ to γ transition ressembles that of nylon.

Concerning the γ- to α- phase transition, it is clear that the thickening observed at this transition temperature is related to the appearance of the planar zigzag configuration. This transition is not obvious on the DSC trace although clear from infrared data. We have already explained the reasons why thickening is expected at this transition: the change from helical to planar zigzag implies an extension of the chain in addition to the expected thickening usually observed before the melting temperature is reached.
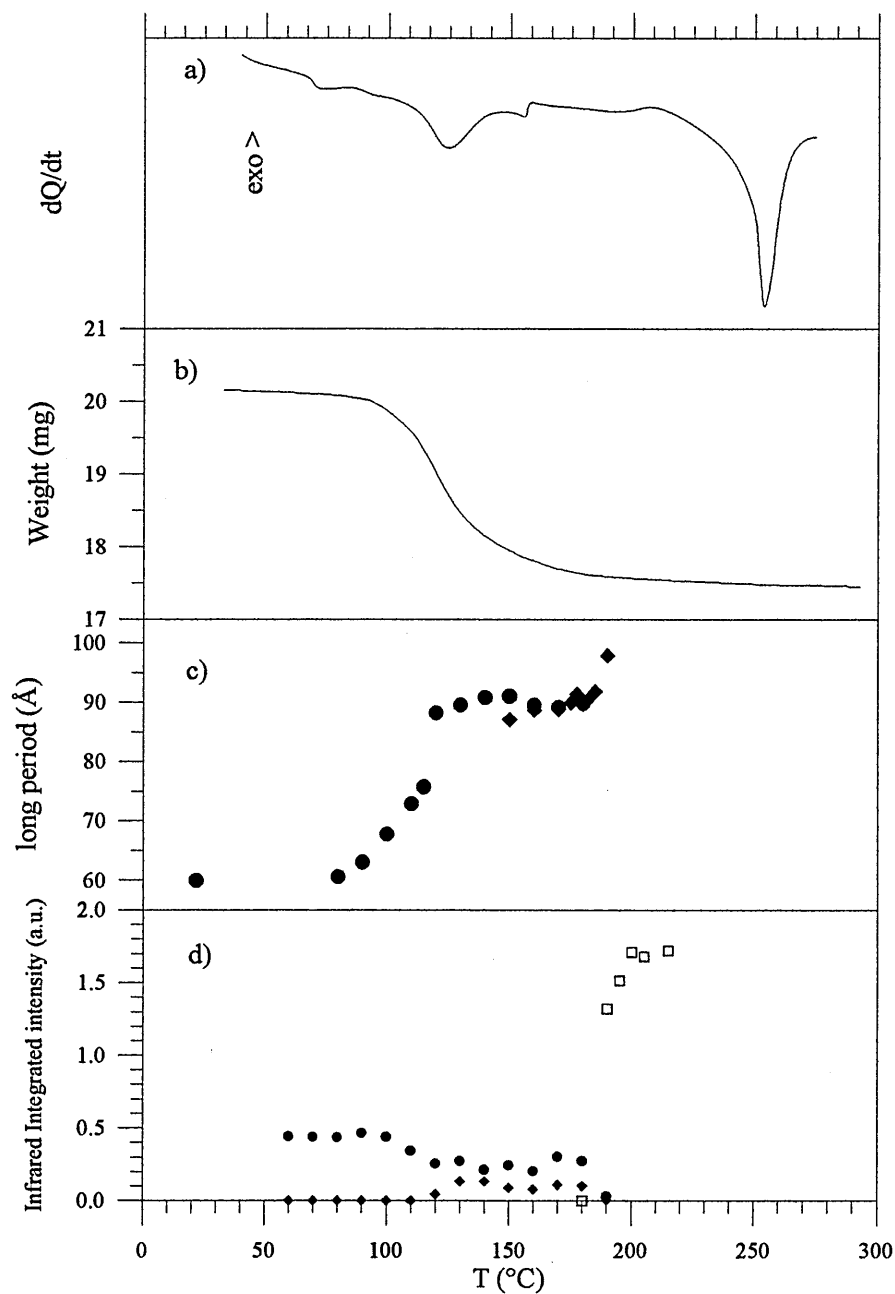
Figure 4.27.

a) DSC and b) TGA plots for a sample initially in the δ-phase. c) long period versus annealing temperature for the solution-crystallized mats, ● annealing time 15 s, ◆ annealing time 30 min   d) Integrated intensity of the configurationally sensitive infra-red bands, ● band at 943 cm^{-1} (helix), ◆ band at 940 cm^{-1} (helix without solvent), □ band at 1222 cm^{-1} (planar zigzag). In all cases the heating rate was 10°Cmin^{-1}.

Chapter 5

Neutron Scattering Results

Introduction

In this chapter, we present a neutron scattering study of molecular conformations in sPS. The first section concerns preliminary small angle neutron scattering (SANS) measurements of molecular dimensions in the δ- and γ-phases. In the second section, we use the statistical model we presented in chapter 3 to simulate sheet-like arrangements of labelled stems. The scattered intensity from such arrangements is calculated and compared with experimental IANS data. In the case of sPS, the fold plane is not known with any certainty. The presence or absence of diffraction peaks related to the fold direction was used to clarify the situation. The model simulations allow the best fit to experimental data to be obtained, and parameters such as the probability of adjacency can be evaluated. An important constraint in the fitting process is the in-plane radius of gyration: values obtained from the simulations must be consistent with experimental results from SANS. The

combined quality of fit of scattering intensities and radius of gyration values is therefore a further test for the sheet-like model.

5.1. Small angle neutron scattering

Experimental

Small Angle Neutron Scattering (SANS) measurements were made using LOQ at the ISIS neutron source (Chilton, England). The available range of momentum transfer q was from 9×10^{-3} to 2.5×10^{-1} Å^{-1}. The γ-phase samples used for neutron scattering were obtained by heating the sample previously in the δ-phase for 5 hours at 135°C. WAXS confirmed that the γ-phase was attained after this heat treatment.

The samples were in the form of 100 mm^2 square sheets, with typically 15 sheets stacked together and wrapped in aluminium foil. They consisted of a mixture of C_D=5% (w/w) of deuterated sPS in a matrix of protonated sPS. As a consequence of sample availability, two series of samples were prepared differing in the protonated matrix. The characteristics of these samples are summarized in table 5.1.

It was not possible to match the molecular weight of the protonated and deuterated molecules in order to give identical melting temperatures. This difference and the resulting fractional crystallization may give rise to (i) isotopic fractionation ("segregation") and (ii)

Matrix	Sample	DsPS conc. C_D (%) Initial	DsPS conc. C_D (%) Final	Initial molecular weight of DsPS ($\times 10^{-3}$ $\overline{M}_w$)	$\overline{M}_w / \overline{M}_n$	Initial molecular weight of HsPS ($\times 10^{-3}$ $\overline{M}_w$)	$\overline{M}_w / \overline{M}_n$
AH	AD		4.6	42.7	3.6	85.4	5.0
	BD		5.9	124.5	3.0		
	CD		5.2	144.5	2.4		
BH	AD	5	4.9	42.7	3.6	55.7	3.2
	BD		6.1	124.5	3.0		
	CD		7.6	144.5	2.4		
	DD		7.7	124.0	2.8		

Table 5.1.

Characteristics of the samples used for neutron scattering experiments: molecular weights and polydispersities of the protonated and deuterated polymer as measured by GPC, and concentration of deuterated species after crystallization as measured by FTIR.

molecular weight fractionation. The first of these effects can be detected using an extrapolation to zero angle from SANS data. The second may give rise to label concentrations C_D which differ from their initial values (5%). In order to verify this, and to carry out the blank subtractions, real isotopic concentrations need to be known. We used infrared spectroscopy, with two standard samples of known isotopic concentration. For this purpose, mixtures of isotopic species were weighed and dissolved in toluene before casting onto KBr plates which were then heated for half an hour at 130°C in order to remove the solvent bands. Nyquist et al. [69] have assigned the 2849 cm^{-1} band to backbone C-H stretching modes ($\nu_{sym.}CH_2$). Similarly, we have assigned the 2193 cm^{-1} band to backbone C-D stretching ($\nu_{asym.}CD_2$).

For two samples of known concentration (5 and 10%), the ratio of the integrated intensity of these two bands was calculated, and plotted versus $C_D/(1-C_D)$ to obtain a calibration curve (figure 5.1). Then for blend samples the ratio was measured, and the corresponding concentrations were calculated using the calibration curve. These results (see table 5.1) show a small amount of fractionation by molecular weight.
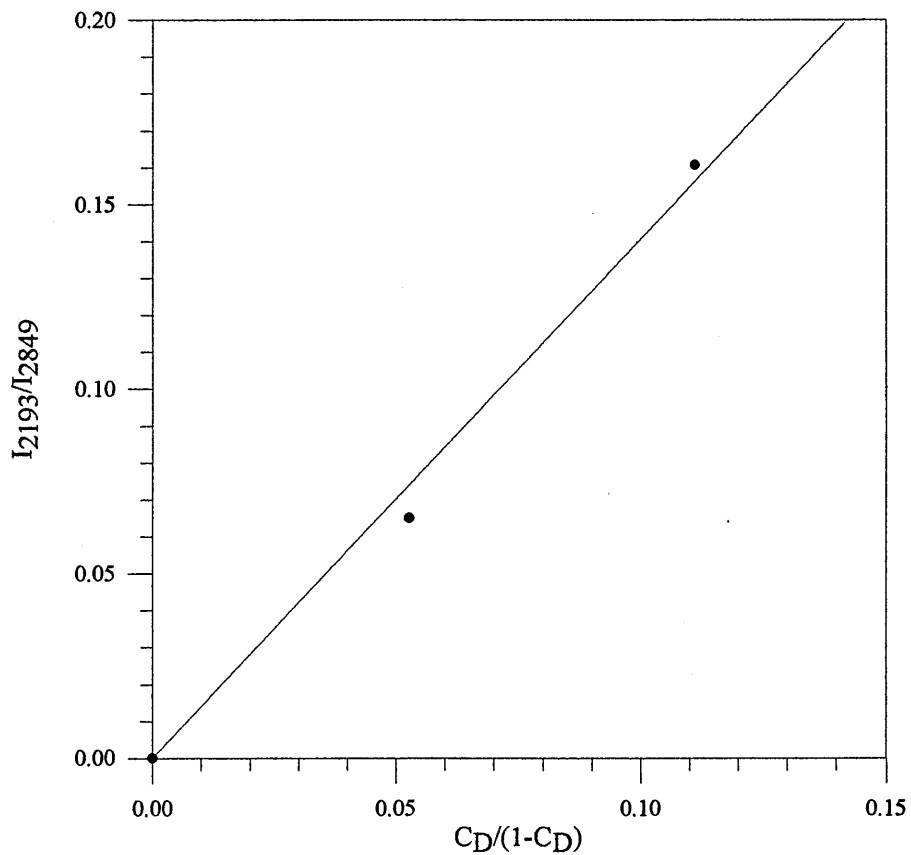

Figure 5.1.

Calibration curve used for the determination of the concentration in isotopic species.

Results

In the Guinier range, $\overline{M}_W$ and the in-plane radius of gyration R_g of the oriented mat were

determined, using Zimm plots (1/I(q) vs. q^2), from the extrapolated intercept at q=0 and the

slope at small q respectively (cf. equation 3.45). Figure 5.2 and 5.3 show two typical

sample Zimm plots for the δ and γ phases with the extrapolation to zero angle. The very

small excess intensity for the δ phase sample at smallest angles indicates negligible

isotopic fractionation.

Sample/Matrix	δ		γ	
	$\overline{M}_W$	Rg (Å)	$\overline{M}_W$	Rg (Å)
AD/AH	20000	45.1 ± 0.4	21000	52.0 ± 0.5
BD/AH	44000	79 ± 2	55000	97 ± 2
CD/AH	32000	68.6 ± 0.7	40000	81 ± 1
AD/BH	21000	51.6 ± 0.5		
BD/BH	32000	72 ± 2		
DD/BH	48000	60.8 ± 1.0	77000	85 ± 1

Table 5.2.

Molecular weights and radii of gyration as measured by SANS.

Measured molecular weights are somewhat lower of a factor of about 3 in comparison to

GPC values. Such a feature, although to a lesser extent, has been reported by Sadler for

polyethylene with high molecular weight [37]. So far, no explanation has been put forward

for this discrepency between molecular weight values measured by NS and GPC.
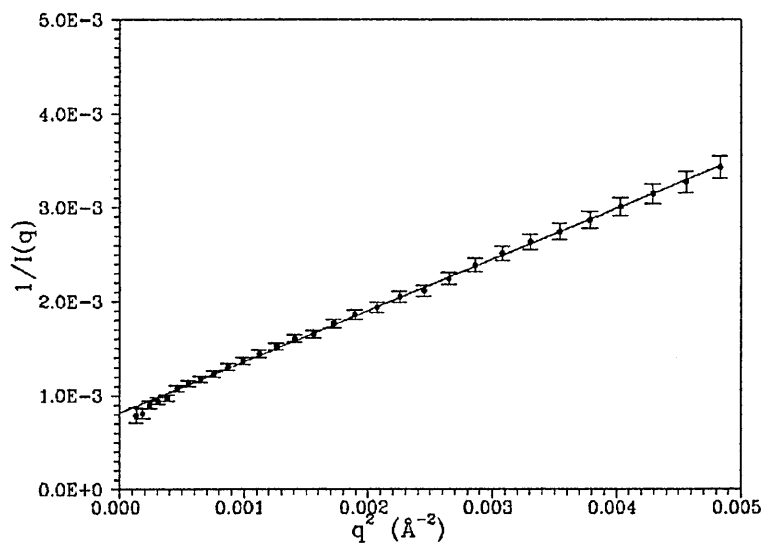
Figure 5.2.

Typical Zimm plots for the δ phase ($\overline{M}_w$=42700). Data obtained using the LOQ instrument at ISIS.
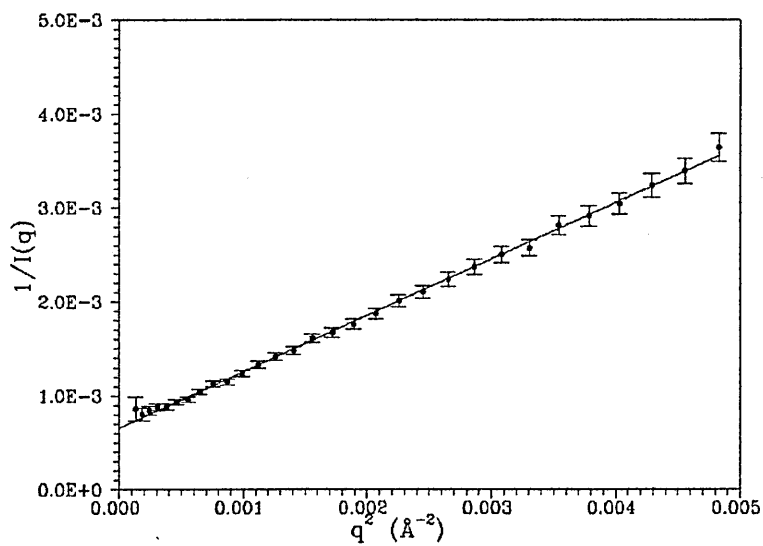
Figure 5.3.

Typical Zimm plots for the γ-phase ($\overline{M}_w$=42700). Data obtained using the LOQ instrument at ISIS.

154

Molecular weight distributions here are somewhat broader, which may partially explain this observation.

In figure 5.4 and 5.5, the radius of gyration is plotted against the molecular weight. It can be seen that there is a small change in R_g with increasing molecular weight. We calculated by means of a least-squares fit the exponent α in the relationship $R_g \propto M^\alpha$ and obtained values of 0.31 ± 0.6 and 0.41 ± 0.09 for the δ and γ phases respectively. The expected value for a random coil or an uncorrelated array of stems is 0.5. For polyethylene crystallised from the solution, this exponent was found to be 0.1 [6]. This result was explained by the "superfolded sheet" model, whereby sheets of stems along the preferred crystallographic fold direction are folded back to form a stack of sheets. The value we found may represent an average of the values corresponding to two types of chain conformation: the single sheet structure (for lowest molecular weight $\alpha \rightarrow 1$) and the multiple sheet structure (highest molecular weights $\alpha \rightarrow 0.1$). Thus the data obtained within this molecular weight range are consistent with a transition from the single sheet to the multiple sheet structure. Further support for this model will be shown from IANS data.

In order to illustrate this change of regime, we calculated the in-plane radius of gyration for N_r stems in one sheet in the case of purely adjacent folding [89]:

$$R_g^2 = \frac{N_r^2}{12} I_{//}^2 \tag{5.1}$$

where $N_r = \dfrac{M_w}{M_r}$. We assume here that the sample is fully crystalline and that chain folds form a negligible fraction of the molecular length. M_r is the molecular weight of the stem deduced from the thickness of the monocrystal. When superfolding occurs, the molecule
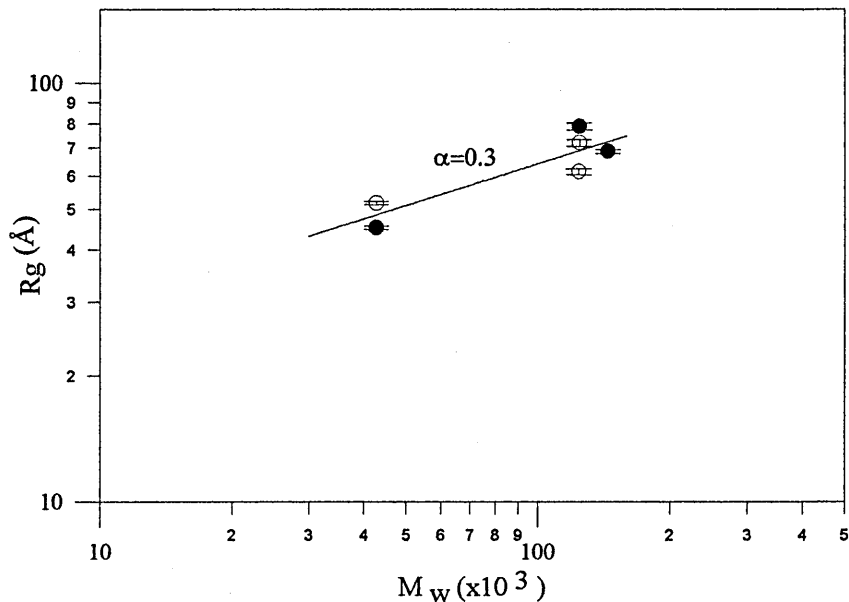
Figure 5.4.

Radius of gyration versus molecular weight (GPC) for the δ-phase samples of sPS presented on a log/log plot and corresponding power fits. ● sample in δ-phase with AH matrix, and O BH matrix.


Figure 5.5.

Radius of gyration versus molecular weight (GPC) for the γ-phase samples of sPS presented on a log/log plot and corresponding power fits. ■ sample in γ-phase with AH matrix, and □ BH matrix.

folds in N_S sheets, each of them containing $N_{r/s}$ stems. In the case where the stems are placed on a rectangular lattice, R_g can be written

$$R_g^2 = \frac{N_{r/s}^2}{12}I_{//}^2 + \frac{N_s^2}{12}I_\perp^2 \qquad (5.2)$$

$I_{//}$ and $I_\perp$ are respectively the fold and superfold lengths. We have made the assumption here that $I_{//}$ and $I_\perp$ are large in comparison to the stem width. Chatani et al. [10] have suggested that folding occurs along the direction a, and we will confirm this result in the following section. In order to take account for the dilution of stems, instead of $I_{//}$ we use d, the average distance between two consecutive stems in a sheet [see section 5.2]. Lines representing equations (5.1) and (5.2) are plotted in figure 5.6 for a fixed number of stems per sheet equal to 12, together with the fit obtained from the experimental data for the δ phase. This figure illustrates how a change of regime within the molecular weight range used as described above would be consistent with the measured values for the radius of gyration and the calculated exponent.

In the γ phase, an increase in R_g is obtained (table 5.2). It should be noted that measurements of the X-ray long period show an increase on transformation to the γ phase, while there is no indication of any loss of crystal orientation. The fact that R_g increases at the δ to γ transition has implications for the mechanism of thickening discussed earlier : the chain reorganisation must occur on a local level, rather than on a molecular scale because in the latter case, a decrease in R_g would be expected. This proposal is reminiscent of the solid state diffusion proposed for polyethylene single crystals at low heating rates [35]. The magnitude of the increase in R_g suggests significant movement of stems upon transition.

This is further suported by the increase in the α exponent indicating a more random distribution of the stems (cf. $\alpha=0.5$ for an uncorrelated array of stems). For a simple model where stems are allowed to move only in a direction perpendicular to the sheet plane, the relation between the radius of gyration before and after displacement is:

$$R_g^{\gamma^2} = R_g^{\delta^2} + <\delta_{\perp}^2> \qquad (5.3)$$

where $<\delta_{\perp}^2> = \dfrac{1}{N_r} \displaystyle\sum_{i=1}^{N_r} \delta_i^2$, and δ_i is the displacement length of the stem i.

If we apply this formula to our experimental data we find that the root mean square of the displacement length ranges from 25 to 60Å depending on the molecular weight. This demonstrates the mobility of stems, arising from the expulsion of solvent molecules which form part of the δ phase polymer/solvent complex. Again, this mobility is likely to be facilitated by significant numbers of crystal defects in the transition region. A molten zone of a size at least equal to molecular dimensions would give rise to fractionation of isotopic species. This is not observed, as the Zimm plots for the γ phase samples do not show any excess intensity at small q (see figure 5.3). Similarly, the low angle intercepts are of very similar magnitudes, suggesting minimal isotopic fractionation. Thus, the regions of enhanced mobility are smaller than molecular dimensions.

Summary

SANS measurements on the δ phase complex are characterised by negligible isotopic fractionation, but significant fractionation by molecular weight. In-plane radius of gyration data for oriented mats show only a small increase with increasing molecular weight. The interpretation is that the structure closely resembles those already determined for non-complexing polymer/solvent systems after crystallisation from dilute solution, namely a sheetlike structure, with crystal stems arranged in a preferred crystallographic direction.
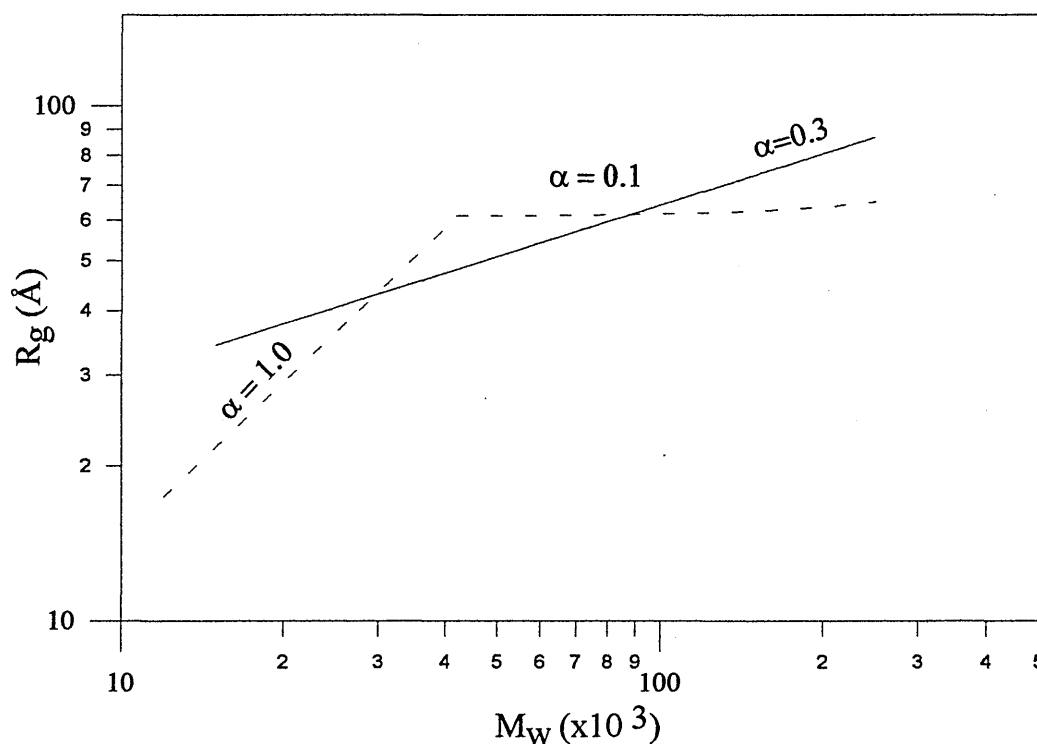

Figure 5.6.

Radius of gyration versus molecular weight as calculated using equations (5.1) and (5.2) (- - - -) presented with the power fit obtained for the δ-phase (————).

We will demonstrate in the next section that this direction is the $\underline{a}$ direction. Furthermore, superfolding (characterised by parallel sheets of stems) occurs, as in single crystal mats of polyethylene [7] and isotactic polystyrene [9]. This is, to our knowledge, the first time that such a structure has been observed in a polymer/solvent complex. The detailed arrangement of labelled stems within the sheets will be analyzed in the next section.

An increase in the radius of gyration with decomplexation and formation of the γ phase is interpreted as evidence of the movement of crystal stems from the δ phase sheets. A simple calculation shows this displacement to be of the order of 25 to 60 Å, depending on molecular weight. The formation of the γ phase structure through the existence of zones of mobile material suggests that these zones are considerably smaller than individual molecules, since there is no evidence of enhanced isotopic fractionation.

5.2. Wide angle neutron scattering

5.2.1 Experimental

WANS experiments were performed at the Institut Laue-Langevin (ILL, Grenoble, France), with the D17 instrument. In order to cover a wide momentum transfer range, two sets of experiments were carried out. The first involved the normal to the detector on the axis of the incident beam, while in the second case the normal was at an angle of 35° to this axis. For the latter, the multiple sample holder was rotated, as appropriate to the geometry. Two ranges were then available: the small angle region (from 3.6×10^{-2} to 2.5×10^{-1} Å^{-1}) and the intermediate angle region (from 1.9×10^{-1} to 6.7×10^{-1} Å^{-1}). A mechanical wavelength selector was used, which provides a spectrum characterized by a relative width at half-height of $\Delta\lambda/\lambda=10\%$. All the data were normalized with an incoherent scatterer and corrected for transmission and thickness. The excess intensity scattered by the labelled chains was obtained after subtracting the signal from a sample containing protonated chains only, crystallized under the same conditions. In the intermediate angle range, we face two problems with the data analysis, namely the intrinsically small diffuse scattered intensity and the large incoherent signal from the unlabelled polymer. To demonstrate the latter point, we considered a plot of the measured intensity versus transmission (figure 5.7). This will be linear for incoherent scatterers. Inclusion of samples, as well as unlabelled "blanks" showed good agreement with the linear plot, confirming the predominance of incoherent scattering. The procedure adopted, on the basis of this result, was to scale the

"blank" scattering so as to reduce the sample scattered intensity to zero in the vicinity of

$q=0.60$ Å^{-1}. A similar procedure has been used previously in the case of polyethylene [82], and was shown to be a satisfactory method of data analysis.
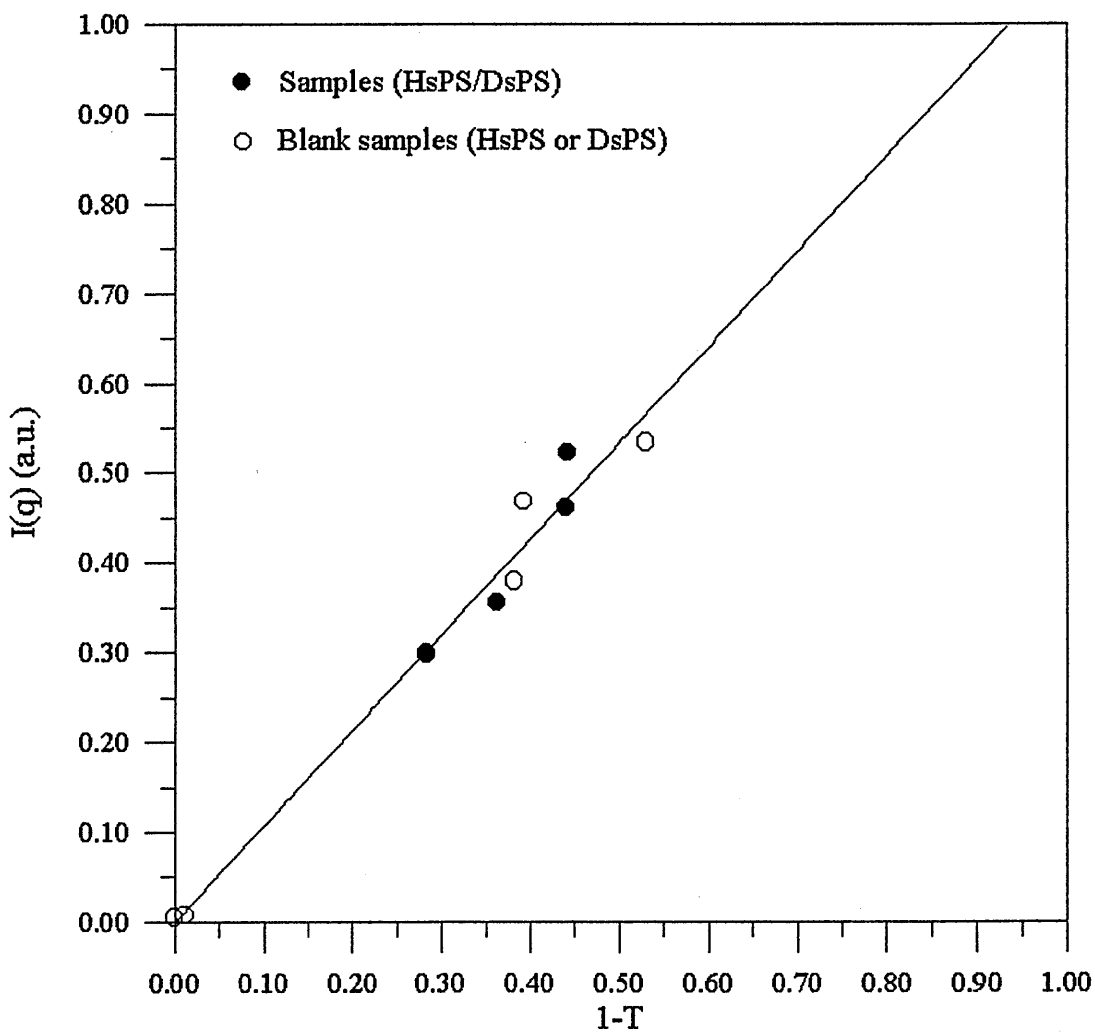

Figure 5.7.

Transmitted intensity versus (1-T) for blend and blank samples as measured by the D17 detector at ILL.

162

5.2.2. Effects of crystallinity and orientation

Amorphous samples of sPS with various concentrations in deuterated molecules have previously been studied by SANS, over the range 0 to 0.5 Å^{-1} [30]. They showed intensities smaller by a factor of about 10 in comparison to intensities measured for semi-crystalline samples and presented in this paper. Thus the amorphous material produces very small scattering over the wave vector range used. Crystallinity for samples crystallised under various conditions is found to range from 40% to 74% [14, 35, 36, 67].

The scattering from the stems is only significant when the wavevector q is perpendicular to the chain axis (the c-direction). From equation (3.7.) there is a difference of phase $q.r_{ij}$ between the wave scattered by two nuclei separated in space by the distance r_{ij}. The total scattered amplitude is maximum when this phase difference is zero. For a stem, r_{ij} is parallel to the stem axis, and $q.r_{ij}=0$ when $q \perp r_{ij}$. In our case the stem axis is the chain axis. Hence, with the usual experimental situation of the normal to the mat along the beam direction, the intensity is enhanced above that expected for isotropic samples. Since the formulae used for calculating the intensity are derived for isotropic systems, we must evaluate the enhancement factor E of the intensity due to the orientation of the crystallites within the mats. This is illustrated in figure 5.8, where a comparison of the intensity for oriented and isotropic samples is made. The latter sample was obtained by chopping the former into very small pieces. It is very difficult to ensure that there is a random distribution of the orientation of these pieces, and some preference for the original orientation is likely to remain. The ratio of intensities of oriented to unoriented samples

must be regarded as a minimum value. In this case, the ratio of the two intensities gave a value of 1.06 at widest angles.

On this basis, we consider that the combined effects of crystallinity and orientation on the scattered intensity justify a direct comparison between calculated and experimental intensities, with a scaling factor of 2 applied to the latter values.
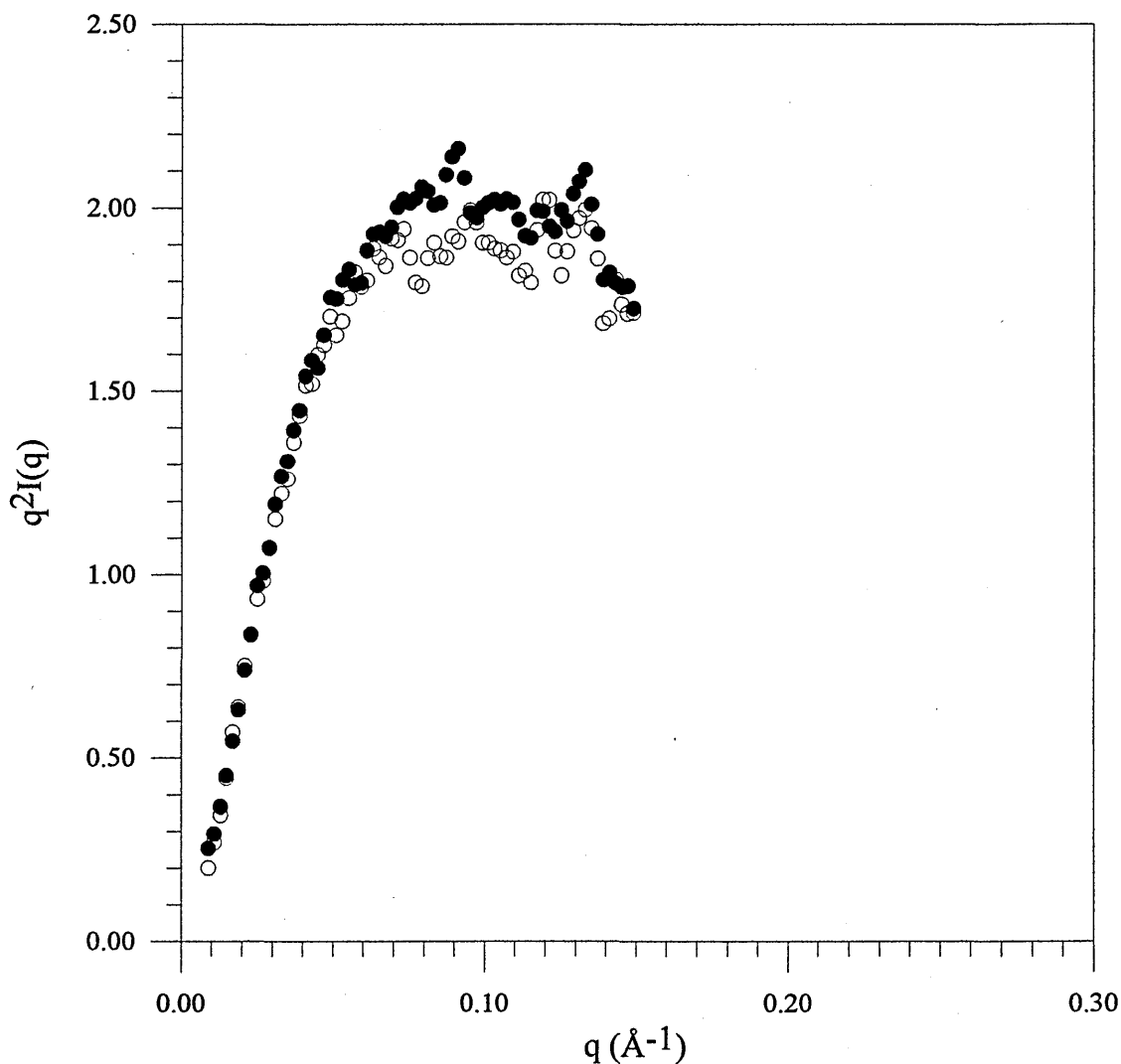
Figure 5.8.

SANS results for sample AD (M_w=42700) in the γ phase. ● oriented mat and O isotropic sample obtained by chopping the former into very small pieces.

5.2.3. The problem of the fold direction

In applying the model to sPS/ethylbenzene, we are faced with a problem in that the fold direction for the crystals is not already known with any confidence. Although the neutron scattering technique does not provide direct information on chain folds, the arrangement
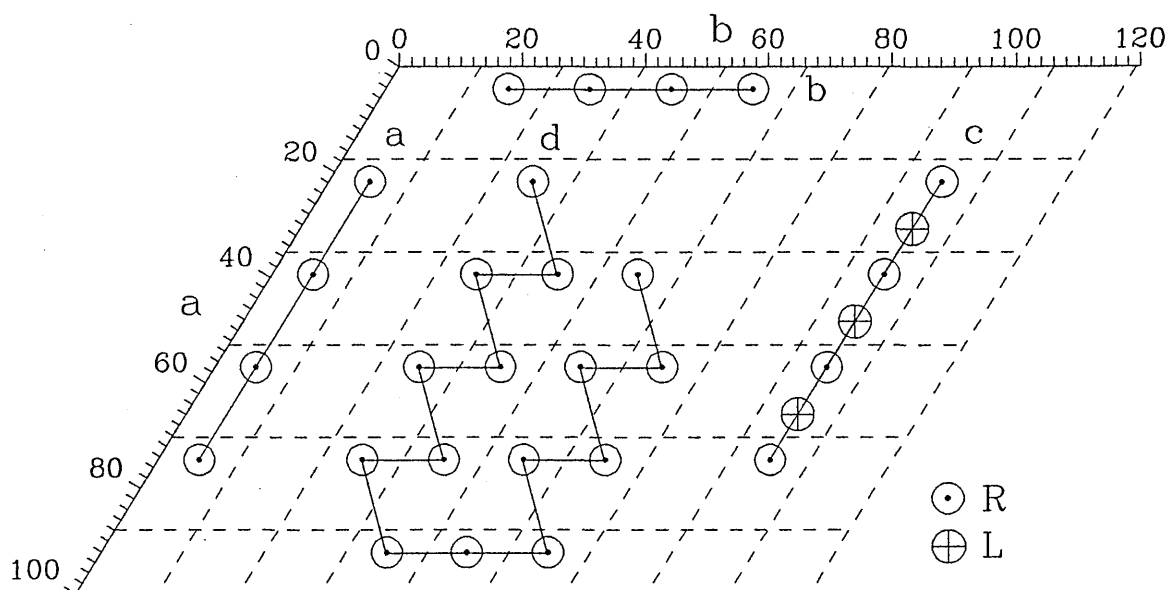
Figure 5.9.

Schematic representation of the different models tested for the folding of sPS molecules in the δ phase. a) Folding along the a-axis, with constant helicity, b) Folding along the b-axis, c) Folding along the a-axis, with alternation of the helicity (a/2 model), d) Zigzag folding.

of stems in a sheetlike structure is indicative of a particular fold direction, and different fold directions imply different interstem correlations. Thus different models were tested

165

and these are represented in figure 5.9. The first two models (a and b) involve folding along one of the main crystallographic directions ($\underline{a}$ or $\underline{b}$) and require the helicity of each stem to be the same along the molecular trajectory. This condition is clearly fulfilled for the $\underline{b}$ direction, while for $\underline{a}$ it implies that the chain does not fold to the first neighbouring site, but to the second. In a third model (c in figure 5.9), called the $\underline{a}/2$ model, we tested the possibility for successive stems to alternate in helicity along $\underline{a}$. This means that the nearest neighbouring sites corresponds to the closest possible separation. In a fourth model (d in figure 5.9), called the zigzag model, the chain occupies two neighbouring [010] planes, the helicity being retained and the overall fold direction being $\underline{a}$.

Assuming the chain to fold within sheets with regular adjacent re-entry, we calculated the resulting intensity for rows of 10 stems. Each type of folding gives rise to a peak corresponding to the smallest interstem distance.

We compared these calculations with the measured intensity (figure 5.10). Unfortunately, the magnitude of the uncertainties in the region $q>0.50\text{Å}^{-1}$, makes it difficult to settle whether there is a peak or not. Though if a peak exists, it would be very narrow, and narrower than the simulated peaks.

The absence of any peak in the available q range would be indicative of the interstem distance being smaller than $2\pi/q_{max}$. This would only be possible when folding occurs along $\underline{a}$ at adjacent sites, with an alternation of the chain helicity (model $\underline{a}/2$). Figure 5.11 illustrates the alternation of the helicity of the sPS chain. Along $\underline{a}$ the helicity alternates and two consecutive stems can only be inter-converted by the operations of a mirror plane inversion plus a translation in the c-direction (corresponding to a change in the chain

handedness). In the a c plane, the interlocking of stems allows close packing. Folding is then in the "nearest neighbour" direction, as might be expected *a priori*. Along the b direction, the consecutive stems are identical and the packing in the b c plane (figure 5.11) is less efficient. There is a precedent for this situation: a "zigzag folding" model was proposed for the molecular conformation in solution-grown isotactic polystyrene crystals [8]. This involved an alternation in helicity and was shown to result in the phenyl rings of neighbouring stems having the same inclination. A similar situation could arise for sPS/ethylbenzene but involving a single fold plane. It is possible to envisage the crystallising molecules with helical segments separated by segments with other bond conformations. High mobility of "defects" in the latter regions, together with their recombination, is then necessary to obtain the alternation of helicity in successive stems laid down. Note also that Chatani et al. [10, 11] have suggested that chain folding was performed along the a-direction. This was based on the changes observed in the orientation of the crystallites after hot drawing of fibres. Further evidence are provided below.
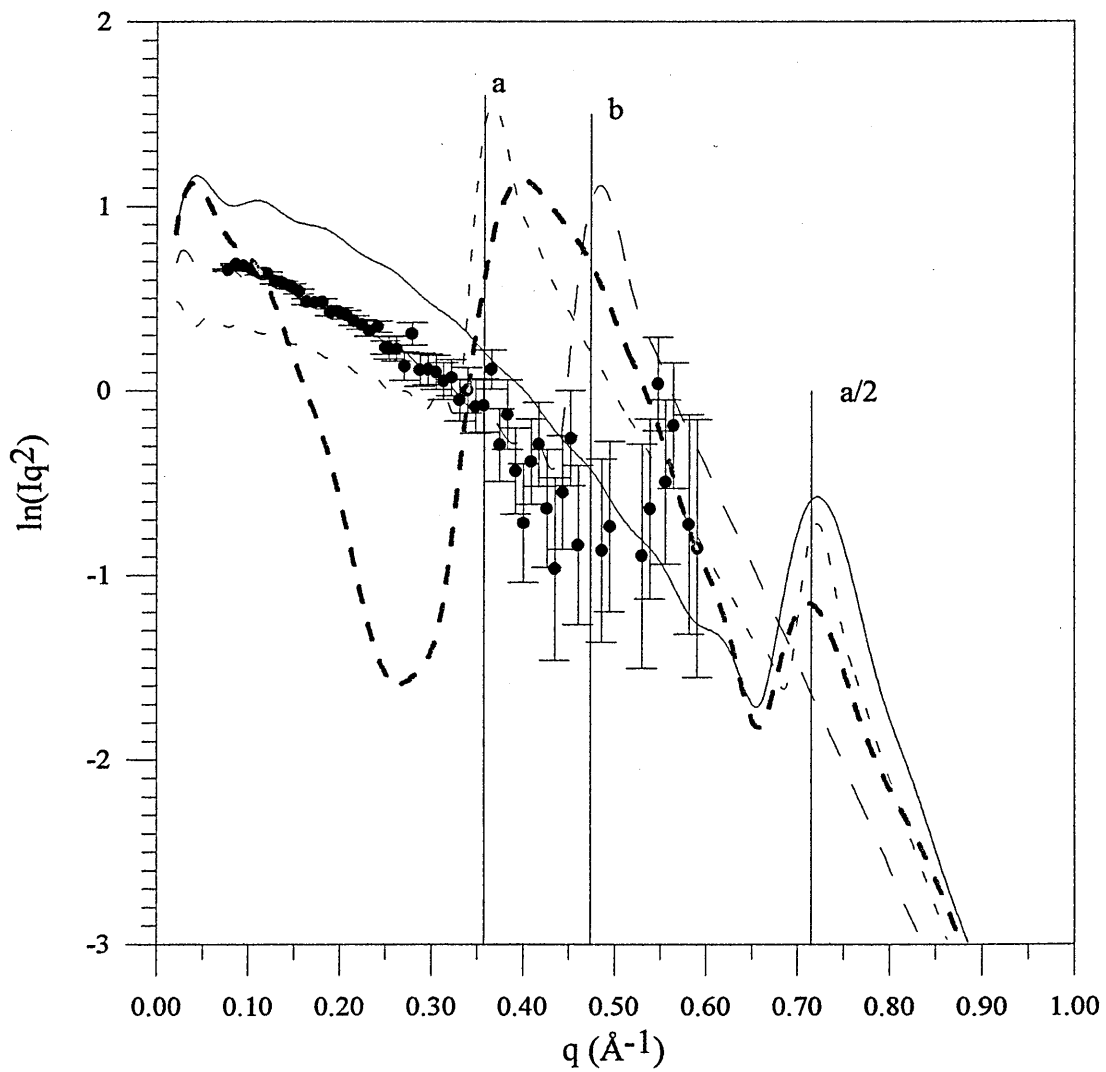
Figure 5.10.

Calculated scattering curves for : - - - - : $\underline{a}$ folding, — — : $\underline{b}$ folding, ——— : $\underline{a}/2$ folding and - - - : zigzag folding. ● experimental difference scattering curve for sample AD (M_w=42700), representative errors bars are indicated.
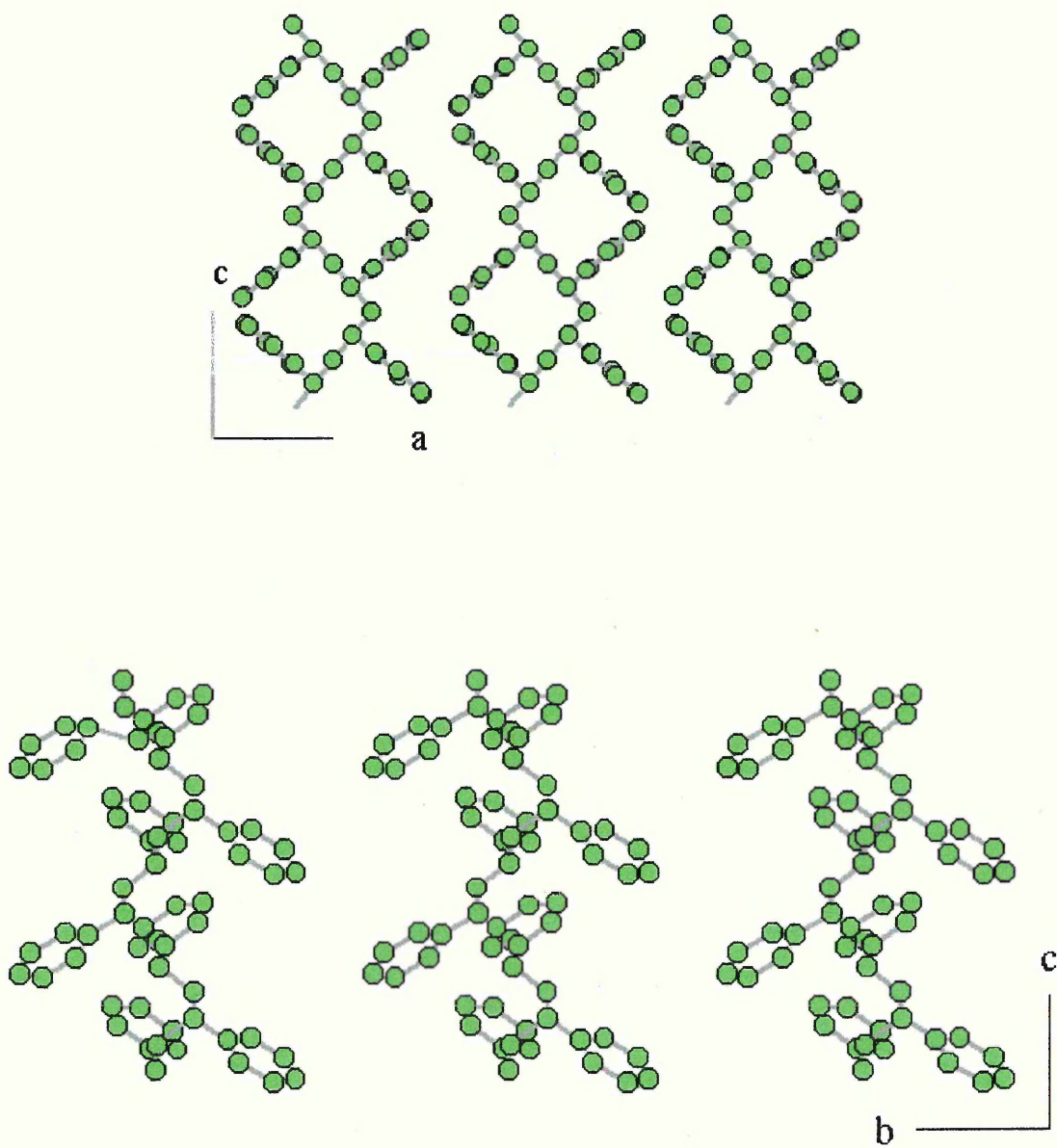
Figure 5.11.

Crystal structure of sPS in the δ-phase viewed along the normal to the [010] plane (top), and to the [100] plane (bottom). The solvent molecules have been omitted.

5.2.4. Results

5.2.4.1 Kratky plots

A) IANS - $q < 0.3 \text{Å}^{-1}$:

Kratky plots (Figures 5.12, 5.13, 5.14) show an increasingly negative slope with increasing molecular weight, beyond the position of the maximum. This peak becomes sharper and its position is shifted to low angle as the molecular weight increases. This behaviour is reminiscent of that shown by polyethylene crystals as a function of molecular weight [6], lending further support to a sheetlike model.

B) IANS - $0.3 \text{Å}^{-1} < q < 0.6 \text{Å}^{-1}$:

For the highest molecular weight (Figure 5.14), in addition to the small angle peak, a second peak is observed at approximately $q = 0.46 \text{ Å}^{-1}$. This peak, absent for the smaller molecular weight (Figure 5.12) indicates the presence of pairs of stems separated by approximately 13.7 Å, and suggests the existence of a second kind of nearest neighbours. This is strong evidence for the existence of a sheet-like structure. In the case of the intermediate molecular weight (figure 5.13), the shape of the Kratky plot seems to be intermediate between those of a single sheet and a double sheet structure.

We consider that the shapes of the curves are of greater significance than absolute intensities: as noted earlier, there is necessarily some uncertainty in both sample crystallinities and intensity enhancement arising from the sample orientation. From proposed figures for the δ-phase crystallinity and the orientation effect noted earlier, we estimate that the experimental intensities require scaling by a factor of around 2, which provides good agreement with calculated data.

We carried out simulations (Figure 5.15) for the different folding models we described, allowing the molecules to superfold so as to be confined in two sheets, containing an equal number of stems. In all the cases, a second peak additional to one observed for the single sheet structure is predicted. The position of this peak depends on the distance between adjacent stems on adjacent sheets. This peak is in fact the sum of two peaks, corresponding to the two smallest interstem distances allowed within the lattice. When the fold direction is $\underline{b}$, a peak at $q = 0.48\text{Å}^{-1}$ is observed (neighbouring stems along $\underline{b}$) with a wide shoulder (stems along $\underline{a}$) at the small angle side. When the fold direction is $\underline{a}$, the peak's maximum is at $q = 0.40\text{Å}^{-1}$ (stems along $\underline{a}$), but its base is extended up to $q = 0.60\ \text{Å}^{-1}$ (stems along $\underline{b}$). When the fold direction is $\underline{a}/2$, a relatively weak and broad peak appears. This peak results from the contribution of pairs of stems separated by a distance of either a or b. In addition a third peak at $q = 0.72\text{Å}^{-1}$, which corresponds to an interstem distance a/2, is predicted.

In the process of finding best fits for the intensity plots, different values for the probabilities P_A and P_U have been tested. Figures 5.16 shows the effect of varying one of these parameters, the other being constant. Clearly, a variation in P_A affects the scattering to a far greater extent than variation in P_U. Finally, the best fits were obtained
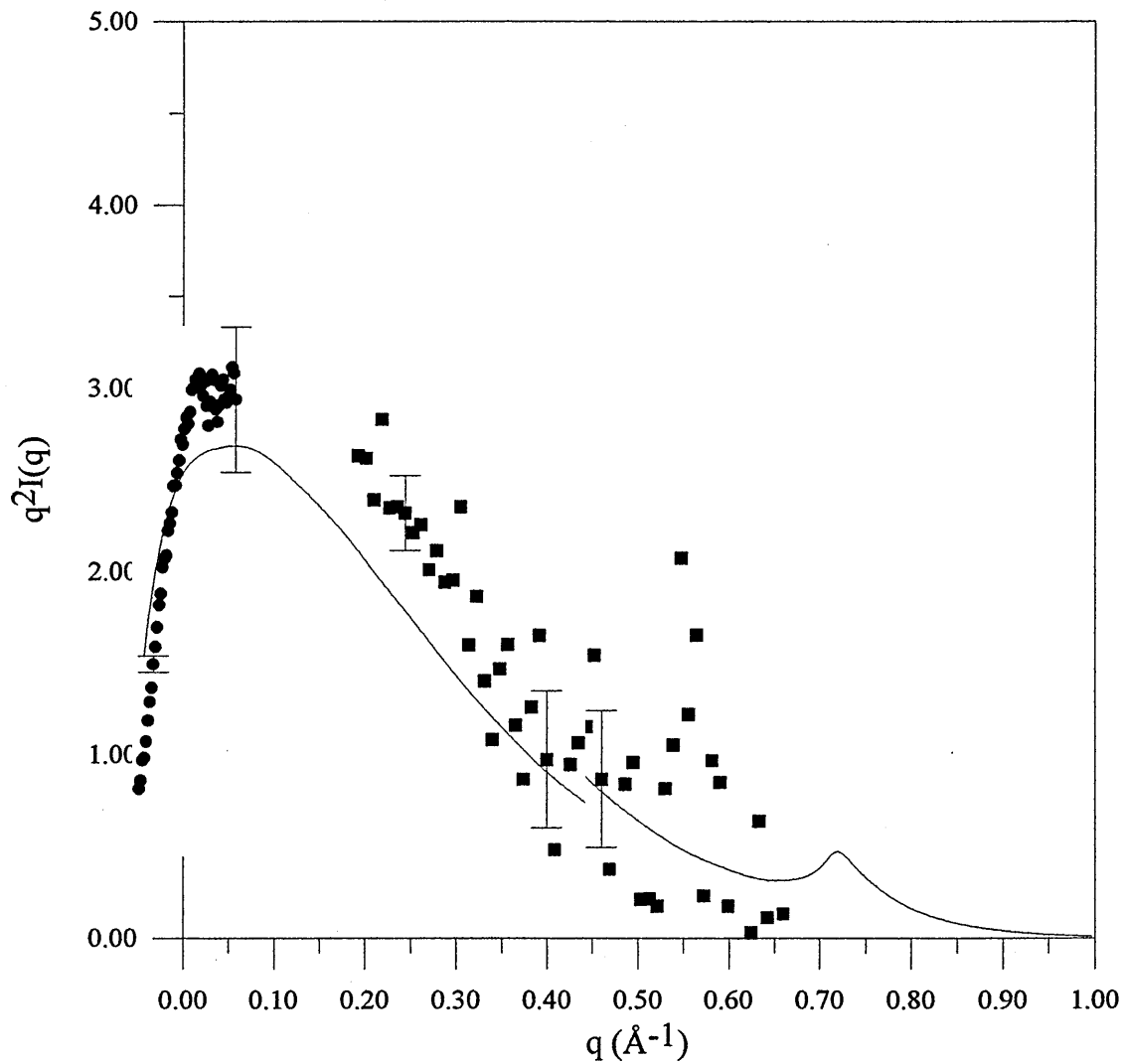
Figure 5.12.

SANS (LOQ) and IANS (D17) data for sample AD ($M_w = 42700$) in the δ phase. ———: calculated scattering curve for 8 stems in 1 sheet, P_A=0.80, P_U=0.18.
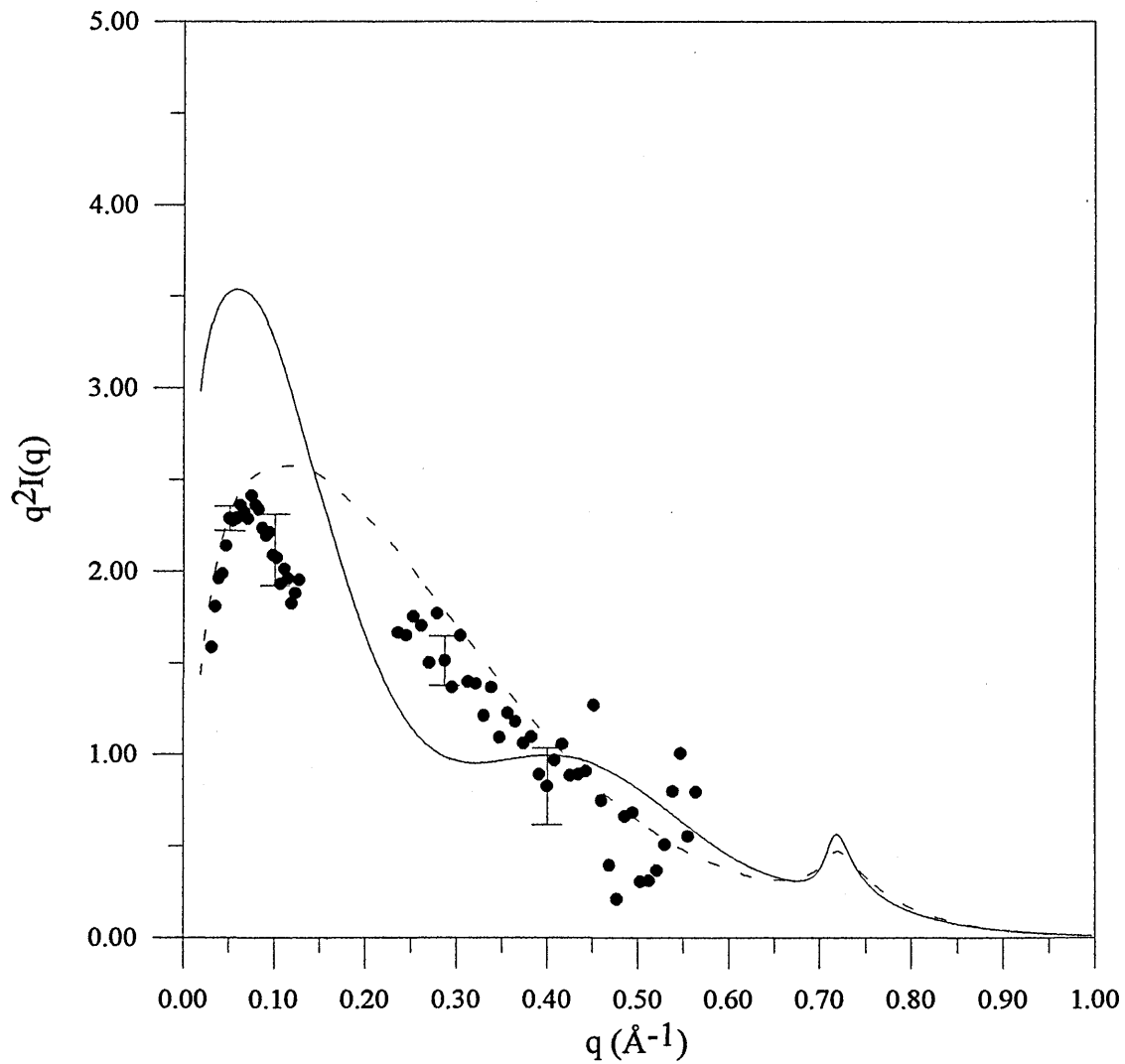
Figure 5.13.

SANS (LOQ) and IANS (D17) data for sample BD ($M_w = 124500$) in the δ phase. Calculated scattering curves for - - - - 8 stems in 1 sheet, ——— 22 stems in 2 sheets, P_A=0.80, P_U=0.18.
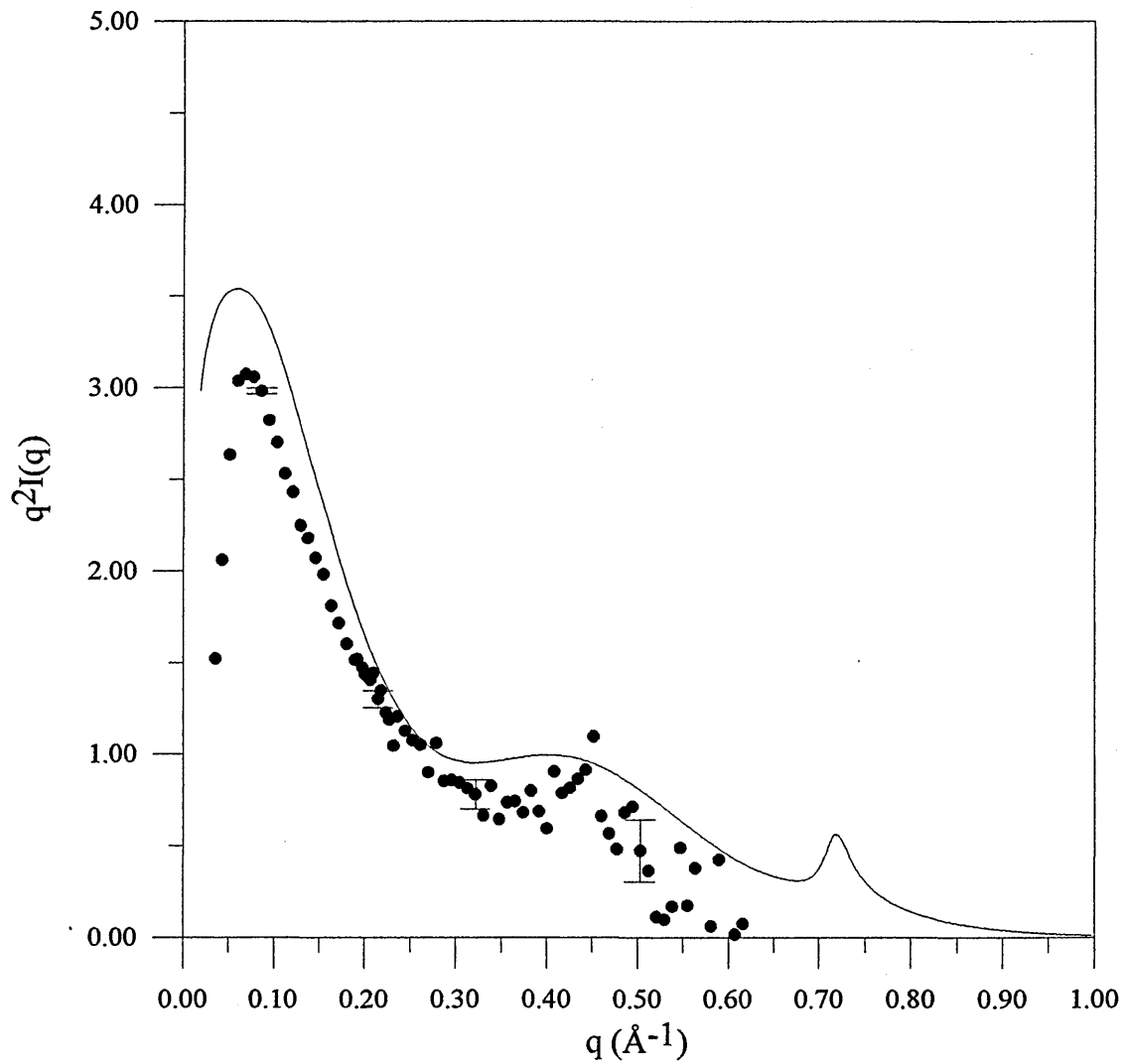
Figure 5.14

SANS and IANS (both from D17) data for sample CD (M_w = 144500) in the δ

phase. ———: calculated scattering curve for 22 stems in 2 sheets, P_A=0.80,

P_U=0.18.
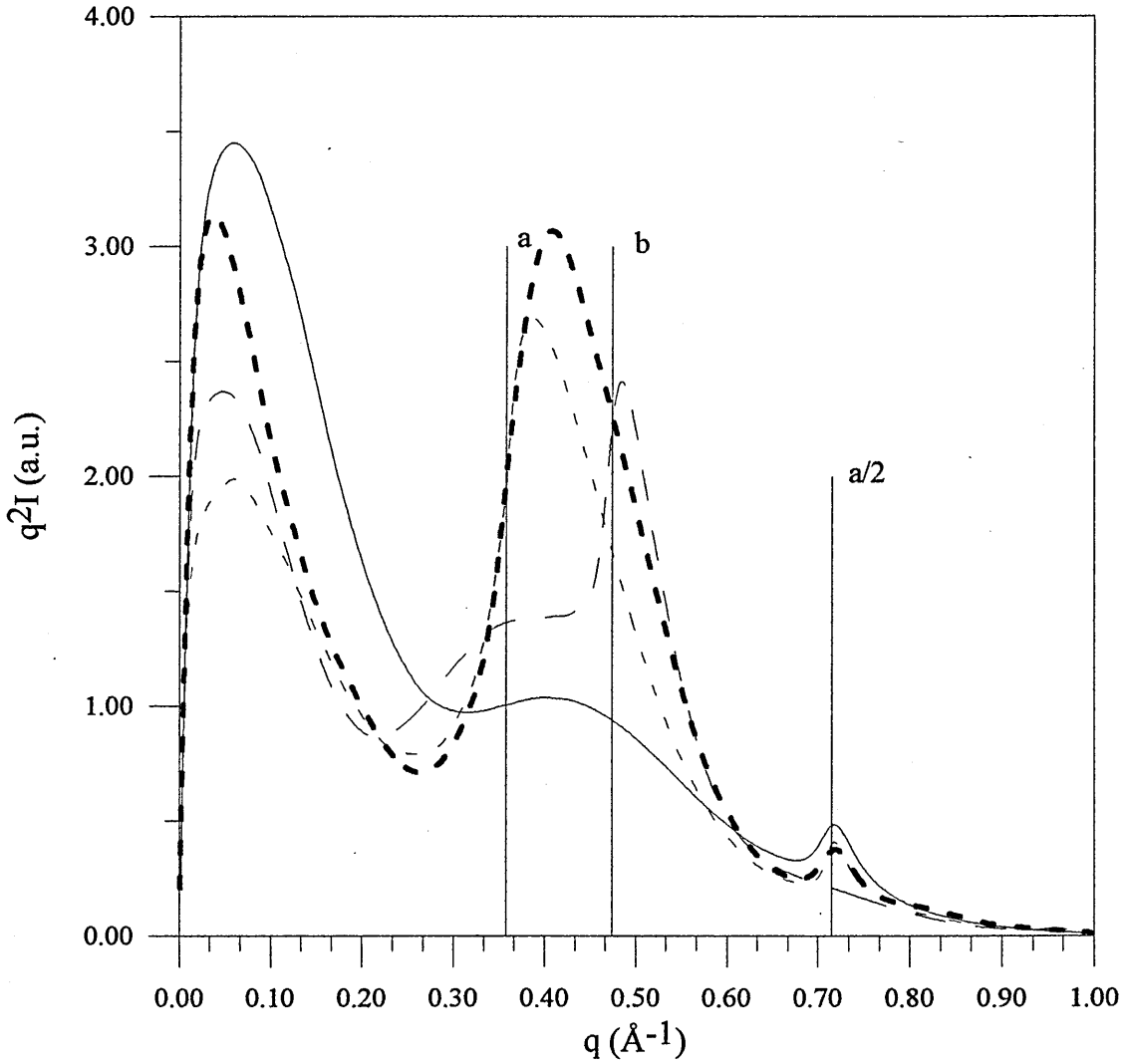
Figure 5.15.

Calculated scattering curves for a double sheet structure each of them containing 8 stems, for the different models with $P_A=0.75$, $P_U=0.25$. - - - - : $\underline{a}$ folding, — — : $\underline{b}$ folding, ——— : $\underline{a}/2$ and - - - : zigzag folding. Vertical lines represent relevant crystallographic spacings.
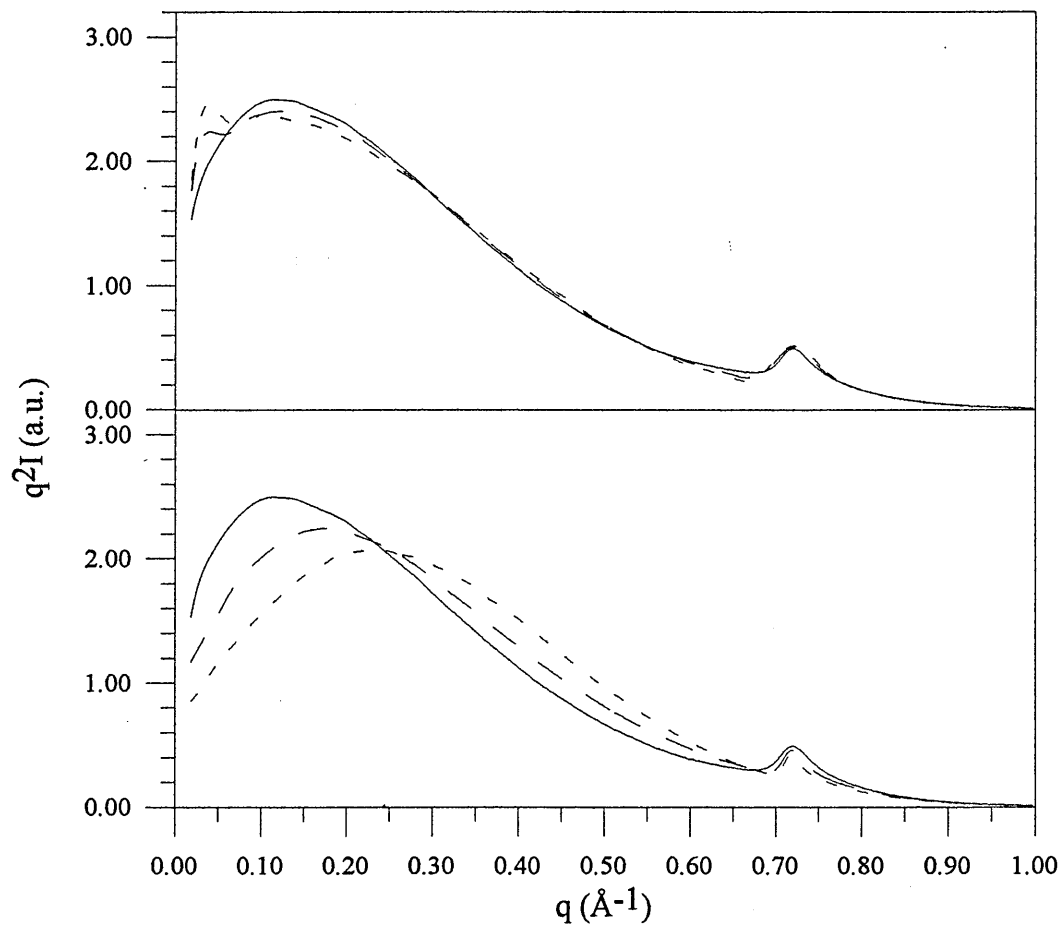
Figure 5.16.

Influence of P_U (top) and P_A (bottom) on the scattering intensity calculated using the statistical model for a single sheet structure (9 stems, $\underline{a}/2$ folding). Top P_A=0.75 and ———— : P_U=0.25, —— —— : P_U=0.50, - - - - : P_U=0.75. Bottom P_U=0.25 and - - - - : P_A=0.25, —— —— : P_A=0.50, ———— : P_A=0.75.

when the fold direction is $\underline{a}/2$ and $P_A = 0.80$. These fits are presented in figures 5.12, 5.13 and 5.14.

5.2.4.2. Radius of gyration

As a further test for our model, for each molecule generated the radius of gyration was calculated and an average was made which can be compared with the measured radius of gyration and that obtained using the analytical expressions. In the last case, this allows us to test the statistical validity of the simulations. For a thin sheet-like structure, the relation between the in-plane radius of gyration and the dimension of the sheet L_c is [11]:

$$R_g^2 = \frac{L_c^2}{12} \tag{5.4}$$

where $L_c = Nd$, N is the number of stems in the sheet and d the average distance between two consecutive stems in a sheet. d is related to the probabilities P_A and P_U and the smallest interstem distance d_i according to equation 3.50

$$d = d_i \left[P_A + (1 - P_A) \frac{(1 + P_U)}{P_U} \right] \tag{5.5}$$

In-plane radii of gyration are compared in table 5.3.

Sample (M_W)	R_g (Å)	
	Measured	Simulations
AD (42700)	44.8	44.3 (42.5)
BD (124500)	76.1	
CD (144500)	67.9	69.3

Table 5.3.

Comparison between measured in-plane radii of gyration and those resulting from the simulations. The number in brackets is the radius of gyration of a single sheet structure calculated using the analytical expression (5.4) and (5.5). As the scattering from sample BD is consistent with a mixture of single and double sheet structures, a radius of gyration is not quoted for the simulations.

Good agreement is shown, consistent with the previous findings in terms of structure (a sheetlike structure, with the fold direction as proposed here) and statistical parameters. For the smallest molecular weight, the calculated radius of gyration for a single sheet structure also shows good agreement demonstrating the quality of the sampling used for the statistical calculations.

The case of the intermediate molecular weight is interesting, in that the measured radius of gyration is larger than expected from its molecular weight. If the molecular weight distribution of sample BD matches the region of transition from single to double sheet, some molecules will be in one sheet, while others will be in two. In the first case, for a similar number of stems, the resulting radius of gyration will be much greater, increasing the average above the value expected for a double sheet structure.

5.2.4.3. Cluster size distribution

Taking the value of P_A to be 0.80, with $\sigma = 22$ (corresponding to the highest molecular weight studied), leads to the distribution of stems within clusters of different size shown in Figure 5.17. The slight increase for the cluster size 22 is related to the maximum number of stems available to build a cluster. A very similar distribution was found from our simulations. For the parameters chosen here, the largest number of stems are in clusters of size $t = 4$. The average cluster size $<t>$ can be calculated using the equation 3.49:

$$\langle t \rangle = \frac{\sigma}{\sigma - P_A(\sigma - 1)} \qquad (5.6)$$

which gives $< t > = 4.23$ with the parameters given above. A typical molecular trajectory is shown in figure 5.18.
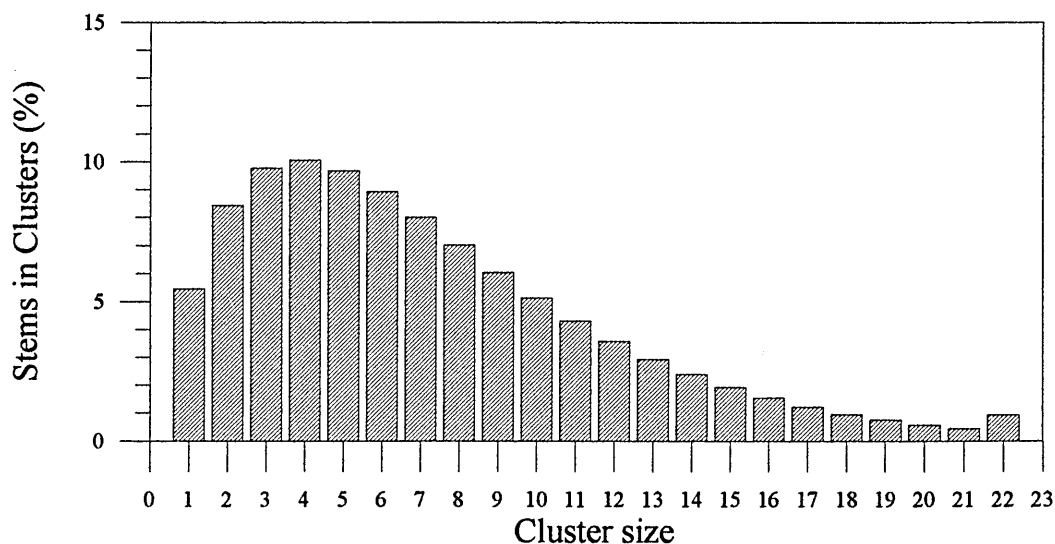
Figure 5.17.

Calculated distribution of numbers of stems in particular clusters as a function of cluster size, for a sheet of 22 labelled stems ($P_U=0.183$, $P_A=0.80$).
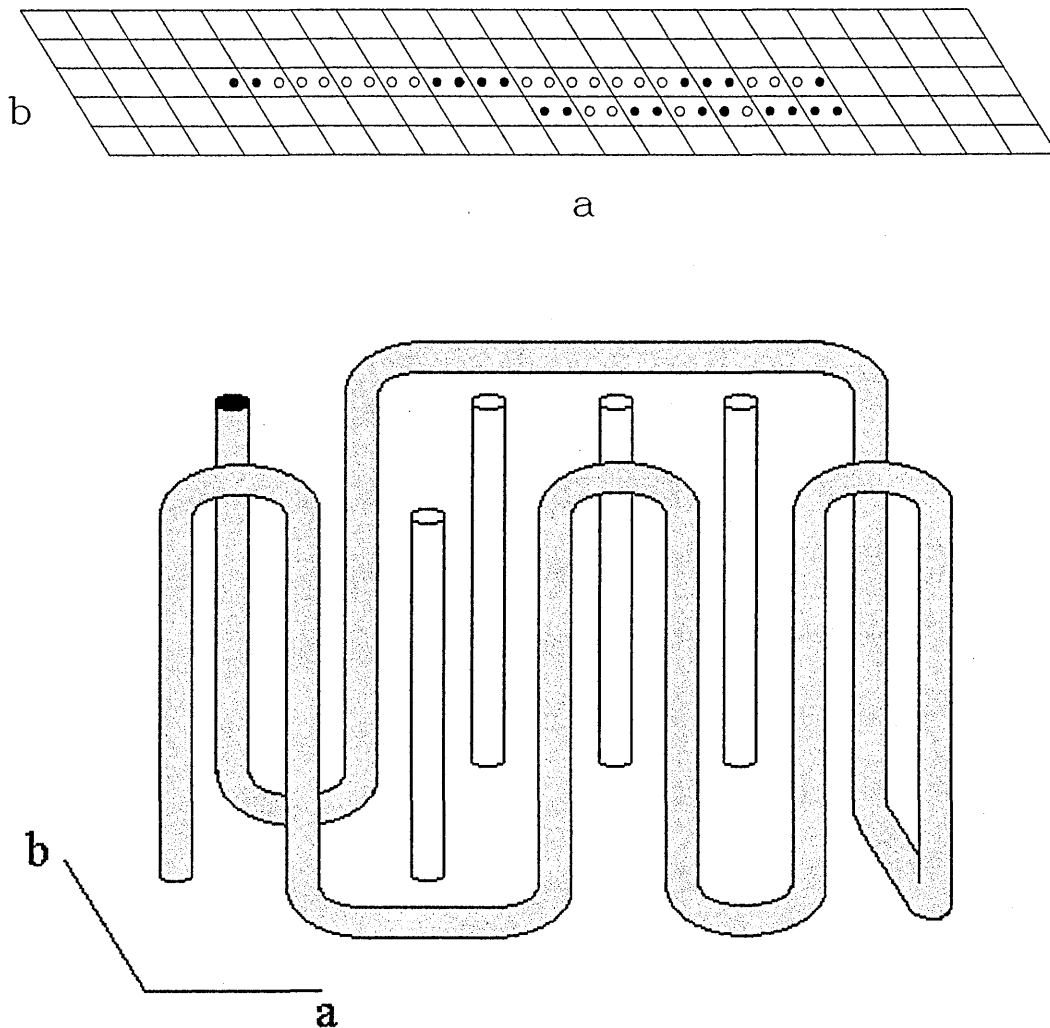
Figure 5.18.

Top : Schematic representation of the molecular conformation of a labelled molecule within the lamella. Bottom : Perspective diagram of the arrangement of part of this molecule within the crystal lattice, including the superfold. The shaded spots and "tubes" represent a second (unlabelled) molecule.

5.2.5. The γ phase

In the previous section, an increase in the radius of gyration on moving from the δ to the γ phase was shown to demonstrate significant movement of stems during the transition. A rough evaluation was made of the magnitude of this movement, assuming that the stems are allowed to move out of the plane of the sheet. We calculated the scattering intensity for a model with stems able to move to either side of the initial sheet. We started with a single sheet built using the probabilities and folding direction determined in the previous sections and allowed this to be disrupted by moving a proportion of stems. The results are shown in figure 5.19. The main new feature of the intensity curve is the appearance of a peak at approximately q=0.55 Å^{-1} corresponding to the dimension $\underline{b}$ in the monoclinic lattice of the γ phase. Note that in the γ-phase the unit cell parameter $\underline{b}$ is smaller by about 2Å in comparison to the δ phase. The sample with $M_w = 42700$ was chosen for the comparison, and the scattering data shows a peak in the expected region. This tentative model requires further refinement, but the presence of the 0.55Å^{-1} peak clearly shows that a redistribution of the stems along the $\underline{b}$ direction occurs at the transition.

Summary

We propose a sheetlike model for the chain conformation in the δ phase of sPS/ethylbenzene. Neutron scattering data have been used to test different folding models.

Among them, folding along the direction $\underline{a}$ with a regular alternation in stem helicity gives the best agreement with neutron scattering curves, on the basis of the absence of a diffraction peak below $q = 0.60\text{Å}^{-1}$, while also reproducing the measured in-plane radius of gyration. Thus the stem arrangements involve folding in the nearest neighbour direction. As was already suggested in section 5.1, the molecular weight range we used appears to be around the transition from a single-sheet to a double-sheet structure.

The statistical model indicates a strong preference for adjacent reentry. Coincidentally, the model parameters, and particularly the high probability of adjacent re-entry, are similar to those derived for polyethylene crystallized from dilute xylene solution at high supercoolings.

Lamellar thickening at the transition to the γ phase is accompanied by a local rearrangement of the crystal stems, similar to the solid state diffusion mechanism in the annealing of polyethylene, with the in-plane radius of gyration showing an increase. This is taken into account in our model which involves a displacement of stems out of the initial sheet to their neighbouring lattice sites. This explains the peak observed in the IANS data, which corresponds to adjacent stems at a separation of b on the monoclinic lattice of the γ phase, clearly showing that the transition involves a redistribution of stems along the $\underline{b}$ direction.
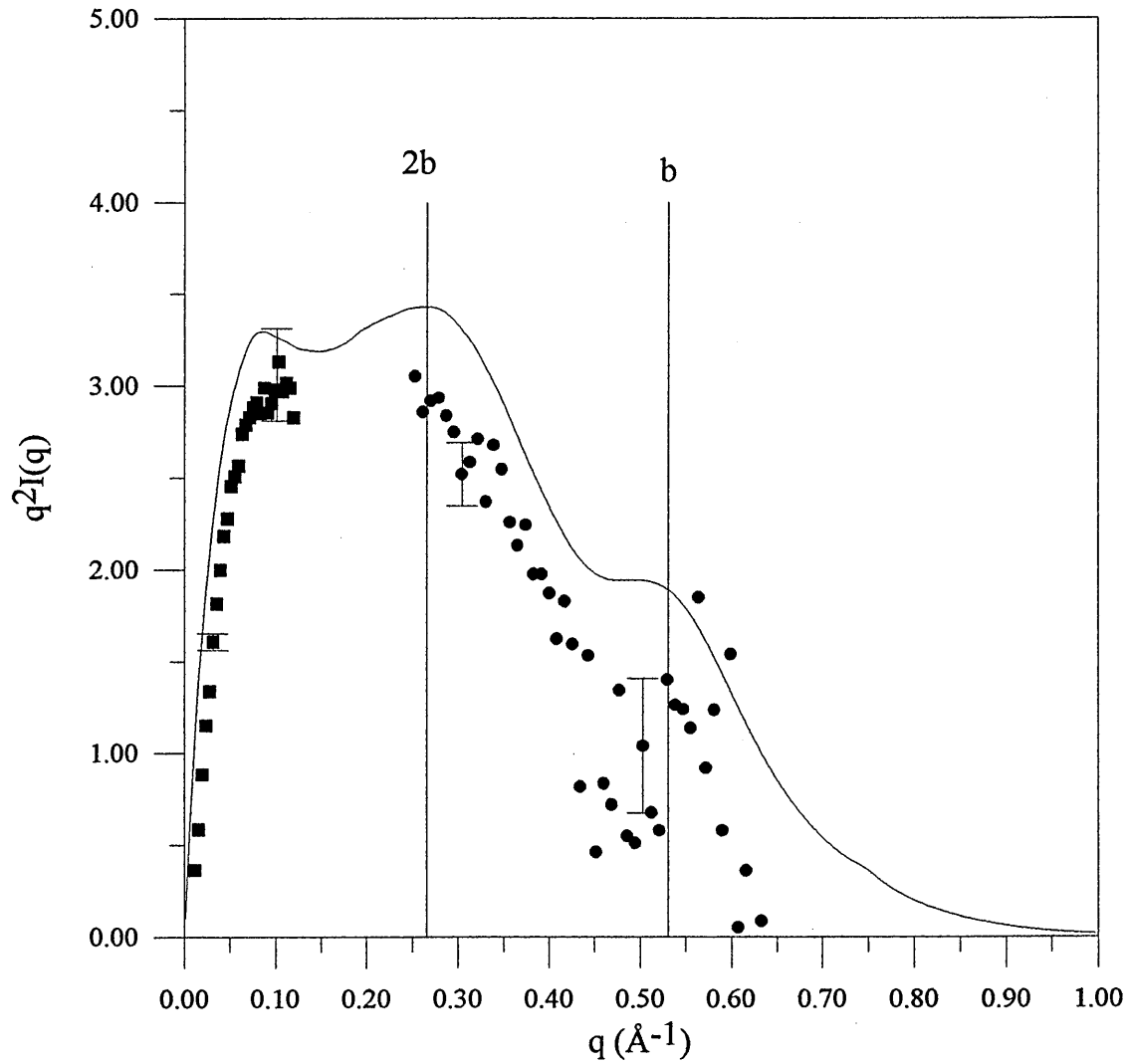
Figure 5.19.

SANS (ISIS) and IANS (ILL) data for sample AD (M_w = 42700) in the γ phase.
——— : calculated scattering curve for the disrupted sheet model. Each stem of
the initial sheet is allowed to move out to the neighbouring sheet.

5.3 Anisotropic Small Angle Neutron Scattering

Introduction

The neutron scattering measurements discussed previously were all undertaken with the mat normal parallel to the incident beam. Data analysis and comparison with the results of computer simulations were essentially carried out using two-dimensional projections of the crystal stems, as is appropriate for a well oriented sample in this geometry. However, to obtain a more complete understanding of the structures and of the conformational changes at the transition, it is necessary to invoke the full three-dimensional chain trajectory. We have made SANS measurements of oriented sPS mats, with the mat normals tilted away from the incident beam. The resultant anisotropic signal has been analysed using a method [18, 37] which makes use of the whole area of the two-dimensional detector to give radii of gyration both in the plane of the lamellae (R_{xy}) and along the lamellar normals (R_z). A comparison between values obtained for R_z and for the X-ray long spacing (l_x) then allows conclusions to be made about whether a molecule occupies one or more lamellae. This feature has important implications for the extent of molecular mobility required to accomplish the δ to γ phase transition.

5.3.1 Experimental

Neutron scattering measurements were made using instrument LOQ at the ISIS neutron source. The range of scattering wavevector was from 9×10^{-3} Å^{-1} to 0.25 Å^{-1}. A goniometer mounting was used to tilt samples by 30° with respect to the beam direction, about a horizontal axis.

Data reduction and analysis was mostly undertaken using the Collette program at ISIS. A similar data reduction procedure as that used for untilted samples was followed here. The major difference was that the detector was divided into 24 sectors, each with an azimuthal width of 15°. Subtraction of a purely hydrogenous sample was carried out as previously described, and the same sample was used to calibrate the intensity scale.

The raw data, in the form of count rate over the array of the 64×64 counter elements (figure 5.20) was reduced to intensity values $I(2\theta, \Phi)$. Φ is the azimuthal angle between the direction of measurement and a vertical line of the detector. Equal angular sectors of 15° gave seven independent values of Φ from 0 to 90°.
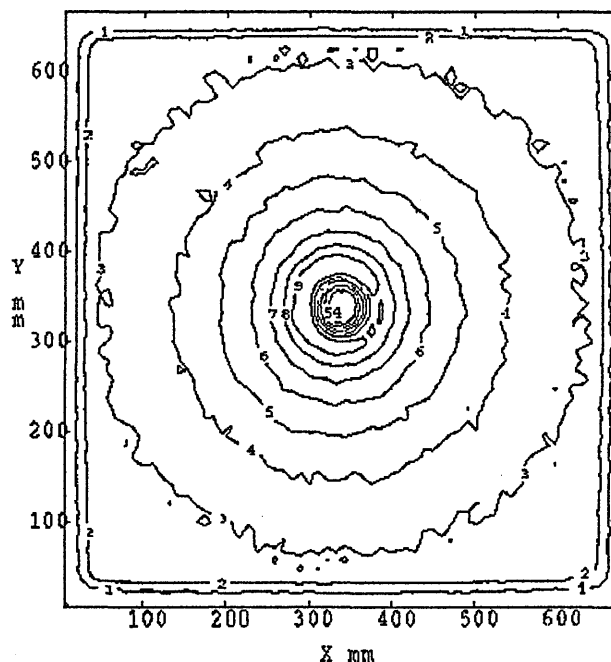
Figure 5.20.

Contour map of the SANS intensity distribution of the sample DD/BH δ tilted by 30° about a horizontal axis.

5.3.2 Method of analysis

The data for each sector can be represented by:

$$\frac{I(0)}{I(q)} = 1 + q^2 \langle d^2 \rangle \tag{5.7}$$

where d is the distance of part of the molecule from its centre of gravity, projected onto the direction (S′) through the sample which is parallel to the direction in the plane of the detector (S) along which the intensity is measured [37]. An angle α is then defined as the angle between the measurement direction (S) and the sample normal (n) (see figure 5.21).

Following reference 18, the behaviour as a function of the angle α can be written:

186

$$\langle d^2 \rangle = \langle a \rangle + \langle b \rangle \cos^2 \alpha \qquad (5.8)$$

where

$$\langle z^2 \rangle = \langle a \rangle + \frac{\langle b \rangle}{3} \left[1 + \frac{2}{\langle P_2(\gamma) \rangle} \right] \qquad (5.9)$$

and

$$\langle l^2 \rangle = 2\langle a \rangle + \frac{2\langle b \rangle}{3} \left[1 - \frac{1}{\langle P_2(\gamma) \rangle} \right] \qquad (5.10)$$
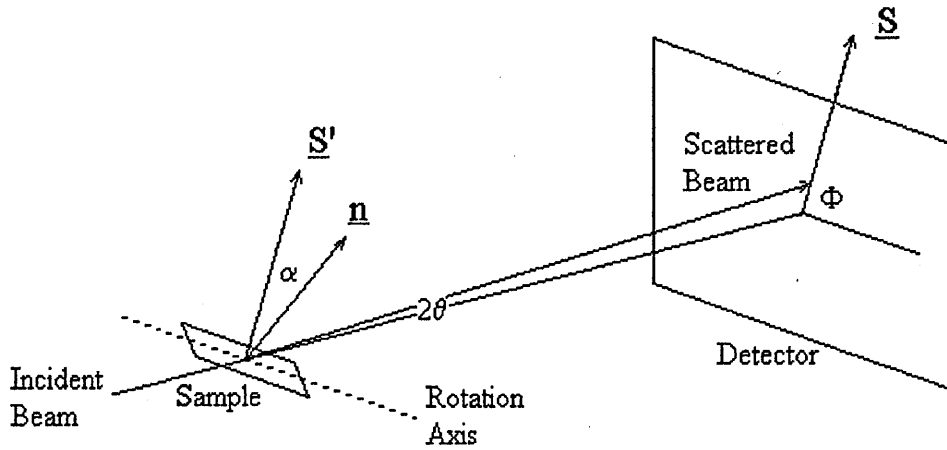
Figure 5.21.

Schematic diagram of the neutron scattering experiment. $\underline{S}$ is the direction within the detector along which measurements of intensity are made and $\underline{S}'$ passes through the sample, parallel to $\underline{S}$. The sample normal is $\underline{n}$, and the angle α is that between $\underline{n}$ and $\underline{S}'$.

Here, $P_2(\gamma) = 3\cos^2 \gamma - 1$ is a Legendre polynomial, with γ the angle between $\underline{n}$, the sample normal and $\underline{n}'$, a local crystallite normal. Let $\underline{r}$ be the position of part of the molecule with respect to its centre of gravity, with z and l the components of $\underline{r}$ along and at right angles to $\underline{n}'$ respectively.

To obtain in-plane (R_{xy}) and out-of-plane (R_z) radii of gyration then requires the use of equations 5.9 and 5.10, the evaluation of $P_2(\gamma)$ from SAXS measurements and the use of the identities:

$$R_z = \left\langle z^2 \right\rangle^{\frac{1}{2}} \tag{5.11}$$

and

$$R_{xy} = \left\langle \frac{l^2}{2} \right\rangle^{\frac{1}{2}} \tag{5.12}$$

SAXS diffraction patterns were analysed using a microdensitometer to give an average value of $P_2(\gamma) = 0.34$ (section 4.3.1.2).

5.3.3 Results

Figures 5.22 and 5.23 show representative Zimm plots for δ and γ phase samples respectively, using data for equatorial and meridional sectors in each case. As with previous isotropic data, the plots show small excess intensity at smallest angles, with linear
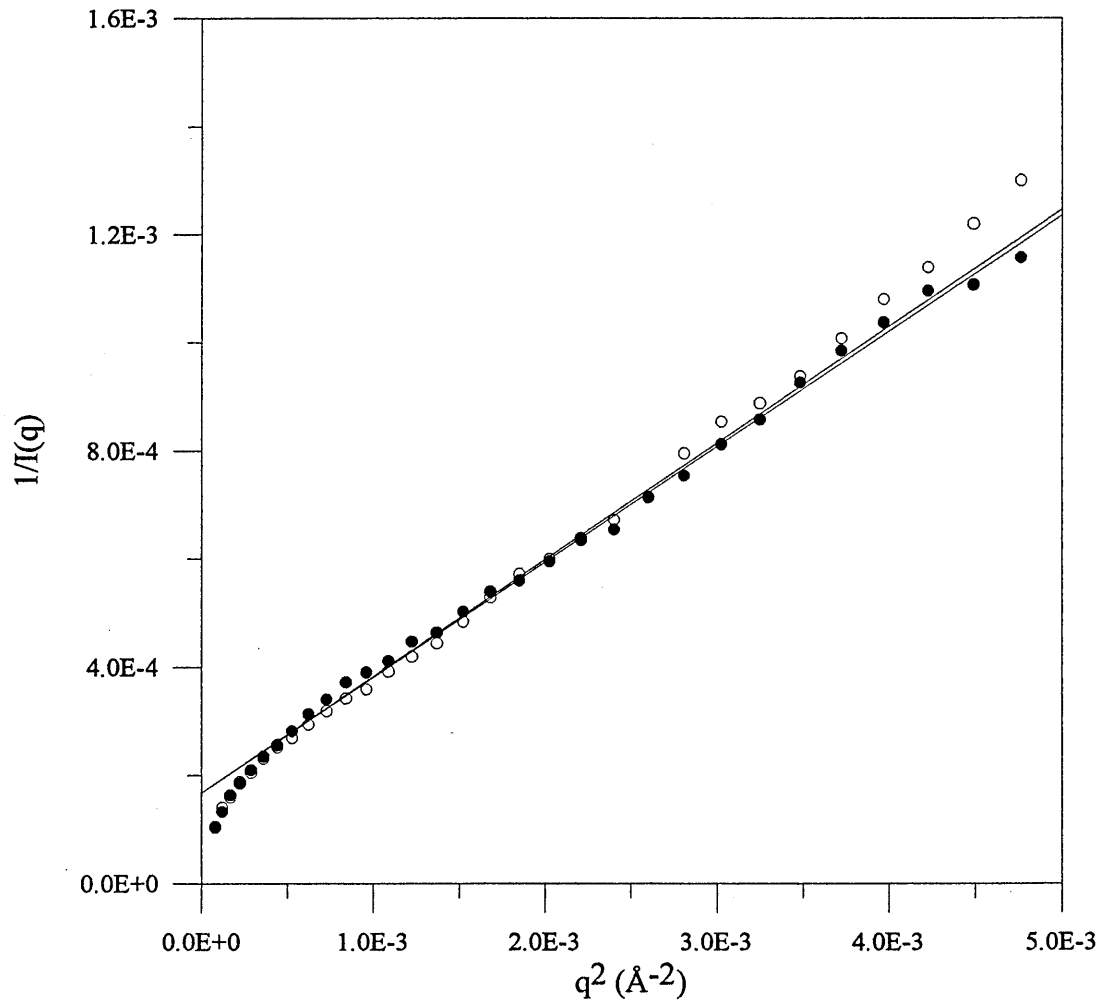
Figure 5.22.

Typical Zimm plots for sample DD/BH in the δ phase, for the intensity along the meridian ● and the equator ○ of the detector, with corresponding linear fits. The intercept at q=0 was imposed as a constant.
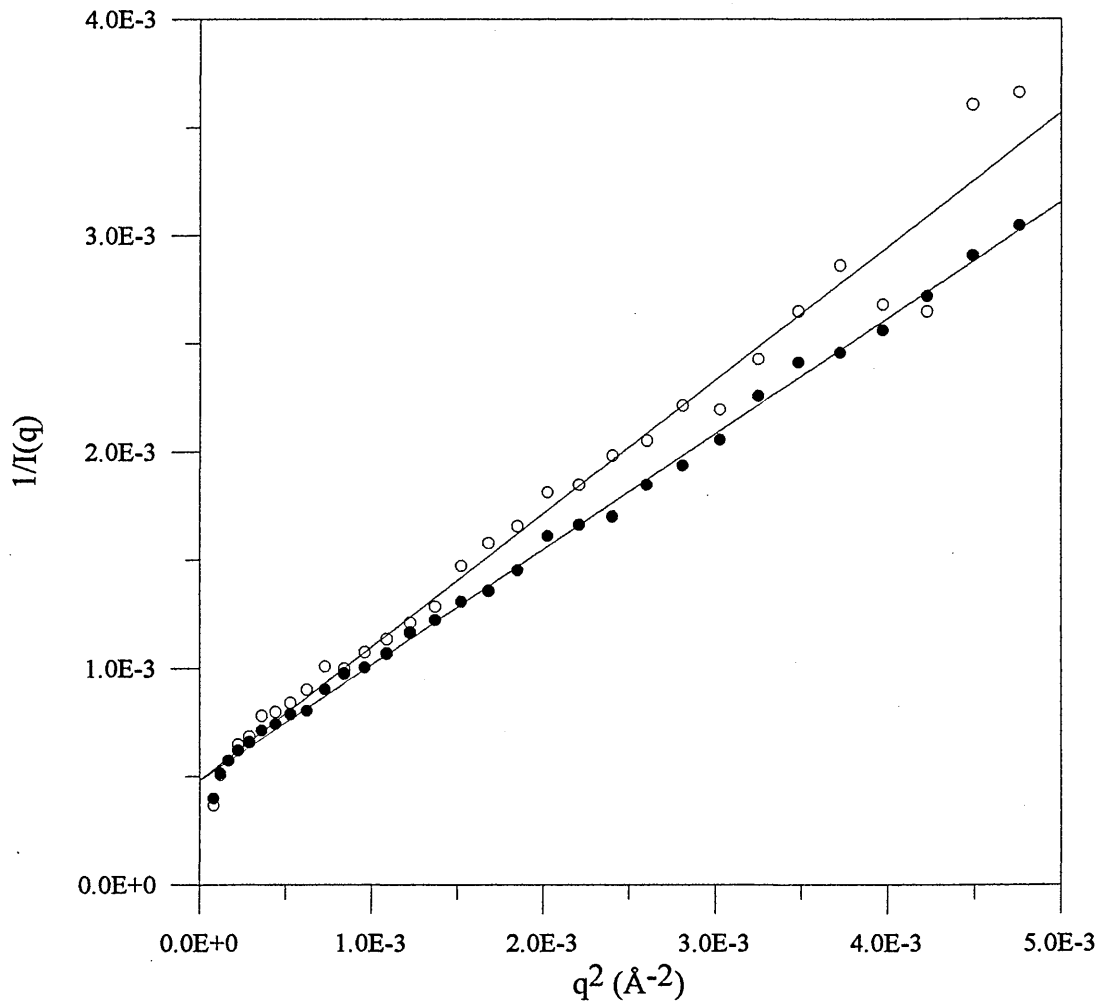
Figure 5.23.

Typical Zimm plots for sample AD/BH in the γ phase, for the intensity along the meridian ● and the equator ○ of the detector. The intercept at q=0 was imposed as a constant.

behaviour well within the limit of $q < 1/R_g$. Fits were obtained, using the requirement that for all sectors the same intercept is obtained at $q = 0$.

Figures 5.24 and 5.25 show plots according to equation 5.8 for low and high molecular weight samples respectively, with both δ and γ phase data points shown together.

190

Sample	M_w	R_g (Å)	R_{xy} (Å)	R_z (Å)	$l_x / 2\sqrt{3}$ (Å)
DD/BH/δ	124000	61	36 ± 1	35 ± 2	17
DD/BH/γ	124000	85	52 ± 2	45 ± 4	21
AD/BH/δ	42700	52	33 ± 1	23 ± 3	17
AD/AH/γ	42700	55	41 ± 2	22 ± 9	21

Table 5.4.

Molecular dimensions. R_g is the in-plane radius of gyration measured by isotropic small angle neutron scattering (section 5.1). R_{xy} and R_z are the dimensions in the mat plane and along the mat normal respectively, as measured in this work. l_x is the long period measured by SAXS.

Values thus obtained for the radii R_{xy} and R_z are listed in Table 5.4, along with the quantity $l_x / 2\sqrt{3}$, derived from the X-ray long spacing l_x. For molecules confined to a single lamella, the value of R_z is expected to equal $l_x / 2\sqrt{3}$. As can be seen from the table, for the lower molecular weight this equality is satisfied for the γ-phase sample and approximately for the δ-phase sample. However, for the higher molecular weight, values obtained for R_z are close to twice the value of $l_x / 2\sqrt{3}$ in both δ and γ phases. This indicates that on average a molecule occupies two lamellae.

Also listed are the values of radius of gyration, R_g, obtained for the oriented mats with the mat normal in the beam direction. The quantity R_{xy} is expected to be smaller by a factor of $\sqrt{3}$, and the data generally approximately follow this relationship.
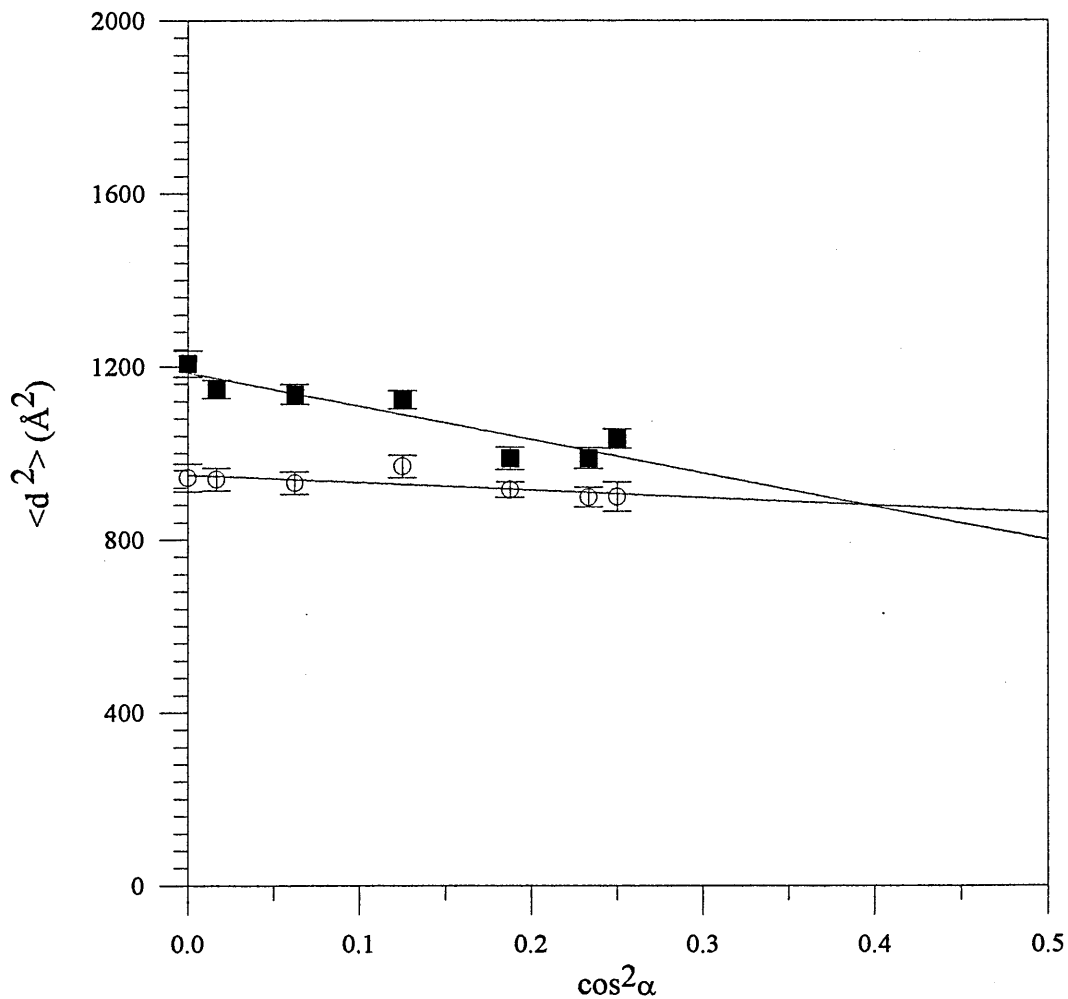
Figure 5.24.

Plot of $<d^2>$ versus $\cos^2\alpha$ for sample with low molecular weight (M_W=42 700).

■ : γ phase, O : δ phase.

5.3.4 Discussion

From our previous chain conformational model for the δ phase (sections 5.1 and 5.2), superfolding was shown to be absent at the lower molecular weight studied here, whereas a
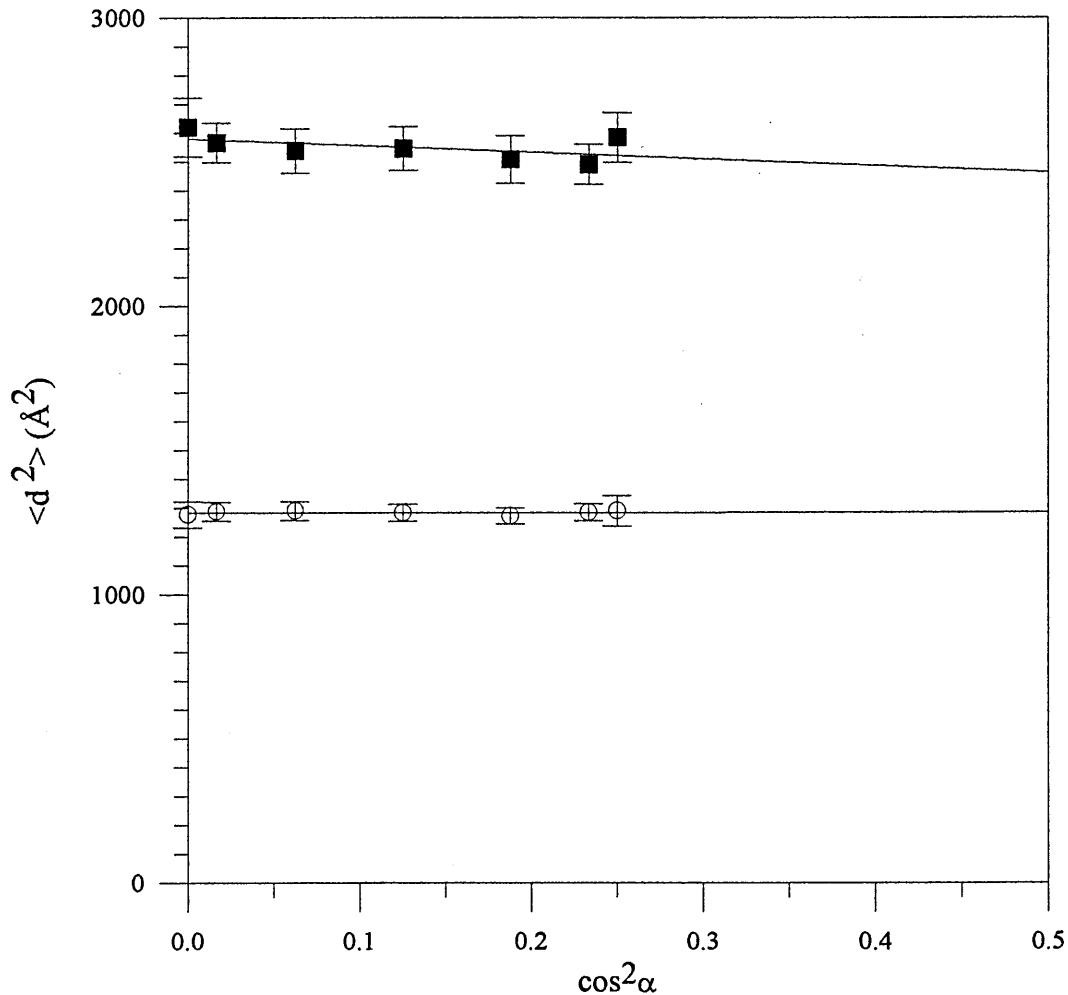
Figure 5.25.

Plot of $<d^2>$ versus $cos^2\alpha$ for sample with high molecular weight $(M_W=124\ 000)$. ■ : γ phase, O :δ phase.

proportion of two sheet structures were found necessary to describe the higher molecular weight sample. We conclude that the probability of a molecule leaving one lamella to enter another is similar to its probability of superfolding. Considering the higher molecular weight sample, in view of the small total number of stems involved, it is likely that the two lamellae occupied by a single molecule are adjacent.

It is worth noting that a similar model, with multiple lamellar occupation, has previously been proposed for isotactic polystyrene samples crystallised from solution at high supercoolings [7]. Features such as sheetlike growth, superfolding and the occupation of more than one lamella appear, therefore, to be general to solution crystallisation, irrespective of whether or not complex formation is involved.

The fact that the number of lamellae occupied by a single molecule remains unchanged on passing from the δ to γ phase transition has significance for the mechanism of the transition. It has been shown that on heating a δ phase sample, decomplexation involves a disordering of the helical stems (chapter 4). We proposed that this allows lateral movement of helical segments out of (010) planes. The increase in helical order on completion of the transition is interpreted as evidence of complete stems having moved out of the original sheets, giving rise to a larger in-plane radius of gyration (R_{xy}) in the γ phase (see table 5.4). The present work indicates that chain mobility at the phase transition only occurs within the individual lamellae and does not involve movement into neighbouring lamellae

Chapter 6

Discussion and Conclusion

Introduction

We have established, using a set of techniques, the chain conformation in the δ-phase and suggested a model for that in the γ-phase. The mechanisms involved during the transition between these two phases have also been examined. In this chapter, we make a synthesis of the results gained by the different techniques in order to clarify the macromolecular conformation in the lamella and the mechanisms involved during the transition.

6.1 Discussion

6.1.1. Morphological features

The thermal analysis of sPS/ethylbenzene has shown the existence of three complexes, of which the stoichiometries are 1.4, 0.5 and 0.25. We have studied the polymer/solvent complex formed by sPS with ethylbenzene when it crystallizes at 40°C in dilute solution (0.1% w/w). At this concentration, the glass transition temperature is usually slightly higher than the melting temperature of the δ-phase [90]. Thus, the formation of this complex for the δ-phase could be stabilized by the glass transition. TEM showed that the morphology obtained under these conditions is lamellar, while for a higher temperature of crystallization a fibrous structure was observed [16]. The thickness of these lamellae measured by SAXS is of about 60Å. The crystal structure is shown to be monoclinic, with cell parameters identical to those given by Chatani et al. for the complex with toluene [11]. In addition, the stoichiometry proposed by Chatani for the sPS/toluene complex equals that measured for the complex C_3, namely 1 solvent molecule for 4 monomers. The γ-phase is also monoclinic and showed a decrease of 1.6Å in the b dimension. This result is also in agreement with previous work [11, 16]. In conclusion, the crystal structure of Chatani for sPS/toluene is also relevant to that of sPS/ethylbenzene.

It should be noted that the type of structure obtained here may not be typical of polymer/solvent complexes. For instance, when crystallization occurs at 50°C, a more fibrous morphology was observed. Thus the existence of a lamellar structure may be

representative of sPS/solvent complexes only under these precise conditions of crystallization.

6.1.2. The chain conformation in the δ-phase

Radii of gyration measurements using a range of molecular weights give for the exponent α in the relationship $R_g \propto M^\alpha$ a value of 0.31. This value is intermediate between that expected for a sheet-like structure ($\alpha \rightarrow 1$) and a superfolded structure ($\alpha \rightarrow 0.1$). Intermediate angle neutron scattering confirmed this interpretation of the small angle data. Stems are contained into sheets lying along the crystallographic [010] direction. In these sheets, adjacent re-entry is predominant (80%). When adjacent folding occurs, it is done so as to achieve the closest contact (8.8 Å) between stems of the same molecule. According to the crystal structure of Chatani et al. [11], this means that a macromolecule changes its helicity with each adjacent site. For high molecular weights, departure from the single sheet occurs, each macromolecule becoming incorporated in several sheets. Incorporation in several lamellae also becomes possible for high molecular weights.

Thus, sPS/ethylbenzene crystals present the same features as other well known solution-grown polymer crystals, in particular, the existence of sheet-like structures. The probability of adjacency for PE was shown to be of 75%. A dependence of the probability of adjacency on supercooling is likely, from changes in the crystallization regime [92]. Thus, the value we found for sPS is coincidentally close to that of PE. This is unexpected for several reasons. First, sPS chains are more rigid than PE chains. Second, the intercalation of

solvent molecules between stems as they are deposited is a factor which might be expected to make such a perfect arrangement less attainable. Finally, sPS crystallizes rapidly, which might be thought to prevent such good organization being reached.

A feature which now appears to be common to different macromolecules is that they try to perform folding to achieve the closest stem separation : for PE folding occurs in the [110] direction (figure 1.1), for iPS it alternates along the [010] and [100] directions (figure 1.6) and for sPS it occurs along the [010] direction (figure 5.9). For the two latter cases, the mode of folding implies that the macromolecule changes its helicity along its path. However, work with other crystallization temperatures and concentrations is required to throw further light on the mechanisms involved.

One of the parameters which is known to determine how molecules are incorporated on a growth surface is the roughness of the latter. There is a temperature T_R above which the growth face becomes rough. Smooth surfaces will favour adjacent stem attachment. On the other hand, it will be easier for any passing molecule other than one already attached to be caught on a rough surface, making adjacent reentry less possible.

The details of the chain conformation have consequences on the type of mechanisms occuring during crystallization. This is usually described as a two step mechanism involving, in a first stage, nucleation and followed by growth from the nucleus. There are broadly three regimes predicted to describe nucleation. In regime I, a first stem attaches on the growth face and subsequent stems are attached at adjacent positions, because this requires less surface energy. Regime I is also called the mononucleation regime. In regime II, several stems are deposited on the growth surface. From each of these nuclei growth

occurs until two growth fronts meet. Regime II is also called the polynucleation regime. Finally regime III is an extreme case where a high density of nucleation occurs. The predicted growth rates for the three regimes are proportional to $e^{-K/T\Delta T}$ where ΔT is the supercooling and K is some constant. A high degree of adjacency, together with superfolding, suggests regime II. For a detailed review on the crystallization theories, see for example ref. [91].

6.1.3 The chain conformation in the γ-phase

We decribed the chain conformation in the γ-phase by starting with that of the δ-phase, and disrupting the initial sheet-like structure. This model explains the difference in the radius of gyration between the two phases, and also the appearance of a peak at $q=0.55$Å in the Kratky plots of the γ-phase. This peak is therefore related to the existence of a correlation between pairs of stems distributed in a direction perpendicular to that of the initial sheet. No model of the crystal structure of the γ-phase has been published, so it is not possible to check the consistency of this model with the distribution of helicity of the stems in the γ-phase.

6.1.4. The transition from the δ- to the γ-phases

The variation of the chain dimension after the transition indicates significant movement of stems. It appears from infrared measurements that, during the transition, the amount of

material presenting a helical configuration passes through a minimum. After this minimum, the initial helical content is only partially recovered. We suggest that this minimum coincides with the temperature at which the mobility of the stems becomes sufficient for lamellar thickening to occur. In other words, the movement of stems is facilitated by the disruption of the helical configuration which itself is the result of the expulsion of the solvent molecules from the crystalline lattice.

As the temperature is increased, decomplexation starts and the initial helical configuration of the chains stabilized by solvent molecules becomes disordered. This leads to an increase of the mobility of the stems perpendicular to the plane of the lamella (figure 6.1).

6.2. Further work

Futher work can be oriented towards the use of other techniques and also the study of different samples. The present work concerns the particular case of the sPS/ethylbenzene complex crystallized at 40°C. A question remains if the lamellar morphology is typical of polymer/solvent complexes. The crystallization temperature seems to be an important factor affecting the type of morphology obtained by crystallization. For example, when crystallization occurs at 50°C, a fibrous morphology (reported as a ribbon like morphology by Hsu [16]) is obtained. Little is known about this morphology and the related chain conformation. Other solvents are known to form a complex with sPS, they could result in other types of morphologies.
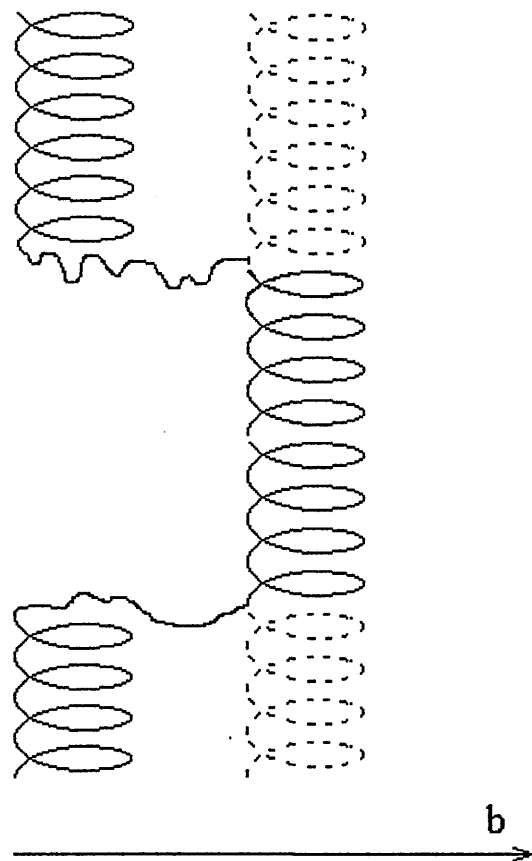
Figure 6.1

Proposed intermediate structure formed during the δ to γ phase transition.
Disordered chain segments allow the movement of part of the original helix.
The final stem structure, with disorder replaced by helical segments, is
shown by the dashed line.

By further annealing of the γ-phase, two other phases can be reached, which are the α- and

β-phases. Now that we have clarified how the conformation in the γ-phase is related to that

of the δ-phase, it could be interesting to push these investigation further and to determine

the mechanisms involved at the transition between the γ-phase and the α- or β-phases. We

know already from the WAXS patterns, that disordering occurs, which may involve partial melting. Note that these mechanisms will not involve solvent molecules.

In the infrared work, we proceeded by heating a sample so as to go from the less stable phase (δ) to the phase of maximum stability (α). It is also possible to follow another procedure in the evolution of a sample. A sample in the α-phase can be obtained by crystallization from the melt, and it has been shown that swelling of this sample can bring it to the δ-phase. The morphology obtained is probably different and a spherulitic structure is expected. The chain conformation and the mechanisms involved at the transition from the α- to the δ-phase are of interest. We can imagine here that this could involve identical mechanisms to those decribed in the transition from the δ- to the γ- phases, with for example a disordering of the initial zigzag configuration, followed by stabilization of the helix as the incorporation of solvent molecules occurs.

The knowledge of the existence of solvated and non-solvated helical bands in the infrared spectrum opens the path to many new investigations. An infrared study of an empty δ-phase sample slowly reswelled could show interesting features. There could be an inversion of the process observed for the δ to γ transition, leading to a loss in the helical content at the transition followed by an increase, with the bands at 940 and 943 cm^{-1} showing an opposite behaviour to that observed when a δ-phase is annealed. Here, the lack of information concerning the crystalline structure of the γ-phase could present a problem in the interpretation of these data.

Also these bands provide a way to study the mechanisms involved during the crystallization. As crystallization leads, in a first stage, to the stabilization of the helix and

then to the formation of a polymer/solvent complex, the bands at 934-940 cm^{-1}, could give significant information on these two mechanisms. By using an infrared liquid cell, a time dependent experiment could be realised. In this way, the crystallization could be monitored during its process.

Other investigations could be carried out which would involve other techniques than those we already used. For example, NMR and Raman spectroscopy could bring useful information, with the advantage of having both protonated and deuterated materials. The former would allow the study of the mobility of the solvent molecules. The latter could, in the low frequency range (0-200 cm^{-1}), give us information about polymer sidechain mobility within the lattice.

Finally, considering the success of the statistical model, it would be interesting to carry out similar simulations using the known values for the crystal dimensions of iPS in order to get the statistical parameters, and in particular the probability of adjacency as a function of crystallization temperature and molecular weight. Previous work by Guenet et al. has already demonstrated the existence of dilution [7], but no quantitative study was made. Neutron scattering data are already available, and could be used for comparison with model calculations.

References

1. Sadler, D. M., Comprehensive Polymer Science, 1989, Vol. 1, Chap. 32, Pergamon Press

2. Keller, A., Phil. Mag., 1957, **2**, 1171

3. Sadler, D. M. and Keller, A., Polymer, 1976, **17**, 37

4. Sadler, D. M. and Keller, A., Macromolecules, 1977, **10**, 1128

5. Spells, S. J. and Sadler, D. M., Polymer, 1984, **25**, 739

6. Sadler, D. M. and Keller, A., Science, 1979, **203**, 263

7. Guenet, J.-M., Sadler, D. M. and Spells, S. J., Polymer, 1990, **31**, 195

8. Sadler, D. M., Spells, S. J., Keller, A. and Guenet, J.-M., Polym. Commun., 1984, **25**, 290

9. Ishihara, N., Seimiya, T., Kuramoto, M. and Uoi, M., Macromolecules, 1986, **19**, 2464

10. Chatani, Y., Shimane, Y., Inagaki, T., Ijitsu, T., Yukinari, T. and Shikuma, H., Polymer, 1993, **33**, 488

11. Chatani, Y., Shimane, Y., Inagaki, T., Ijitsu, T., Yukinari, T. and Shikuma, H., Polymer, 1993, **34**, 1620

12. Greis, O., Xu, Y., Asano, T. and Petermann, J., Polymer, 1989, **30**, 590

13. De Candia, F., Filho, A. R. and Vittoria, V., Makromol. Chem., Rapid Commun., 1991, **12**, 295

14. Manfredi, C., De Rosa, C., Guerra, G., Rapacciuolo, M., Auriemma, F. and Corradini., P., Macromol. Chem. Phys., 1995, **196**, 2795

15. Guerra, G., Manfredi, C., Rapacciuolo, M., Corradini, P., Mensitieri, G. and Del Nobile, M., A., Italian Patent, 1994 (CNR)

16. Wang, Y.K., Savage, J.D., Yang, D. and Hsu, S.L., Macromolecules, 1992, **25**, 3659

17. Sonntag, P., Care, C. M., Spells, S. J. and Halliday, I., J. Chem. Soc. Faraday Trans., 1995, **91**, 2593

18. Sadler, D. M., J. Appl. Cryst., 1983, **16**, 519

19. Guenet, J.-M., Thermoreversible Gelation of Polymers and Biopolymers, Academic Press, 1992

20. Corradini, P. and Guerra, G., Advances in Polymer Science, 1992, **100**, 183

21. Kusuyama, H., Takase, M., Higashihata, Y., Tseng, H. T., Chatani, Y. and Tadokoro, H., Polymer, 1982, **23**, 1256

22. Assender, H. E. and Windle, A. H., Macromol. Symp., 1997, **114**, 199

23. Dosière, M., Macromol. Symp., 1997, **114**, 51

24. Dell'Isola, Floridi, G., Rizzo, P., Ruiz de Ballesteros, O. and Petraccone, V., Macromol. Symp., 1997, **114**, 243

25. Keller, A. and O'Connor, A., Discussions Faraday Soc., 1958, **25**, 114

26. Bank, M. I.and Krimm, S., J. Polym. Sci (A-2) 1969, **7**, 1785

27. Painter, P. C., Havens, J., Hart, W. W. and Koenig, J. L., Journal of Polymer Science: Polymer Physics Edition, 1977, **15**, 1223

28. Patel, G. N. and Keller, A., J. Polym. Sci. Phys. Ed., 1975, **13**, 2259

29. Sadler, D. M., Faraday Discuss. Chem. Soc., 1980, **69**, 91

30. Schelten, J., Wignall, G. D. and Ballard, D. G. H., Polymer, 1974, **15**, 682

31. Schelten, J., Ballard, D. G. H., Wignall, G. D., Longman, G. and Schmatz, W., polymer, 1976, **17**, 751

32. Spells, S. J., Sadler, D. M. and Keller, A., Polymer, 1980, **21**, 1121

33. Spells, S. J., Polymer Comm., 1984, **25**, 162

34. Sadler, D. M., Faraday Discussions, 1979, **68**, 429

35. Sadler, D. M., and Spells, S. J., Macromolecules, 1989, **22**, 3941

36. Spells, S. J. and Hill, M. J., Polymer, 1991, **32**, 2716

37. Sadler, D. M., Polymer Comm., 1985, **26**, 204

38. Natta, G., Corradini, P. and Bassi, I. W., Nuovo Cimento, 1960, **1**, 68

39. Guenet, J.-M., Picot, C. and Benoit, H, Macromolecules, 1979, **12**, 86

40. Guenet, J.-M., Macromolecules, 1980, **13**, 387

41. Kobayashi, M., Nakaoki, T. and Uoi, M., Rep. Progr. Polym. Phys. Jpn., 1988, **31**, 481

42. Immirzi, A., de Candia, F., Iannelli, P., Vittoria, V. and Zambelli, A., Makromol. Chem. Rapid. Commu., 1988, **9**, 761

43. Corradini, P., Napolitano, R. and Pirozzi, B. , Eur. Polym. J., 1990, **26**, 157

44. Guerra, G., Vitagliano, V. M., De Rosa, C., Petraccone, V. and Corradini, P., Macromolecules, 1990, **23**, 1539

45. Kellar, E. J. C., Evans, A. M., Knowles, J., Galiotis, C. and Andrews, E. H., Macromolecules, 1997, **30**, 2400

46. Gianotti, G. and Valvassori A., Polymer, 1990, **31**, 473

47. Reynolds, N. M., Stidham, H. D. and Hsu, S. L., Macromolecules, 1991, **24**, 3662

48. De Rosa, C., Guerra, G., Petraccone, V. and Pirozzi, B., Macromolecules, 1997, **30**, 4147

49. Manfredi, C., Del Nobile, M. A., Mensitieri, G., Guerra, G. and Rapacciuolo, M., J. of Polym. Sci. : Part B : Polym. Phys., 1997, **35**, 133

50. Kobayashi, M., Nakaoki, T., Ishinara, N., Macromolecules, 1989, **22**, 4377

51. Chatani, Y., Inagaki , T., Shimane, Y. and Shikuma, H., Polymer, 1993, **34**, 4841

52. Gomez, M. A., Tonelli, A. E., Macromolecules, 1991, **24**, 3533

53. De Candia, F., Guadagno, L. and Vittoria, V., J. Macromol. Sci.-Phys., 1995, **B34**, 95

54. Chatani, Y., Shimane, Y., Inagaki, T., Ijitsu, T., Yukinari, T. and Shikuma, H., Polymer, 1993, **34**, 1625

55. Roels, T., Deberdt, F. and Berghmans, H., Macromolecules, 1994, **27**, 6216

56. Deberdt, F. and Berghmans, H., Polymer, 1993, **34**, 2192

57. Daniel, Ch., Deluca, M. D., Brûlet, A., Menelle, A. and Guenet, J.-M., Polymer, 1996, **37**, 1273

58. Daniel, Ch., Menelle, A., Brûlet, A. and Guenet, J.-M., Polymer, 1997, **16**, 4193

59. De Candia, F., Guadagno, L. and Vittoria, V., J. Macromol. Sci.-Phys., 1994, **B33**, 347

60. Auriemma, F., Petraccone, V., Dal Poggetto, F., De Rosa, C., Guerra, G., Manfredi, C. and Corradini, P., Macromolecules, 1993, **26**, 3772

61. Petraccone, V., Auriemma, F., Dal Poggetto, F., De Rosa, C., Guerra, G. and Corradini, P., Makromol. Chem., 1993, **194**, 1335

62. Vittoria, V., Filho, A. R. and de Candia, F., J. Macromol. Sci. Phys., 1990, **B29**, 411

63. Vittoria, V., Filho, A. R. and de Candia, F., J. Macromol. Sci. Phys., 1991, **B30**, 155

64. Nakaoki, T. and Kobayashi, M., Journal of Molecular structure, 1991, **242**, 315

65. Capitani, D., De Rosa, C., Ferrando, A., Grassi, A. abd Segre, A. L., Macromolecules, 1992, **25**, 3874

66. Stölken, S., Ewen, B., Kobayashi, M. and Nakaoki, T., J. of Polymer Science : Part B : Polymer Physics, 1994, **32**, 881

67. Rastogi, S. and Gupta, V. D., J. Macromol. Sci.-Phys., 1994, **B33**, 129

68. Rastogi, S. and Gupta, V. D., J. Macromol. Sci-Phys., 1995, **B34**, 1

69. Nyquist, R. A., Putzig, C. L., Leugers, M. A., McLachlan R. D. and Thill, B., Applied Spectroscopy, 1992, **46**, 981

70. Reynolds, N. M., Savage, J. D. and Hsu, S. L., Macromolecules, 1989, **22**, 2867

71. Vittoria, V., Polymer Communications, 1990, **31**, 263

72. Jasse, B. and Monnerie, L., J. Mol. Struct., 1977, **39**, 165

73. Baltà-Calleja, F. J., Vonk, C. G., X-Ray Scattering of Synthetic Polymers, 1989, Elsevier

74. Glatter, O. and Kratky, O., Small Angle X-ray Scattering, 1982, Academic Press

75. Atkins, E. D. T., Comprehensive Polymer Science, 1989, Vol. 1, Chap. 28, Pergamon Press

76. Wunderlich, B., Thermal Analysis, Academic Press, 1990

77. Bower, D. I. and Maddams, W. F., The Vibrational Spectroscopy of Polymers, Cambridge University Press, 1989

78. Kobayashi, M., Akita, K. and Tadokoro, H., Makromol. Chem., 1968, **11**, 324

79. Cooley, J. W. and Tukey, J., Math. Comp., 1965, **19**, 297

80. Krimm, S., Advances in Polymer Science, 1960, 2, 51

81. Spells, S. J., Characterization of Solid Polymers : New techniques and developments, Chapman and Hall, 1994

82. Higgins, J. S. and Benoît, H. C., Polymers and Neutron Scattering, Oxford U.P., 1994

83. Higgins, J. S. and Maconnachie, A., Methods of Experimental Physics, Volume 23, Part C, Chapter 22, Academic Press, 1987

84. Young, R. J. and Lovell, P. A., Introduction to Polymers, Chapman et Hall, 1991

85. Daniel, Ch., Thèse Doctorale Européenne, Université Louis Pasteur, Strasbourg, 1996

86. Sonntag., P., Daniel, Ch. and Spells, S. J., unpublished

87. Ruvolo Filho, A and Vittoria, V., Makromol. Chem., Rapid Commun., 1990, **11**, 199

88. Magill, J. H., Girolamo, M. and Keller, A., Polymer, 1981, **22**, 43

89. Guenet, J.-M. and Picot, C., Polymer, 1979, **20**, 1473

90. Berghmans, H., private comm.

91. Armitstead, K. and Goldbeck-Wood, G., Advances in Polymer Science, 1992, **100**, 219

92. Sadler, D. M., Polymer, 1983, **24**, 1401

93. Oster, G. and Riley, D. P., Acta Cryst., 1952, **5**, 272